

UNCLASSIFIED

AD NUMBER

AD875027

LIMITATION CHANGES

TO:

Approved for public release; distribution is unlimited. Document partially illegible.

FROM:

Distribution authorized to U.S. Gov't. agencies and their contractors; Critical Technology; SEP 1970. Other requests shall be referred to Air Force Technical Applications Center, VSC, Alexandria, VA 22313. This document contains export-controlled technical data.

AUTHORITY

usaf ltr, 25 jan 1972

THIS PAGE IS UNCLASSIFIED

TR 70-29

AD 875027

20  
CB

TECHNICAL REPORT NO. 70-29

DEVELOPMENT OF LP WAVE DISCRIMINATION CAPABILITY  
USING LP STRAIN INSTRUMENTS  
QUARTERLY REPORT NO. 8  
PROJECT VT/8706

SPONSORED BY

ADVANCED RESEARCH PROJECTS AGENCY  
NUCLEAR TEST DETECTION OFFICE  
ARPA ORDER NO. 624

AVAILABILITY

QUALIFIED USERS MAY REQUEST COPIES  
OF THIS DOCUMENT FROM:

DEFENSE DOCUMENTATION CENTER  
CAMERON STATION  
ALEXANDRIA, VIRGINIA 22314

ACKNOWLEDGEMENT

THIS RESEARCH WAS SUPPORTED BY THE ADVANCED RESEARCH  
PROJECTS AGENCY, NUCLEAR TEST DETECTION OFFICE, UNDER  
PROJECT VELA-UNIFORM, AND ACCOMPLISHED UNDER THE  
TECHNICAL DIRECTION OF THE AIR FORCE TECHNICAL APPLICATIONS  
CENTER UNDER CONTRACT NO. F33615-69-C-0121

NOTICE

THIS DOCUMENT IS SUBJECT TO SPECIAL EXPORT CONTROLS AND EACH  
TRANSMITTAL TO FOREIGN GOVERNMENTS OR FOREIGN NATIONALS  
MAY BE MADE ONLY WITH PRIOR APPROVAL OF CHIEF, AFTAC.

DDC  
RECEIVED  
OCT 5 1970  
C

TELEDYNE  
GEOTECH

# DISCLAIMER NOTICE

THIS DOCUMENT IS THE BEST  
QUALITY AVAILABLE.

COPY FURNISHED CONTAINED  
A SIGNIFICANT NUMBER OF  
PAGES WHICH DO NOT  
REPRODUCE LEGIBLY.

TECHNICAL REPORT NO. 70-29

DEVELOPMENT OF LP WAVE DISCRIMINATION  
CAPABILITY USING LP STRAIN INSTRUMENTS  
Quarterly Report No. 8, Project VT/8706

by

James E. Fix

and

John R. Sherwin

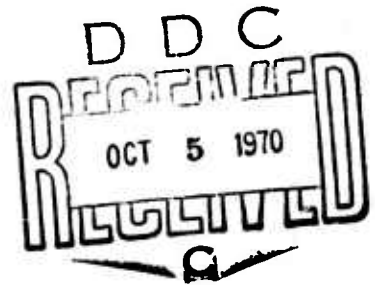
Sponsored by

Advanced Research Projects Agency  
Nuclear Test Detection Office  
ARPA Order No. 624

Availability

Qualified users may request copies of  
this document from:

Defense Documentation Center  
Cameron Station  
Alexandria, Virginia 22314



Acknowledgement

This research was supported by the Advanced Research Projects Agency, Nuclear Test Detection Office, under Project VELA-UNIFORM, and accomplished under the technical direction of the Air Force Technical Applications Center under Contract No. F33657-69-C-0121

**NOTICE**

THIS DOCUMENT IS SUBJECT TO SPECIAL  
EXPORT CONTROLS AND EACH TRANS-  
MITTAL TO FOREIGN GOVERNMENTS  
OR FOREIGN NATIONALS MAY BE MADE  
ONLY WITH PRIOR APPROVAL OF CHIEF,  
AFTAC. *VSC, Alex Va 22313.*

TELEDYNE GEOTECH  
3401 Shiloh Road  
Garland, Texas

21 September 1970

IDENTIFICATION

AFTAC Project No.	VELA T/8706
Project Title	Development of LP Wave Discrimination Capability Using LP Strain Instruments
ARPA Order No.	624
ARPA Program Code No.	8F10
Name of Contractor	Teledyne Industries, Inc.
Contract No.	Geotech Division
Effective Date of Contract	F33657-69-C-0121
Amount of Contract	1 July 1968
Contract Expiration Date	\$555,990
Project Manager	31 December 1970
	James E. Fix
	271-2561, A/C 214

## CONTENTS

	<u>Page</u>
ABSTRACT	
1. INTRODUCTION	1
2. DEVELOP DESIGN SPECIFICATIONS, TASK a(1)	1
3. DETERMINE THE MOST EFFECTIVE TECHNIQUE, TASK a(2)	1
4. DESIGN, FABRICATE, AND TEST LABORATORY MODELS, TASK b(1)	1
5. DEVELOP A FINAL ENGINEERING MODEL DESIGN, TASK b(2)	1
5.1 Optical Displacement Transducer, Model 32770	2
5.2 Variable-capacitance displacement transducer	2
6. DESIGN A FIELD TEST INSTALLATION, TASK b(3)	3
7. DESIGN, FABRICATE, AND INSTALL THE FIELD TEST INSTALLATION, TASK c(1)	5
7.1 Fabricate instrumentation	5
7.2 Installation of the strain/inertial complex	5
7.2.1 Additional equipment installed	5
7.2.2 Future plans	5
8. CONDUCT NOISE AND STABILITY TESTS, TASK c(2)	6
9. CONDUCT PRELIMINARY OPERATION AND EVALUATE INSTRUMENT PERFORMANCE, TASK c(3)	6
10. OPERATE THE STRAIN-INERTIAL SYSTEM, TASK d(1)	6
10.1 Equipment modifications	6
10.1.1 Long-period inertial seismometers	6
10.1.2 Strain seismometers	7
10.2 Maintenance	8
10.3 Amplitude and phase response	8
10.4 Future plans	14
11. DEVELOP METHODS OF WAVE DISCRIMINATION, TASK d(2)	14
11.1 Enhancement of signals from interfering events	15
11.2 Enhancement of short-period waves	20
11.3 Enhancement of surface waves and detection of low level signals	26
11.4 Comparisons between the parallel strain seismographs	37
11.4.1 Spectral analysis presentation	37
11.4.2 Low wind conditions	39
11.4.3 High wind conditions	46
11.4.4 Earthquake signals	57

CONTENTS (continued)

	<u>Page</u>
11.5 Seismic noise resulting from atmospheric pressure variations	67
11.5.1 Previous observations of wind-related long-period noise	67
11.5.2 Long-period earth strains and atmospheric pressure variation	70
11.5.3 Observed strains and pressure variations	73
11.6 Linear and non-linear tilt noise on long-period seismographs	76
11.6.1 Tilt theory for ALPS response horizontal seismographs	76
11.6.2 Seismic spectral changes with pressure activity changes	77
11.6.3 Non-linear tilting	81
12. SPECIAL REPORT	82
13. REFERENCES	82
APPENDIX - Instrument Nomenclature, Recorder Channel Allocation, and Polarity	

## ILLUSTRATIONS

<u>Figure</u>		<u>Page</u>
1	Schematic of the detector for the variable capacitance transducer	4
2	Pulses resulting from a step of current into the calibration coil of P55L	10
3	Amplitude response of P55L calculated from the pulse in figure 2	11
4	P55L experimental amplitude response and amplitude response from smoothing and numerical differentiation of pulse from a step of acceleration	12
5	Phase response of P55L calculated from the pulse in figure 2	13
6	Great circle paths from two earthquakes to QC-AZ	16
7	Four beam azimuthal array at QC-AZ. Solid lines are response to Rayleigh and horizontal component of P and SV waves. Dashed lines are response to Love, G, and SH waves	17
8	Magnetic tape playback of arrivals from interfering events. Event 1: $t = 2003:42.2$ , south Sandwich Island region, $h = 70$ km, $m_b = 6.0$ , $\Delta = 113.5$ deg, azimuth = $142.5$ deg; event 2: $t = 2030:54.7$ , Andreanoff Island, $h = 48$ , $m_b = 5.7$ , $\Delta = 50.6$ deg, azimuth = $312.0$ deg	19
9	Enhancement of short-period arrivals from an explosion	21/22
10	Enhancement of short-period arrivals from an earthquake during the coda of an earlier event	23/24
11	Reproduction of 16 mm film recording of LQ1 Love wave and LR1 Rayleigh wave. USC&GS preliminary epicenter data: $t = 1131:34.3$ , $11.7$ N, $92.9$ W, near coast of Chiapas, Mexico, $h = 68$ , $m_b = 4.0$ , $\Delta = 25.1$ deg, azimuth = $132.8$ deg	27
12	Reproduction of 16 mm film recording of surface wave. USC&GS preliminary epicenter data: $t = 1058:03.5$ , $79.7$ N, $3.5$ E, Greenland Sea, $h = N$ , $m_b = 4.1$ , $\Delta = 61.9$ deg, azimuth = $10.6$ deg	29
13	Reproduction of a 16 mm film recording of a Rayleigh wave train from an earthquake near New Britain Island. $t = 1448:38$ , $5.1$ S, $152.1$ E, $h = 70$ , $m_b = 5.0$ , $\Delta = 98$ deg, azimuth = $270$ deg	30



# ILLUSTRATIONS (continued)

<u>Figure</u>		<u>Page</u>
14	Reproduction of a 16 mm film recording of a Rayleigh wave train from an earthquake near New Britain Island. 0 = 1448:38, 5.1S, 152.1E, h = 70, $m_b$ = 5.0, $\Delta$ = 98 deg, azimuth 270 deg	31
15	Reproduction of a 16 mm film recording of a Rayleigh wave train from an earthquake off the coast of Ecuador. 0 = 1408:54, 2.5N, 83.0W, h = ?, $m_b$ = 4.4, $\Delta$ = 42 deg, azimuth = 135 deg	32
16	Reproduction of a 16 mm film recording of a Rayleigh wave train from an earthquake off the coast of Ecuador. 0 = 1408:54, 2.5N, 83.0W, h = ?, $m_b$ = 4.4, $\Delta$ = 42 deg, azimuth = 135 deg	33
17	Reproduction of 16 mm film recording of LR1 Rayleigh wave. USC&GS preliminary epicenter data: 0 = 0517:14.0, 39.2N, 29.5E, Turkey, h = 27 km, $m_b$ = 4.2, $\Delta$ = 99.5 deg, azimuth = 29.6 deg	34
18	Reproduction of 16 mm film recording showing enhancement of LR1 Rayleigh wave on S325L-P325L and S55L-P55L difference traces. USC&GS preliminary epicenter data: 0 = 0517:14.0, 39.2N, 29.5E, Turkey, h = 27 km, $m_b$ = 4.2, $\Delta$ = 99.5 deg, azimuth = 29.6 deg	35
19	Reproduction of a 16 mm film recording of a Rayleigh wave train from an earthquake in the Tonga Island Region. 0 = 0621:16.3, 19.3S, 173.6W, h = 33, $m_b$ = 5.3, $\Delta$ = 78.9 deg, azimuth = 238 deg	36
20	Reproduction of 16 mm film recording of a portion of the low wind sample	40
21	Power spectral density, coherence, and relative phase angle with 256 lags for parallel horizontal strain seismographs S325L1 and S325L2 during low wind conditions	41
22	Power spectral density, coherence, and relative phase angle with 128 lags for parallel horizontal strain seismographs S325L1 and S325L2 during low wind conditions	43
23	Power spectral density coherence, and relative phase angle with 256 lags for parallel horizontal seismographs, S325L1 strain and P325L inertial, during low wind conditions	45
24	Power spectral density, coherence, and relative phase angle with 128 lags for parallel horizontal seismographs, S325L1 strain and P325L inertial, during low wind conditions	47

# ILLUSTRATIONS (continued)

<u>Figure</u>		<u>Page</u>
25	Power spectral density, coherence, and relative phase angle with 256 lags for perpendicular horizontal strain seismographs S325L1 and S55L during low wind conditions	48
26	Reproduction of 16 mm film recording of a portion of the high wind sample	49
27	Power spectral density, coherence, and relative phase angle of parallel horizontal strain seismographs S325L1 and S325L2 during high wind conditions, 1 to 256 sec range	50
28	Power spectral density, coherence, and relative phase angle of parallel horizontal strain seismographs S325L1 and S325L2 during high wind conditions, 20 to 2560 sec range	52
29	Power spectral density, coherence, and relative phase angle of parallel horizontal strain seismographs S325U1 and S325U2 during high wind conditions	53
30	Power spectral density, coherence, and relative phase angle of parallel horizontal seismographs, S325L1 strain and P325L inertial, during high wind conditions	54
31	Power spectral density, coherence, and relative phase angle of perpendicular horizontal strain seismographs S325L1 and S55L during high wind conditions	55
32	Power spectral density, coherence, and relative phase angle of perpendicular horizontal strain seismographs S325U1 and S55U during high wind conditions	56
33	Power spectral density, coherence, and relative phase angle of parallel strain seismographs S325LL1 and S325LL2 during the LR1 Rayleigh wave coda of the Peru earthquake	58
34	Reproduction of 16 mm film recording of part of the LQ3 Love wave, the LR2, and the LR3 Rayleigh wave from the Peru earthquake. USC&G epicenter data: $0 = 2023:27.3$ , $9.2S$ , $78.8W$ , $h = 43$ km, near coast of northern Peru, $m_b = 6.6$ , $M_s = 7.8$ , $\Delta = 52.5$ deg, azimuth = $137.5$ deg	59
35	Power spectral density, coherence, and relative phase angle of parallel horizontal strain seismographs S325LL1 and S325LL2 during the LQ3 Love wave and the LR2 and the LR3 Rayleigh waves of the Peru earthquake	60
36	Power spectral density, coherence, and relative phase angle of perpendicular horizontal strain seismographs S325LL1 and S55LL during the LQ3 Love wave and the LR2 and the LR3 Rayleigh waves of the Peru earthquake	62

# ILLUSTRATIONS (continued)

<u>Figure</u>		<u>Page</u>
37	Reproduction of 16 mm film recording of LR1 Rayleigh wave from an aftershock of the Peru earthquake. USC&GS epicenter data: $\phi = 0136:10.2$ , $9.3S$ , $79.0W$ , $h \approx 48$ , off coast northern Peru, $m_b = 6.0$ , $M_s = 5.5$ , $\Delta = 52.5$ deg, azimuth = $137.5$ deg	63
38	Power spectral density coherence, and relative phase angle with 256 lags for parallel horizontal strain seismographs S325L1 and S325L2 during the LR1 Rayleigh wave of an aftershock of the Peru earthquake	64
39	Power spectral density, coherence, and relative phase angle with 128 lags for parallel horizontal strain seismographs S325L1 and S325L2 during the LR1 Rayleigh wave of an aftershock of the Peru earthquake	65
40	Power spectral density, coherence, and relative phase angle with 128 lags for parallel horizontal seismographs, S325L1 strain and P325L inertial, during the LR1 Rayleigh wave of an aftershock of the Peru earthquake	66
41	Relationship between equivalent ground displacement and wind velocity at WMO	69
42	Power spectral density, coherence, and relative phase angle between horizontal strain seismograph S325U1 and micro-barograph ML2	74
43	Power spectral density, coherence, and relative phase angle between horizontal strain seismograph S55U and micro-barograph ML2	75
44	Horizontal inertial ALPS seismograph response to displacement, tilt, and Rayleigh waves	78
45	Comparison of power spectral density between low and high wind conditions	80

TABLES

<u>Table</u>		<u>Page</u>
1	Relative response of strain/inertial complex to two earthquakes	18
2	Instrumentation systems compared	38
3	Tilt response of horizontal inertial seismometers to Rayleigh waves	79

## ABSTRACT

Progress during the second quarter of 1970 is reported. Variable-capacitance transducers will be installed on the three strain seismometers in July for a broad-band output. A second microbarograph records pressure fluctuations outside the mine. A second Develocorder and an analog computer are recording directional beams on-line by combining strain and inertial seismographs. The second 325 deg azimuth strain seismometer will be used to construct a vertical seismometer in July. Magnets and coils on the LP inertial seismometers were returned to a standard configuration to match the strain response. A low-pass filter on the input to the strain preamplifier has limited amplifier saturation from large signals out of the passband. The mine seal has been improved to a 4 hour time constant. Three methods of obtaining system transfer functions from special test data were investigated. The most practical is to record the output from a step or impulse of current into the calibration coil and determine the transfer function by numerical smoothing and differentiating. Magnetic tape playback and on-line recordings provide enhancement of signals, wave type identification, and sharpened time breaks from interfering events and from low-level teleseismic earthquakes. Enhanced short-period recordings demonstrate that Pn, Pg, Sn, and Sg travel times from Rangely, Colorado, to QC-AZ are significantly longer than between NTS and QC-AZ. Examples of small surface waves detected are:  $m_b = 4.1$  at 62 deg,  $m_b = 4.0$  at 25 deg, and  $m_b = 4.2$  at 100 deg. Power spectral density, coherence, and phase angle comparisons between parallel strain seismometers during low and high wind conditions and earthquake signals demonstrate that the instruments are operating properly and that calibrations are accurate. The history of the evaluation of wind-related LP noise is reviewed. Theoretical equations are developed for strains and tilts in a half-space from a plane wave pressure fluctuation. At 50 sec, a horizontal inertial seismometer operating at 100K (at 25 sec) has magnifications for displacements of 45,000, for Rayleigh waves of 46,300 and for tilts of 27,900,000. A hypothesis is presented that at all hard rock seismograph stations non-linear rigid block tilting occurs as a result of pressure loading and Rayleigh waves. Evidence that supports this hypothesis is: (1) There is a slight relative amplitude shift with frequency and a 90 deg relative phase between the two parallel strain seismometers. (2) The horizontal pendulums respond to significantly more tilt than is associated with a Rayleigh wave.

DEVELOPMENT OF LP WAVE DISCRIMINATION  
CAPABILITY USING LP STRAIN INSTRUMENTS  
Quarterly Report No. 8, Project VT/8706

1. INTRODUCTION

This report discusses the progress during April, May, and June, 1970 in the installation and preliminary operation of long-period (LP) strain and inertial seismographs with equivalent magnification and response characteristics. The instruments are being used to develop techniques for discrimination of LP seismic waves. The major effort on each task of the Statement of Work is discussed in separate sections. This report is to apprise the Project Office of the current status of Project VELA T/8706. It is submitted in compliance with Sequence No. A004 of the Contract Data Requirements List, Contract F33657-69-C-0121.

2. DEVELOP DESIGN SPECIFICATIONS, TASK a(1)

This task has been completed.

3. DETERMINE THE MOST EFFECTIVE TECHNIQUE, TASK a(2)

This task has been completed.

4. DESIGN, FABRICATE, AND TEST LABORATORY MODELS, TASK b(1)

This task has been completed.

5. DEVELOP A FINAL ENGINEERING MODEL DESIGN, TASK b(2)

This task, which was previously reported complete, was reopened when it became evident that a drift problem in the Optical Displacement Transducer, Model 32770, would require extensive testing and possible redesign. Since a recently designed Variable Capacitance Displacement Transducer (VCT) had been successfully operated by another group, it was decided that design efforts could be most profitably directed toward an adaptation of the VCT for use at Queen Creek, Arizona, Seismological Station (QC-AZ).

## 5.1 OPTICAL DISPLACEMENT TRANSDUCER, MODEL 32770

Testing of the optical transducer was continued in the stable mine environment at QC-AZ. These tests were directed mainly toward a determination of (1) the effects of heat generated by the exciter lamp on other instruments in the mine, and (2) the source of a serious long-term drift in the transducer. In the first test, the unit was installed on the S325-1 strain seismometer. (The QC-AZ instrument nomenclature, recorder channel allocations, and polarity conventions are given in the appendix.) Operation for several days showed an increase in noise on the S325L1 seismograph only while the thermal environment readjusted to the approximate 10 watt dissipation of the transducer. Long-term thermal effects were not studied because of unfavorable results on the second test. The long-term drift which had been observed in the underground vault in Garland was not improved by operation of the transducer in the thermally stable mine environment. With all optical elements mounted on the test fixture, the drift continued in the same direction and exceeded the dynamic range of the instrument, usually within 24 hours. The problem was further aggravated because the necessary frequent adjustments disturbed the thermal equilibrium of the instrument and started the drift cycle all over again. Although the drift was obviously an effect of temperature change, field tests were unsuccessful in pinpointing the source. Therefore, the development of the optical transducer was abandoned.

## 5.2 VARIABLE-CAPACITANCE DISPLACEMENT TRANSDUCER

Development of a displacement transducer for use on a strainmeter was begun under the Long Range Seismic Measurements (LRSM) program, Project VT/8703, at about the same time that work was started on the optical transducer on Project VT/8706. The VCT, described by Shopland (1970), was successfully operated as part of a strainmeter in a special test under Project VT/8703 during February, March, and April of this year. When field tests on the optical transducer produced unfavorable results, it was decided to adapt the VCT for use at QC-AZ. Since the original transducer was designed for unattended operation in shallow trench installations which would be subject to large strain noise rates, it was possible to simplify the new design to take advantage of better operating conditions in the QC-AZ mine. In particular, the following design modifications were made:

1. Only one variable capacitance detector was used for the transducer;
2. Power supply circuits were modified to be compatible with the existing QC-AZ power subsystem;
3. Remotely operated coarse and fine adjusting assemblies were omitted;
4. A 10:1 parallelogram-lever type motion reducer driven by a 2  $\mu\text{m}$  per division micrometer was substituted for the 100:1 reducer driven by a 10  $\mu\text{m}$ /div micrometer.

The resulting design, although lacking some of the features of the original design, can be built quicker at a considerably lower cost.

Preliminary specifications of the transducer are as follows:

Sensitivity (detector)	40 mV per micron displacement
Noise level (detector)	50 $\mu$ V p-p in the period range of 1000 to 1 sec
Linear range of operation	$\pm 10$ $\mu$ m minimum for $\pm 1$ percent linearity
Dynamic range (detector)	70 dB, minimum
Long-term drift	150 $\mu$ V/ $^{\circ}$ C
Frequency response	Flat in strain from dc; 6 dB down @7.5 Hz
Cut off rate	12 dB/octave
Min. detectable strain	$3 \times 10^{-11}$ , dc to 5 Hz (40 m rod length)
Power: Voltage	+19 to +23 Vdc, -19 to -23 Vdc, center common
Power	2 watts, maximum

The transducer consists of a dual, differential capacitor connected to a detector circuit which is shown schematically in figure 1. The center capacitor plate is attached to the strain rod and is maintained at ground potential. It moves between two fixed active capacitor plates. With the center plate midway between the other plates, capacitance of both capacitors is nominally 100 pF. In the detector, Z1 and Z2 are integrated circuit operational amplifiers connected as a free-running multivibrator. At balance, the complementary outputs of Z1 and Z2 are symmetrical square waves which contain no dc component. If the center plate is displaced, the capacitance of one side of the dual capacitor goes down while the other capacitance goes up in proportion to the displacement. Proportional changes are produced in the time constant circuits used to control multivibrator symmetry. The multivibrator output is then a nonsymmetrical square wave at approximately the same frequency as that at balance. These nonsymmetrical outputs are then filtered and the resulting dc components are applied to the positive and negative inputs of amplifier Z3. The output of Z3 is a dc voltage proportional to displacement.

In early June, design of the necessary mechanical components for the VCT was completed. No further design work under this task is planned.

#### 6. DESIGN A FIELD TEST INSTALLATION, TASK b(3)

This task has been completed.



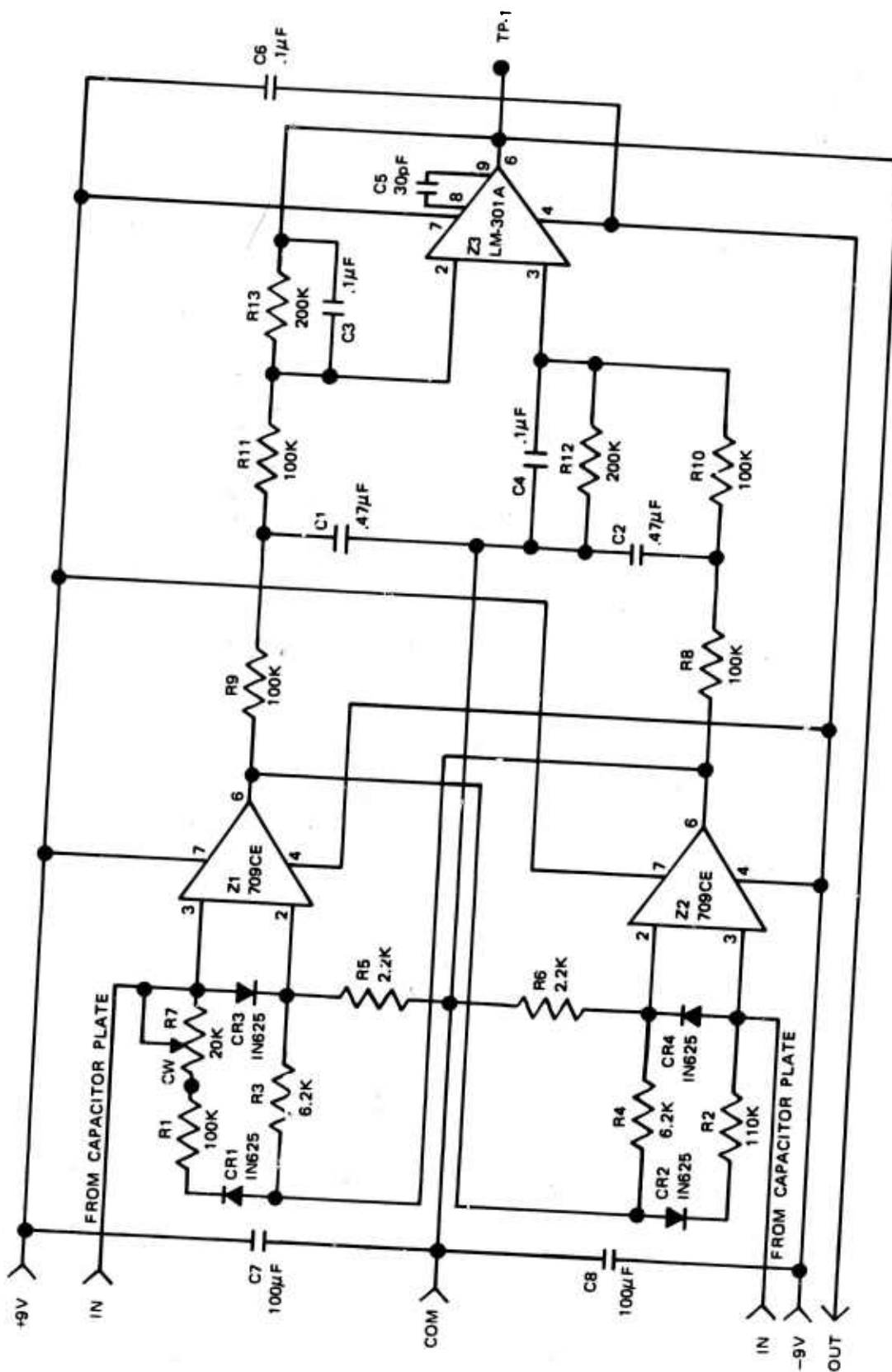


Figure 1. Schematic of the detector for the variable capacitance transducer

G 5698

## 7. DESIGN, FABRICATE, AND INSTALL THE FIELD TEST INSTALLATION, TASK c(1)

### 7.1 FABRICATE INSTRUMENTATION

When design work on the VCT was completed in early June, all necessary electronic components were ordered and fabrication of the mechanical parts was begun. The three transducers are scheduled for completion in early July, after which no further work under the sub-task is planned.

### 7.2 INSTALLATION OF THE STRAIN/INERTIAL COMPLEX

#### 7.2.1 Additional Equipment Installed

During this reporting period, several items of equipment were added to the QC-AZ system. The equipment was furnished to Project VT/8706 as Government Furnished Equipment (GFE).

The first major addition was a complete microbarograph system for monitoring outside air pressure changes. The system was installed on 8 April 1970 and has been recording on film and tape as ML2. The microbarograph transducer senses pressure changes with a single port and the overall response of ML2 is flat to rate-of-change of pressure from about 47 to 200 seconds. Calibration of the two microbarograph systems outside and inside the mine shows that the mine seal provides more than 40 dB attenuation of outside air pressure changes.

On 16 May 1970 routine operation of a second Develocorder, Model 4000, was begun. Prior to putting it in operation, the unit was dismantled for thorough cleaning, general maintenance, and updating with a light-slash time line marker. Recordings of various on-line sums and differences of the long-period strain and pendulum seismographs provide four beams steered toward azimuths of 325, 55, 145, and 235 degrees. Data are being used to demonstrate the on-line capability of the strain-inertial complex to enhance surface waves and to aid in wave discrimination and wave type identification. Signal isolation and gain control for the various sums is being provided by operational amplifiers in an Analog Computer, EAI, Inc., Model TR-10. The computer and the data control equipment for the second Develocorder required addition of a fifth equipment rack in the primary recording van.

#### 7.2.2 Future Plans

Data collected from the two side-by-side 325 deg azimuth strain seismometers are considered adequate for the purposes of the test. Therefore, the temporary S325 seismometer will be removed and its components installed for vertical operation in early July. Also, it is expected that the broad-band transducers can be completed and installed in late July. At that time, the installation phase at QC-AZ will be complete.

#### 8. CONDUCT NOISE AND STABILITY TESTS, TASK c(2)

Noise and stability tests are being conducted as part of the system operation. Results of the noise and stability tests are given under tasks d(1) and d(2).

#### 9. CONDUCT PRELIMINARY OPERATION AND EVALUATE INSTRUMENT PERFORMANCE, TASK c(3)

Preliminary operation has been completed and evaluation of instruments will be a continuing part of the system operation. Instrument evaluation is reported under tasks d(1) and d(2).

#### 10. OPERATE THE STRAIN-INERTIAL SYSTEM, TASK d(1)

Routine operation of the strain-inertial complex was continued on a 7-day-a-week basis. At the end of this reporting period, 21 separate seismograph channels and 5 environmental data channels were being routinely recorded on two 16-mm film recorders, one 35-mm film recorder, and three 14-channel FM tape recorders. Data were interrupted several times for equipment installation, modification, and maintenance.

##### 10.1 EQUIPMENT MODIFICATIONS

##### 10.1.1 Long-Period Inertial Seismometers

In early April, the amplitude responses of the long-period (LP) inertial seismographs indicated a serious variation from the theoretical curve. Since the strain seismographs were built to match the theoretical Advanced Long-Period Seismograph (ALPS) response, the different inertial response resulted in a degradation of on-line sums and differences between strain and inertial seismographs. The problem was traced to the seismometers which were equipped with more efficient transducers than the standard design. These prototype transducers were installed in another program prior to the transfer of the seismometers to Project VT/8706. The higher magnet charge and greater length of wire in the coils resulted in a seismometer with a much higher critical damping resistance (CDR) than normal. For example, the two horizontal seismometers had a CDR of about 2500  $\Omega$  as compared to the standard value of 1510  $\Omega$ . This high CDR resulted in overdamped seismometers when other system parameters were set to nominal values. In the ALPS system where the seismometer and galvanometer are direct coupled, seismometer and galvanometer damping plus the coupling coefficient are interrelated so that one parameter cannot be changed without affecting the other. It was therefore necessary to modify the transducers to obtain standard values of coil wire length, coil resistance, and magnet flux density.

New coils with less wire were wound and installed on the seismometers beginning on 21 May. These new coils incorporated a recent improvement in LP seismometer coils developed especially for high-gain operation. This improvement balances the diamagnetic and paramagnetic properties of the coil/coil-form assembly so that non-linearities in restoring force are minimized. In addition to the installation of new coils, magnet charge was adjusted on the seismometers. The vertical seismometers presented more of a problem than the horizontals. Since the vertical instrument requires a higher flux density than the horizontals (0.195T and 0.195T, respectively) and the prototype magnets could not be charged to a 0.195T flux density, standard magnets were used as replacements. The modifications to the vertical seismometer were completed on 18 June. A final (fine) matching between the strain and inertial seismographs will be made in the near future.

#### 10.1.2 Strain Seismographs

When using broad-band, solid-state amplifiers with velocity transducers, high frequency signals outside the normal passband can very easily saturate the amplifiers. In the strain system, this problem was anticipated and the flag output was incorporated in the strain filter unit to sense this excess voltage. After a spare 20-channel galvanometer bank became available to replace the galvanometer bank in Develocorder No. 1, recording of the flag trace as a 20th channel was begun on 27 April. It was immediately obvious that many of the large spikes recorded on LP strain channels were the result of Ithaco amplifier clipping associated with high amplitude short-period signals. To minimize this preamplifier clipping problem, capacitors were put across the transducer coil output leads on 11 May. The capacitors and coil resistances form single pole low-pass filters with a cut-off corner at 0.8 Hz. These filters reduce 10 Hz signals by about 20 dB, but do not affect periods long compared to 1.25 sec (0.8 Hz). The filters have been very effective in reducing the frequency of occurrence of saturation. It will be necessary to modify the short-period section of the Strain Filter, Model 33350 to achieve matched responses between short-period strain and inertial seismographs. The modification consists of changing the normal 0.8 Hz narrow band-pass filter to a 0.8 Hz high-pass filter. This filter, together with the low-pass coil-capacitor input filter, will form a composite, critically damped band-pass filter. It will be necessary to adjust the existing circuits to change the damping of the short-period inertial seismometers from 0.69 to 1.0 of critical to achieve matched short-period responses.

In another modification, the responses of the ultra-long-period (ULP) strain seismographs were changed to reduce the signal level at the recorders for periods longer than about 300 seconds. The original UPL2 response, which was flat to ground displacements from travelling waves at periods from 30 to 1000 seconds, allowed recording of high level, very long-period noise which limited the usefulness of the ULP recordings. The new response, designated ULP3, was achieved by substituting 283 sec low-pass filter cards for the 1000 sec filter cards, and is flat to ground displacements from travelling waves at periods from 30 to 283 seconds. The 283 sec low-pass filter is used in the ULP 1 response, so the cards for this change were on hand. In addition to the 283 sec filter change, the 30 sec low-pass filter cards were modified to provide an additional 14 dB of circuit gain. This was necessary to obtain sufficient background voltage for magnetic tape recordings.

## 10.2 MAINTENANCE

During April, considerable time was devoted to locating the cause of excessive noise on the LP inertial seismographs, especially P55L. The noise was found to be a combination of ground loops and 60 Hz voltage pickup in the unamplified data circuits. Ground loop problems at QC-AZ are increased by high ground resistivity which results in a 60 Hz potential difference of about 10 V p-p between the seismometer room and the adit of the mine. This problem was minimized by careful grounding techniques. The 60 Hz voltage pickup was found to occur in the twisted-pair, No. 12 AWG, solid copper data lines which extend some 460 feet from the seismometers to the phototube amplifiers (PTA's). Shielded data lines solved the problem.

Lightning damaged the Ithaco amplifiers in the strain system on 27 April and on 24 June. In both cases, shorted transistors in the amplifier output stages indicated that overvoltages were occurring on the field lines between the amplifier and the vans. The lightning protection circuits consist of gas-discharge diodes and high surge semiconductor diodes across the lines, and large inductors in series with the lines. These circuits are identical with circuits being successfully used on other programs but no reason has been found for their failure to adequately protect the QC-AZ circuits.

During this period, the mine seal was improved by eliminating leaks around the second and third ship's doors in the mine. Larger leaks, especially around the masonry holding the doors, were sealed with caulking compound. Smaller leaks were found in the many cracks in the rock around the doors. These were sealed by painting a relatively large area around both sides of the doors with a portland cement slurry. The time constant of the instrument room behind the third door is now about 4 hours and the time constant of the area between the second and third doors is about 40 minutes. This is considered more than adequate for successful operation.

## 10.3 AMPLITUDE AND PHASE RESPONSE

The determination of the amplitude and phase response of all the seismographs is essential to evaluate the precision of match between the strain and inertial seismographs. Considerable time is required to obtain amplitude and phase responses of long-period systems. Several cycles of each frequency with good signal-to-noise ratio are required. Amplitude responses are recorded on the film recorders and can be measured and plotted at a later time. Phase responses are obtained by adjusting phase of a calibration signal on a variable-phase function generator until the Lissajous figure on an oscilloscope indicates zero phase between the function generator reference output and the seismograph output. After numerous cycles are observed, phase adjusted, and reobserved, the phase difference is read from the dial and written down.

Three methods of obtaining the system transfer function by analytical processing of special test data have been considered: (1) random noise input; (2) numerical differentiation of the response to a step of current into the calibration coil; and (3) a least square fit between a theoretical pulse from a seismograph with known parameters and an actual pulse resulting from a step of current into the calibration coil. The second method was found to be the most practical because

it required less lost data than the first method and because it produced a more satisfactory solution than the third method.

To obtain the seismograph transfer function from a random noise input, a sufficiently long data sample must be obtained to provide the desired statistical stability of the cross power spectral density between the input and the output. A data sample at least 32 min duration would be necessary for periods up to 100 sec and at least 6.7 hr duration would be necessary for periods up to 2000 sec. An attempt was made to use the white noise from a resistor on the input of a broad-band dc amplifier driving the calibration coil of an inertial LP seismometer. With the broad-band system, 60 Hz noise dominated the calibration coil input. When it became evident that extreme grounding precautions would be necessary, the experiment was deferred to the other two methods and to other more pressing installation problems.

The three inertial P(Z, 325, 55)L seismographs were attenuated to improve the signal-to-noise ratio and several steps of current were applied to each of the three calibration coils separately. Figure 2 is a recording made from the magnetic tape. It shows the reduction in microseismic background by the attenuation and the first current-on and current-off and second current-on pulses on the P55L seismograph. These pulses were digitized and were used for evaluation of both methods two and three. Both methods use the fast Fourier transform algorithm of Cooley and Tukey to perform the required calculations rapidly.

The second method is straightforward, but contains the problems associated with numerical differentiation. The seismogram pulses are equivalent to the output of the seismograph for a step of acceleration input. (A step of current into the calibration coil produces a step of force  $F$  on the inertial mass  $M$  which is accelerated at the rate of  $F/M$ .) The desired amplitude and phase response is for an input of an impulse of displacement. To obtain the desired transfer function three derivatives are taken. Because of the excellent signal-to-noise ratio, the first attempt was to take the Fourier transform into the frequency domain and take a triple derivative by multiplying by  $(i\omega)^3$ . The first derivative (figure 3a) appeared smooth at all frequencies, and the desired third derivative (figure 3b) was relatively smooth at periods from 512 down to 20 sec. Below 20 sec the noise caused erratic results. A seven-point parabolic, least squares, smoothing (Lanczos, 1956) was then accomplished before each derivative was taken. The smoothed amplitude response is plotted down to 10 sec in figure 4 along with the experimentally measured amplitude curve. At 18 sec and 12 sec microseisms are seen to contribute noise to the result; however, when matched with the experimental curve, the results are very good when the microseismic energy is allowed for. The phase response curve is plotted in figure 5. A five-point, parabolic, least-square, smoothing was also tried, but the true data are sufficiently smooth that the seven-point smoothing produced better results for very little additional computation time.

The third method used to obtain the seismograph transfer function was considered unsuccessful. The method was developed by Mitchell and Landisman (1969) for the World Wide Standard Seismograph Network (WWSSN) recordings. A set of seismograph parameters are input to the program. A theoretical time domain response to an input step of acceleration is calculated using numerical integration which is inherently more stable than numerical differentiation.

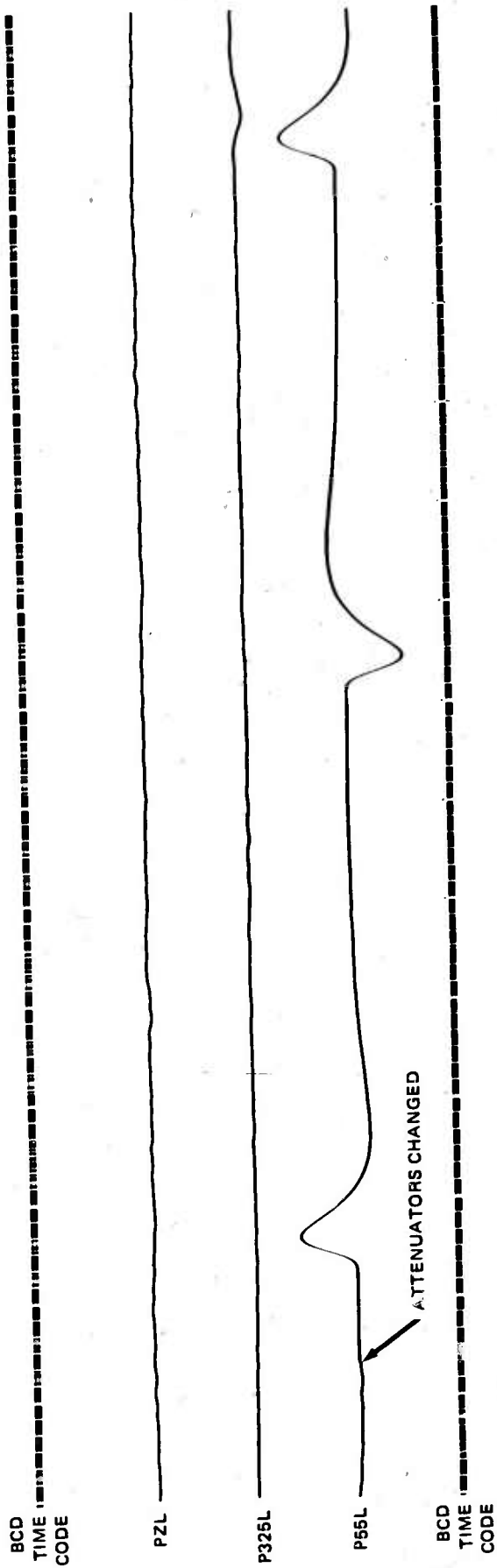
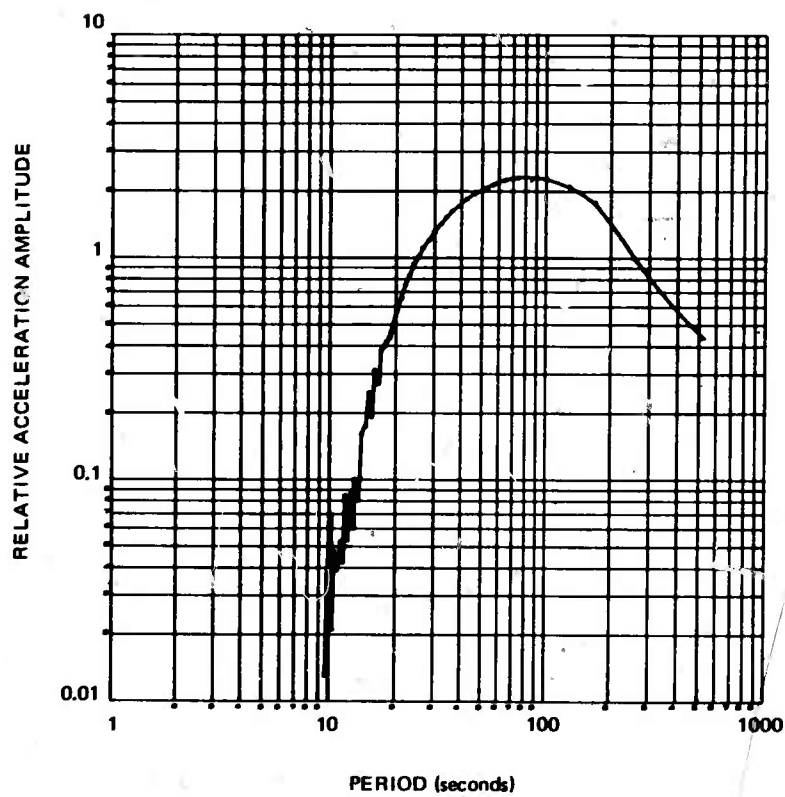


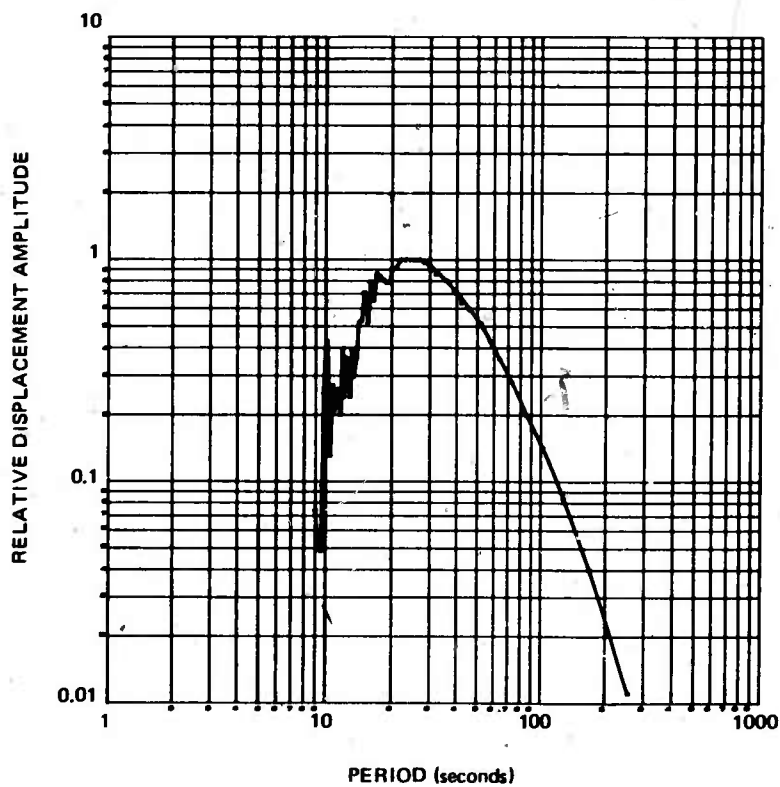
Figure 2. Pulses resulting from a step current into the calibration coil of P55L

OC-AZ  
PLAYOUT FROM  
TAPE RECORDER 1  
RUN 139  
19 MAY 1970

G 6005



a. P55L response to impulse of acceleration (one derivative, no smoothing)



b. P55L response to impulse of displacement (three derivatives, no smoothing)

Figure 3. Amplitude response of P55L calculated from the pulse in figure 2



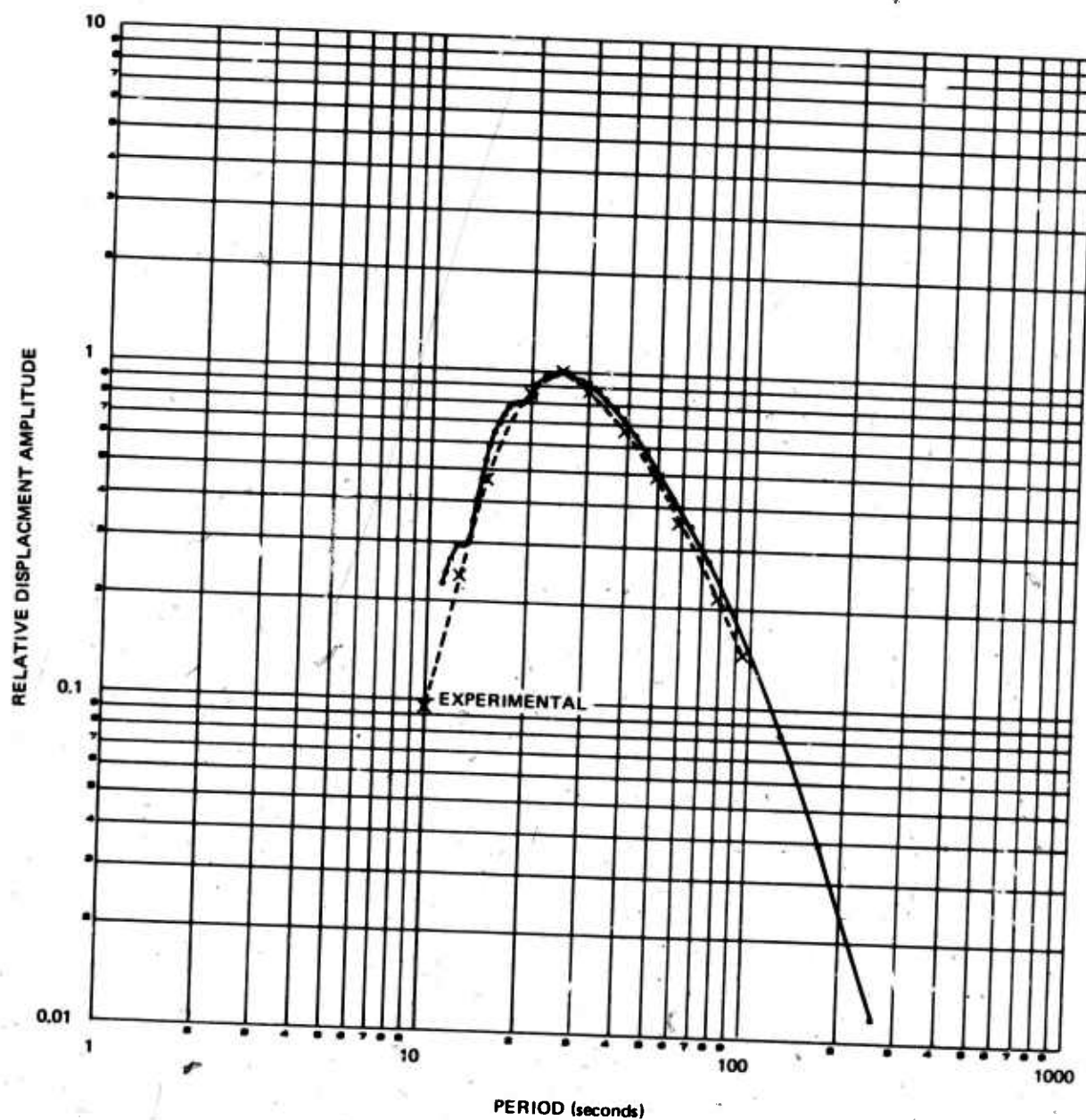


Figure 4. P55L experimental amplitude response and amplitude response from smoothing and numerical differentiation of pulse from a step of acceleration

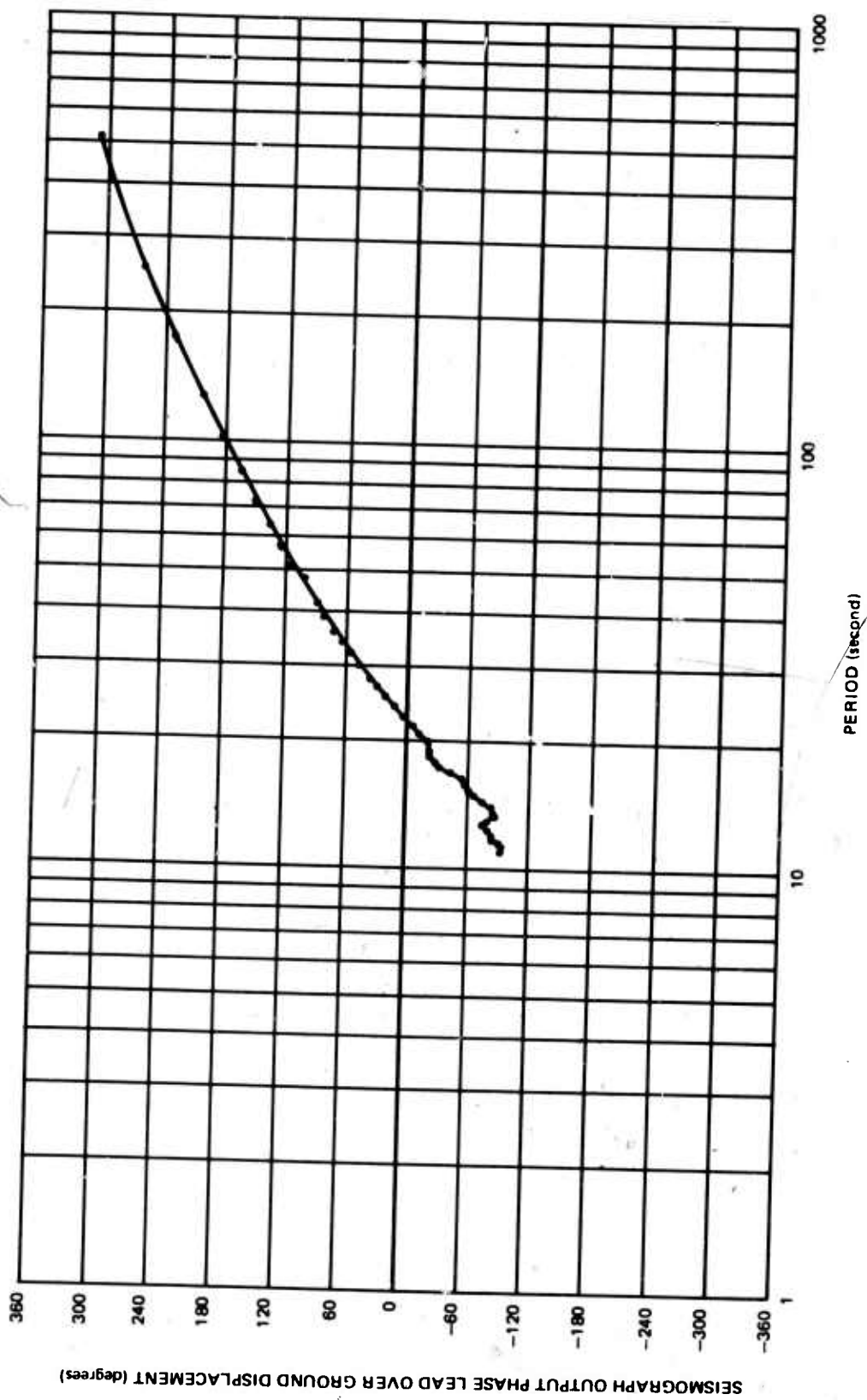


Figure 5. Phase response of P55L calculated from the pulse in figure 2

G 6008

A set of partial derivatives of the time domain pulse to changes in seismometer and galvanometer free period and damping is calculated. A least squares adjustment increment in these four parameters is calculated. The parameters are adjusted and the program iterates until the residual sum of squares between the theoretical and the actual time series is below a predetermined acceptable level. The WWSSN LP seismograph has a seismometer, an attenuation circuit, a galvanometer, and a photographic recorder with a light beam reflected off the mirror in the galvanometer. The QC-AZ seismographs contain electronic filters that do not have a counterpart in the WWSSN. It was necessary to add the transfer function of these filters to the program so that the proper theoretical response could be calculated. The filters are PTA plug-in filters, Model No. 6824-14, without a 6 sec notch, and Model No. 6824-15, with the notch. The parameters of the actual filters vary slightly from one to another, and the use of slightly incorrect corner frequencies may have affected the results some, but more serious problems were encountered. Since Mitchell and Landisman had such good success, the program was first used with real data. After completely unacceptable results were obtained, the measured system parameters were input to the program and the theoretical time domain pulse was output to use as an artificial signal for a test case. With this artificial signal, and parameters within 5 percent of the true parameters input to the program, it did not arrive at a correct solution after 25 iterations, although it was slowly incrementing in the right direction. Because the program did not converge rapidly, because it was very sensitive to the pulse start time and thus signal-to-noise ratio, and because of the longer computation time, this method was abandoned in favor of the second more straight-forward method.

#### 10.4 FUTURE PLANS

Out of necessity, operations have been continued throughout parts of the installation and testing phases. As a result, data quality has suffered somewhat, although collected data are adequate for the most part. In the next quarter, work on installation and testing tasks is expected to decrease. More emphasis can then be placed on the collection of consistent, well calibrated, high quality data.

#### 11. DEVELOP METHODS OF WAVE DISCRIMINATION, TASK d(2)

Methods of wave discrimination and methods of verifying proper instrument operation are being developed and pursued. In this report the preliminary results obtained with some of these methods are presented. An example of the enhancement of LP seismic waves from two interfering events is demonstrated. An illustration is presented of the enhancement of the arrivals from an explosion and of the arrivals from an earthquake in the coda of the Lg wave from the explosion. Examples of detection of surface waves from small events including an  $m_b = 4.2$  at an epicentral distance of 100 deg are illustrated. Results of an experiment to compare parallel horizontal strain seismometers are discussed. And, linear and non-linear tilt noises on the horizontal inertial seismographs are analyzed.

### 11.1 ENHANCEMENT OF SIGNALS FROM INTERFERING EVENTS

On 20 May 1970 two earthquakes occurred in opposite azimuths from QC-AZ. The arrival times of many of the elastic waves overlapped. The United States Coast and Geodetic Survey (USC&GS) Preliminary Determination of Epicenter (PDE) data on the two events are:

Event 1:  $O = 2003:42.2$ ,  $55.9S$ ,  $28.3W$ , South Sandwich Islands Region,

$h = 70$ ,  $m_b = 6.0$ ,  $\Delta = 113.5$  deg, azimuth station to epicenter =  $142.5$  deg.

Event 2:  $O = 2030:54.7$ ,  $51.5N$ ,  $178.5W$ , Andreanof Islands, Aleutian Is.,

$h = 48$ ,  $m_b = 5.7$ ,  $\Delta = 50.6$  deg, azimuth station to epicenter =  $312.0$  deg.

Epicentral distance and azimuth have been calculated from the PDE data, but are listed with the PDE information throughout the report. Figure 6 shows the great circle paths from the two epicenters to QC-AZ. Note that the path from event 2 is tangent to the Aleutian Island Arc at the beginning of its path. This passage through the anomalous island arc structure undoubtedly affected the amplitude and direction of travel of the seismic waves received at QC-AZ.

Before proceeding to the seismograms, the response of the combined strain and pendulum seismographs will be reviewed. When a strain and inertial seismograph are added, they enhance Rayleigh and Love waves in a certain azimuthal pattern. When they are differenced, they enhance waves in a complementary pattern. Figure 7 contains the azimuthal pattern of the four beams formed by the sum and difference between the two sets of strain and inertial seismographs oriented toward azimuths of  $325$  deg and  $55$  deg. The solid lines are the response to apparent horizontal waves such as Rayleigh and the horizontal component of P and SV. The dashed lines are the response to horizontal transverse shear waves such as Love, G, and SH. The beam patterns shown in figure 7 are independent of frequency and apply to long-period and short-period recordings alike. Table 1 is a list of the relative response of the QC-AZ beams to the two earthquakes.

At the time of these earthquakes, the second film recorder was just beginning operation and magnifications had not been equalized for the sum and difference traces. Figure 8 was prepared by playback of the magnetic tapes. The traces are identified on the left of the figure. The top and bottom traces are VELA binary coded decimal (BCD) time code indicating Greenwich Civil Time (GCT). Five minute time marks are identified above the traces. There is some overlap between lines in the figure. The first four seismic traces are related to the  $325$  deg azimuth with the sum of the strain and pendulum seismographs on top, then the strain, the pendulum, and the difference seismographs. The next four seismic traces are a similar arrangement for the  $55$  deg azimuth. The last three seismic traces are the vertical pendulum, the sum of the two orthogonal horizontal strain which is theoretically equal about  $-3$  times the vertical strain, and the difference between the orthogonal horizontal strain seismographs. According to theory, orthogonal horizontal strain seismographs will enhance Rayleigh waves and will not respond to Love waves. The difference between them will enhance Love waves, but it will also respond to Rayleigh waves.

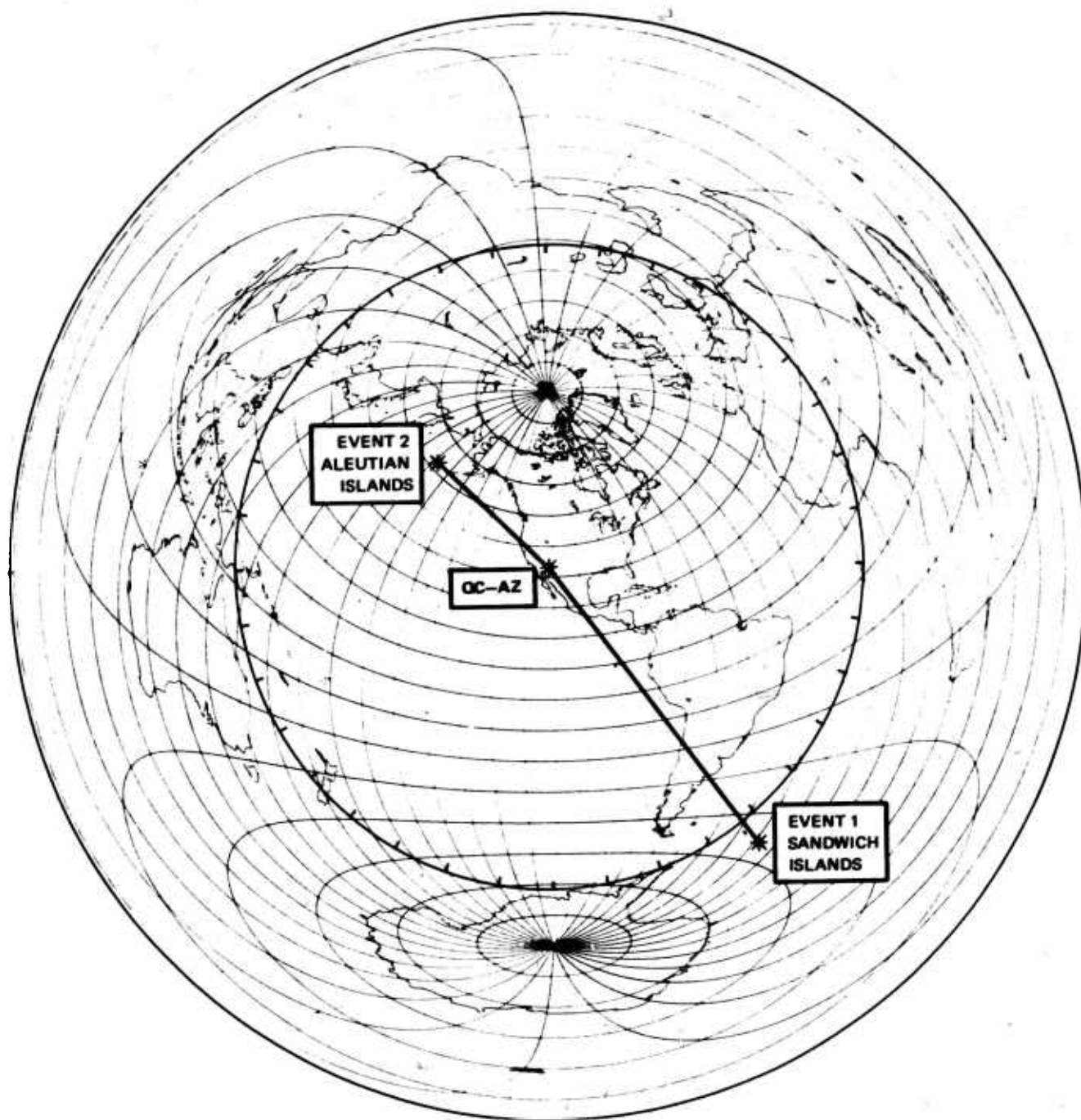


Figure 6. Great circle paths from two earthquakes to QC-AZ

G 6009

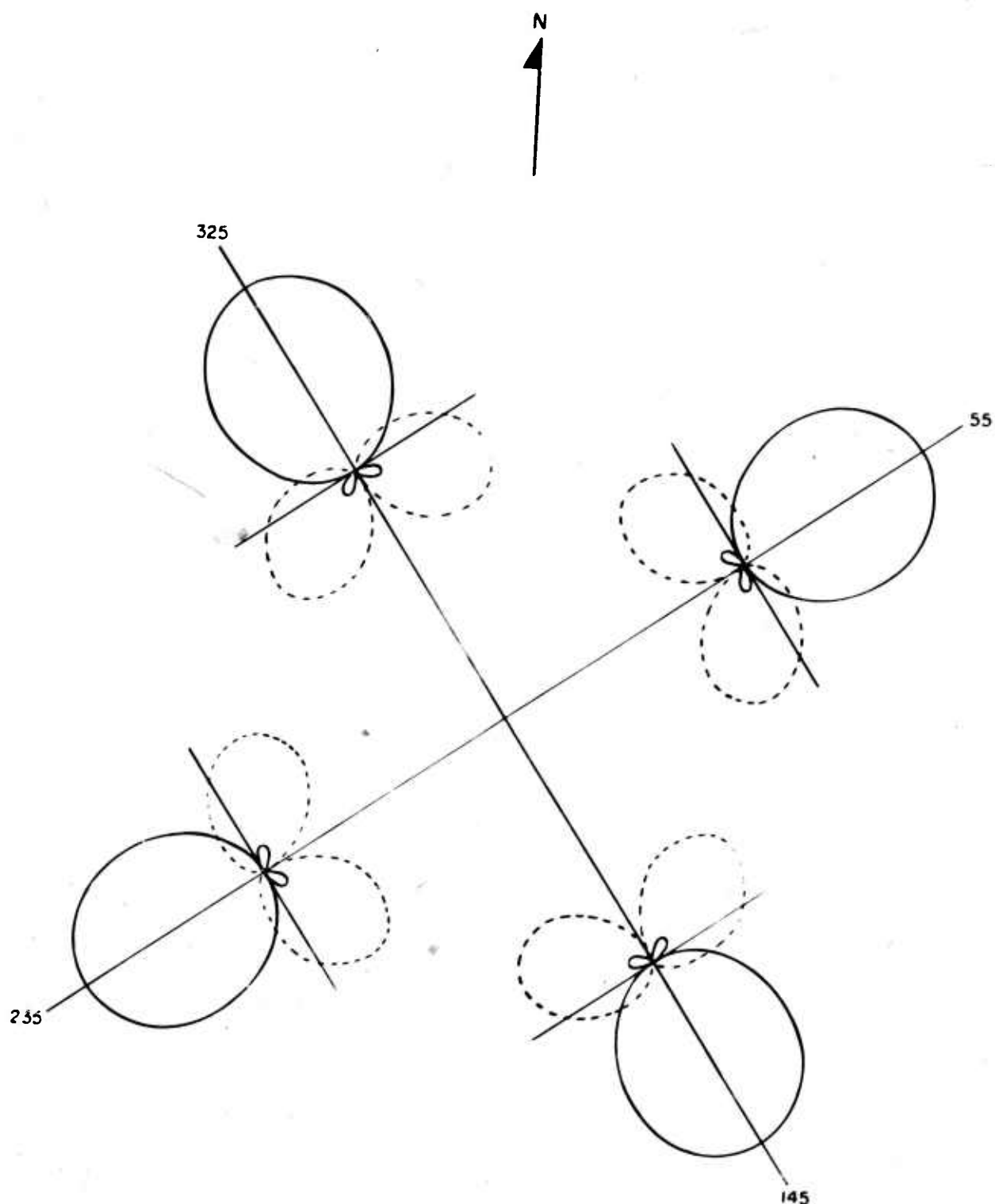


Figure 7. Four beam azimuthal array at QC-AZ. Solid lines are response to Rayleigh and horizontal component of P and SV waves; dashed lines are response to Love, G, and SH waves.

Table 1. Relative response of strain/inertial  
complex to two earthquakes

	EVENT 1	EVENT 2
LOCATION	SANDWICH ISLANDS	ALEUTIAN ISLANDS
DISTANCE	113.5 deg	50.6 deg
AZIMUTH (STATION- TO-EPICENTER)	142.5 deg	312.0 deg
$m_b$	6.0	5.4
RESPONSE IN 325 DEG AZIMUTH		
RAYLEIGH WAVES	0	1.9
LOVE WAVES	0	0
RESPONSE IN 145 DEG AZIMUTH		
RAYLEIGH WAVES	2.0	0
LOVE WAVES	0	0
RESPONSE IN 55 DEG AZIMUTH		
RAYLEIGH WAVES	0	0
LOVE WAVES	0.95	1.17
RESPONSE IN 235 DEG AZIMUTH		
RAYLEIGH WAVES	0	0.25
LOVE WAVES	1.05	0.75

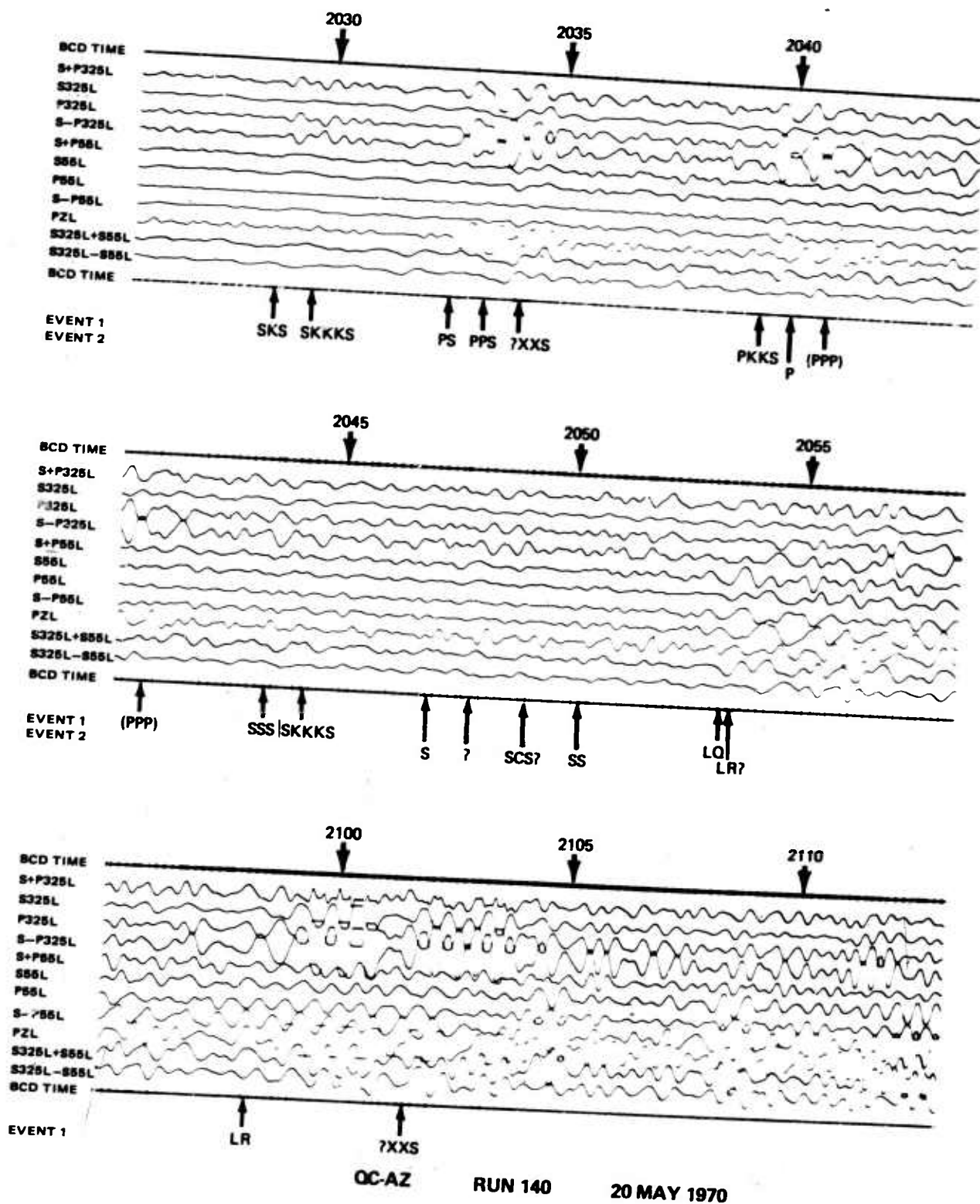


Figure 8. Magnetic tape playback of arrivals from interfering events. Event 1:  $\theta = 2003:42.2$ , south Sandwich Island region,  $h = 70$  km,  $m_b = 6.0$ ,  $\Delta = 113.5$  deg, azimuth =  $142.5$  deg; event 2:  $\theta = 2030:54.7$ , Andeanoff Island,  $h = 48$ ,  $m_b = 5.7$ ,  $\Delta = 50.6$  deg, azimuth =  $312.0$  deg

G 6011



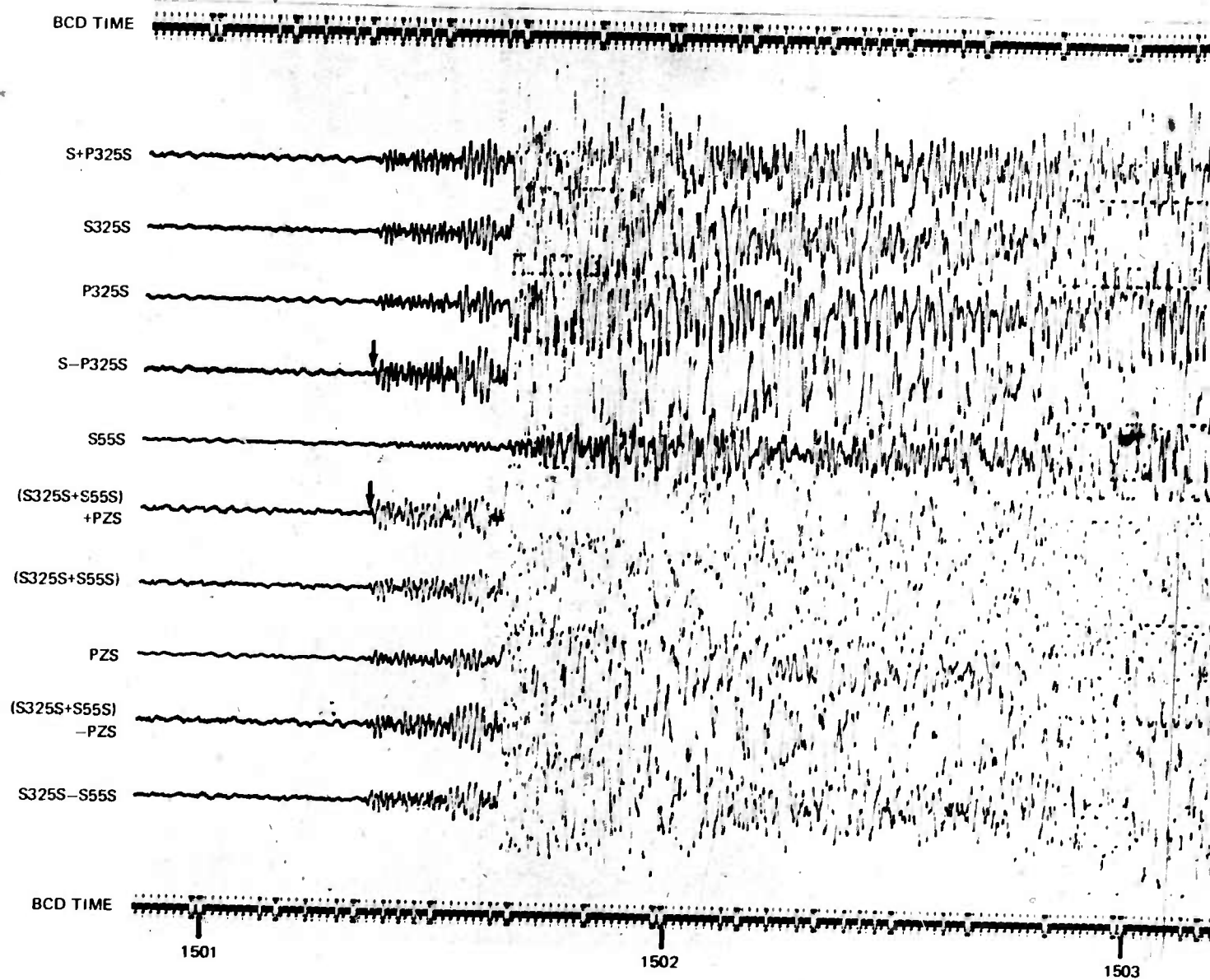
The arrival times of many earthquake phases are enhanced considerably with wave identification clarified and in many cases the time breaks are sharpened for accurate timing. Earthquake phases are identified in the figure with the phases from event 1 on the upper line and from event 2 on the lower line.

All of the arrivals from event 2 are smaller than those from event 1. Several arrivals are particularly interesting. The time break is sharpened for PS and PPS on S-P325L at 2032:37 and 2033:23. An unidentified phase arrival is detected on the PZL and S-P325L at 2034:08. The SSS and SKKKS arrivals are detected on S-P325L and can be timed at 2043:24 and 2044:18. The arrival of the LQ Love wave from event 1 is enhanced on the S-P55L at about 2053. The possible arrival of LRI Rayleigh wave from event 2 at about 2053 is indicated by possible signals on S+P325L, S+P55L (?), PZL, and S325L+S55L. The LRI Rayleigh wave from event 1 at 2058 is enhanced on the S-P325L and cancelled on the S+P325L even with the magnetic tape recorder clipping. Many body phases are detected as arriving after the times for presently tabled phases. These phases are probably either (a) multiple core reflections, (b) second reflected phases arriving by the long arc, and/or (c) thrice reflected phases arriving by the short or long arc. Some of these body phase arrivals are:

<u>Suspected type of arrival</u>	<u>Nearest minute</u>	<u>Channel detecting phase</u>
P	2101	PZL, S325L, S-P325L?
S	2101	S325L-S55L, S-P325L?
P or S?	2103	PZL, S325L+S55L S325L-S55L, S-P325L
P	2104	S-P325L, S-P55L S325L+S55L, PZL
P or S?	2105	PZL, S-P325L, S+P55L S325L+S55L, S325L-S55L
P or S?	2108	S-P55L, S325L+S55L, PZL
P or S?	2109	PZL, S-P325L, S-P55L S325L-S55L

## 11.2 ENHANCEMENT OF SHORT-PERIOD WAVES

Although the primary objective of Project VT/8706 is to develop methods of long-period wave discrimination, magnetic tape recordings are being made of short-period (SP) inertial and strain seismographs. The SP strain and inertial seismographs can be added and subtracted for the same azimuthal response as shown in figure 7. Two examples of enhancement accomplished with the short-period systems are shown in figures 9 and 10. At the time of these recordings the P55S inertial seismograph was inoperational. Magnifications for



QC-AZ  
MAGNETIC  
TAPE PLAYOUT  
RUN 111  
21 APRIL 1970

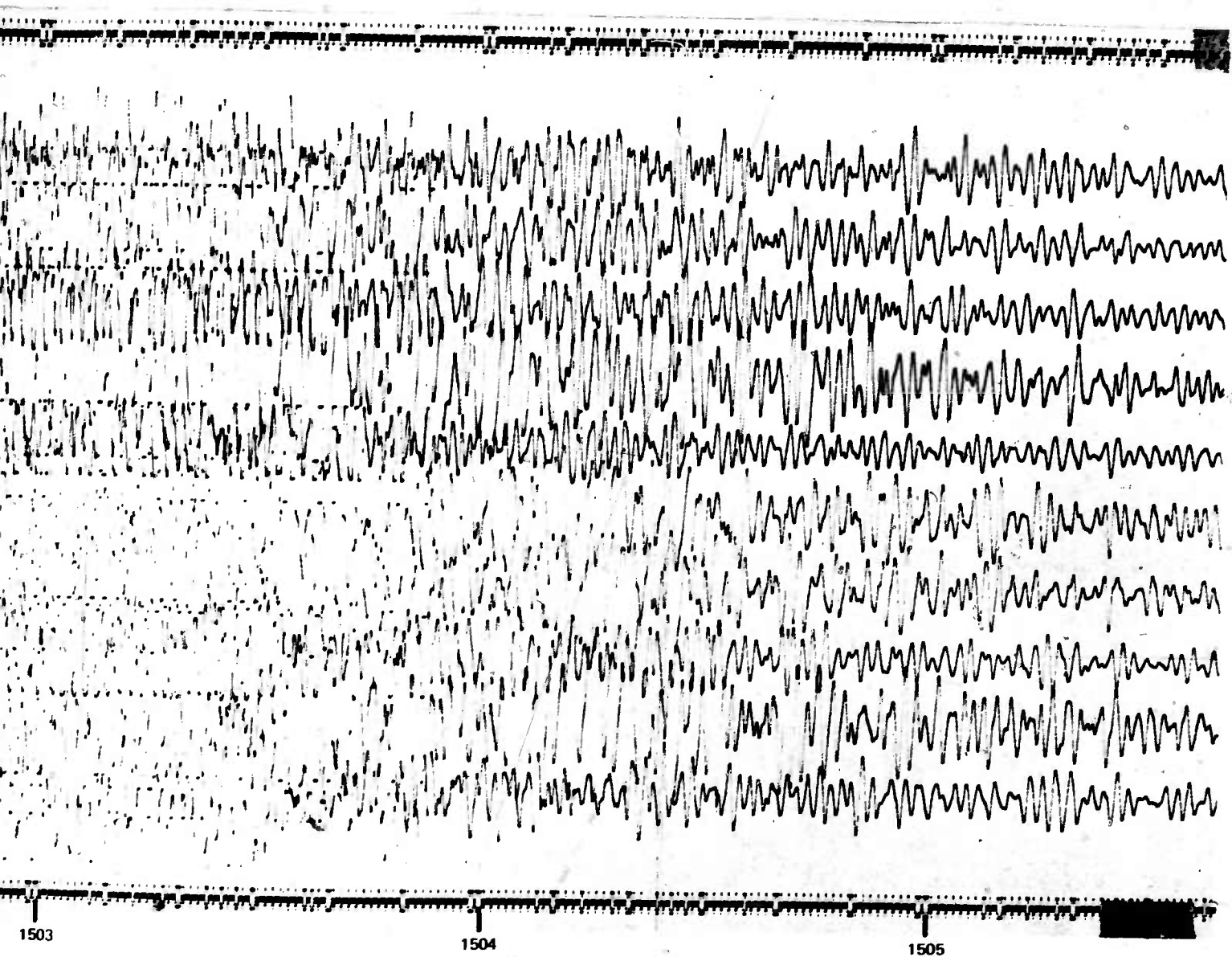
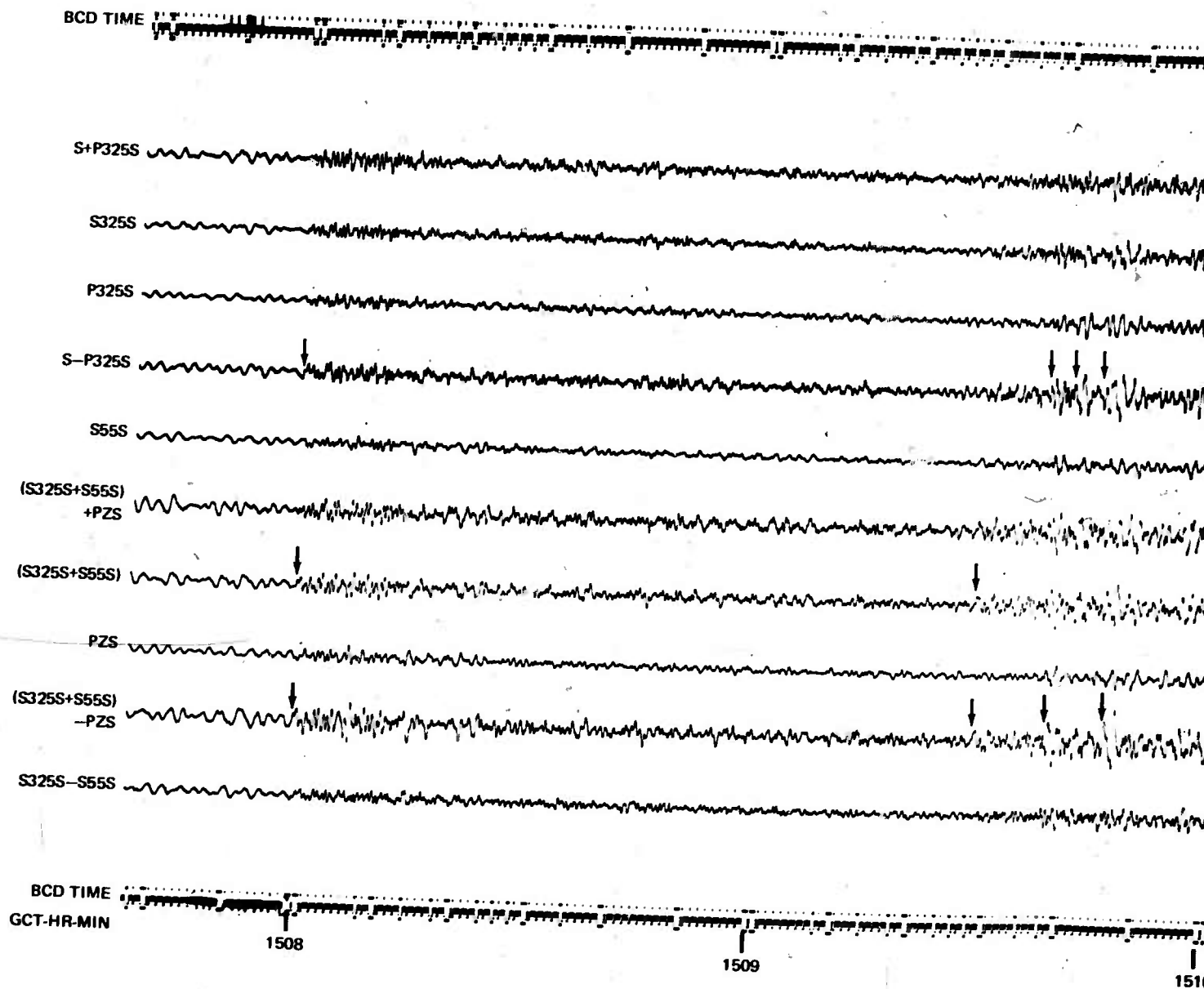


Figure 9. Enhancement of short-period arrivals from an explosion



QC-AZ  
MAGNETIC  
TAPE PLAYOUT  
RUN 111  
21 APRIL 1970

TRACE	MAG.
GCT	AT 25 SEC
HR MIN	
DAY	
FLAG	
WV	
S325L2	
S325LL2	
S325L1	3.72 X 10 <sup>-13</sup> STRAIN/MM
S325LL1	1.57 X 10 <sup>-11</sup> STRAIN/MM
S55L	4.63 X 10 <sup>-13</sup> STRAIN/MM
S55LL	8.05 X 10 <sup>-12</sup> STRAIN/MM
PZL	122K
P325L	122K
P55L	113K
PZX	18.5K
P325X	18.0K
P55X	31.4K
ML1	0.057/μBAR/MM
•PZS	459K
WV	2 MPH/MM
•P325S	370K
ML2	3.5/μBAR/MM
WD	

-27-

NOTE: • MAG. AT 1 SEC

TR 70-29

QC-AZ  
CAMERA 1  
RUN 121  
1 MAY 1970

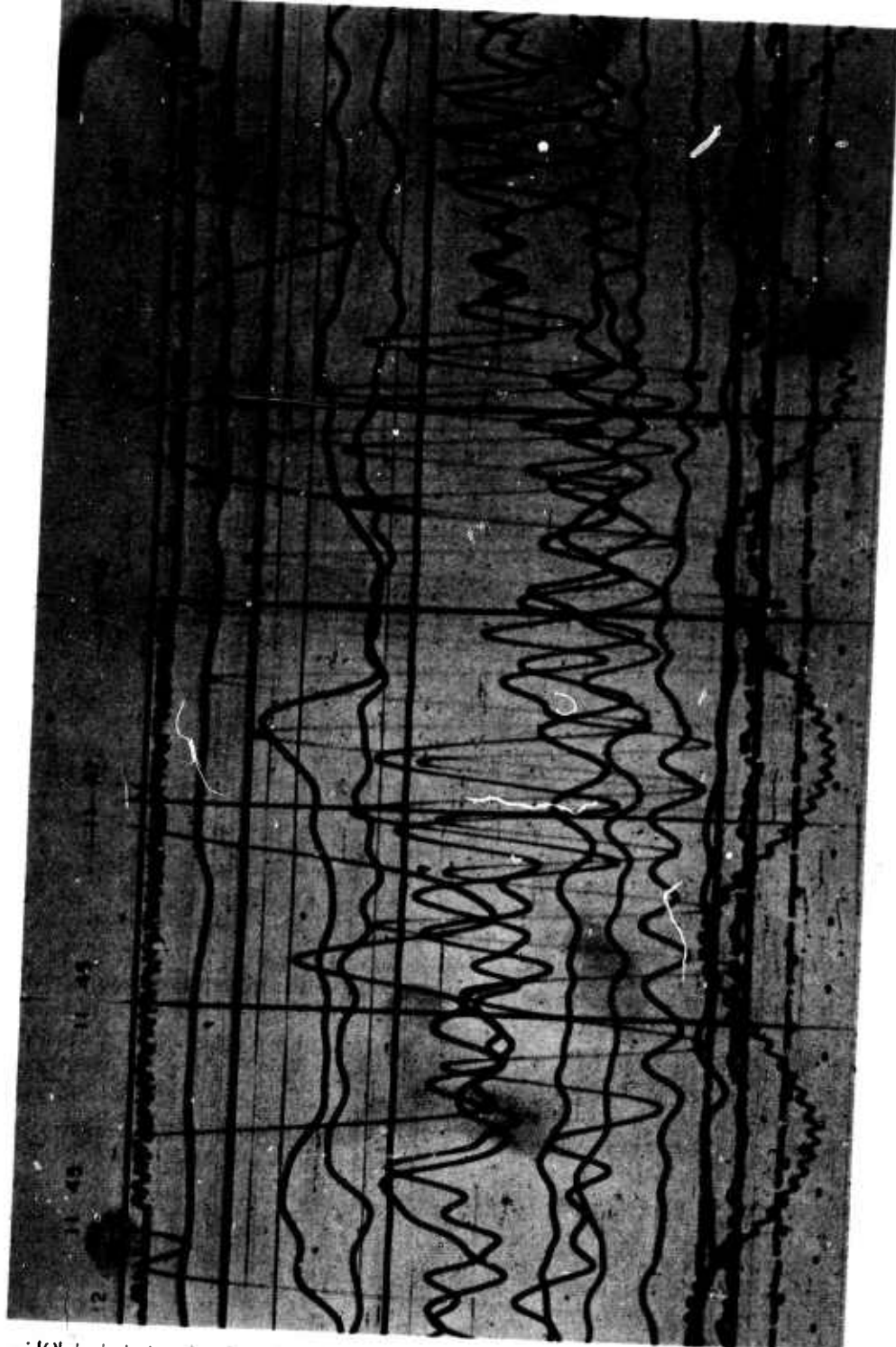


Figure 11. Reproduction of 16 mm film recording of LQ1 Love wave and LR1 Rayleigh wave. USC&GS preliminary epicenter data: 0 = 1131:34.3, 14.7N, 92.9W, near cost of Chiapas, Mexico, h = 68, m<sub>b</sub> = 4.0, Δ = 25.1 deg, azimuth = 132.8 deg

Figure 12 illustrates the LQ1 Love wave from a magnitude 4.1 event in the Greenland Sea at an epicentral distance of 61.9 deg. There are large 100 sec pressure variations causing tilting which are recorded on the horizontal inertial seismographs and ground strain recorded on the strain seismographs.

Two weeks later the second Develocorder was operational and on-line sums and differences were being recorded. Figure 13 is the recording of the Rayleigh wave train from a magnitude 5.0 earthquake near New Britain Island at an epicentral distance of 98 deg and an azimuth of 270 deg. This magnitude event from the south Pacific is always well recorded. Figure 14 is a reproduction from camera 2 for the same event. At the time of this recording, the magnifications had not been determined on this camera and the strain and pendulum traces were not equally contributing to the sums and differences. However, the Rayleigh wave is seen to be greatly enhanced on the S55L+P55L trace. Both the S325L1 and S325L2 were not operating properly during this recording.

Figure 15 illustrates recording of a Rayleigh wave train from a magnitude 4.4 earthquake off the coast of Ecuador at an epicentral distance of 42 deg and an azimuth of 135 deg. The six inertial seismograph traces are all overlining and the two 325 deg azimuth strain seismographs are responding to the Rayleigh wave. The camera 2 recording of the same event is shown in figure 16. The S325L2-P325L difference trace is showing good enhancement. The S55L and P55L seismographs were not contributing equally to the sum and difference and the enhancement does not show as well on these traces.

Figures 17 and 18 are reproductions of recordings from cameras 1 and 2, respectively, of a magnitude 4.2 earthquake in Turkey at an epicentral distance of 99.5 deg and an azimuth of 29.6 deg. In figure 17, the event would possibly not be detected if only the ALPS response inertial seismographs were present. However, the 30 sec signals are seen more clearly on the extended-long-period (XLP) response because the large microseisms present at this time have been eliminated by the XLP response. Even so, the detection of this event would still be questionable except for the clear enhancement in figure 18 on the S325L1-P325L and on the S55L-P55L difference traces and the clear cancellation on the two sum traces. Note also that the 8 sec microseisms are enhanced on the S55L+P55L sum and generally cancelled on the difference trace. (The camera drive was erratic between 0610 and 0611.)

Figure 19 is a copy of a magnetic tape payout from a recording of the Rayleigh wave from a magnitude 5.3 earthquake in the Tonga Island Region at an epicentral distance of 78.9 deg and an azimuth of 238 deg. This figure illustrates the 90 deg phase difference, in accord with theory, between the vertical inertial seismograph PZL and the sum of the two orthogonal strain seismographs S325L1+S55L. The success of this comparison suggests that the vertical strain seismograph will be a valuable addition to the QC-AZ instrumentation complex.



TR 70-29

Figure 12. Reproduction of 16 mm film recording of surface wave. USC&GS preliminary epicenter data:  $0 = 1058:03.5$ ,  $79.7N$ ,  $3.5E$ , Greenland Sea,  $h = N$ ,  $m_b = 4.1$ ,  $\Delta = 61.9$  deg, azimuth =  $10.6$  deg

QC-AZ  
CAMERA 1  
RUN 123  
3 MAY 1970

TRACE	MAG.
GCT	AT 25 SEC
HR MIN	—
DAY	—
WV	—
FLAG	—
S325L2	1.71 X 10 <sup>-12</sup> STRAIN/MM
S325LL2	1.71 X 10 <sup>-11</sup> STRAIN/MM
S325L1	
S325LL1	1.19 X 10 <sup>-11</sup> STRAIN/MM
S55L	1.86 X 10 <sup>-12</sup> STRAIN/MM
S55LL	1.14 X 10 <sup>-11</sup> STRAIN/MM
PZL	46.6K
P325L	55.8K
P55L	51.5K
PZX	29.9K
P325X	34.2K
P55X	19.3K
ML1	0.057μBAR/MM
•PZS	191K
•P325S	177K
WV	2 MPH/MM
ML2	3.5μBAR/MM
WD	—

NOTE: • MAG. AT 1 SEC

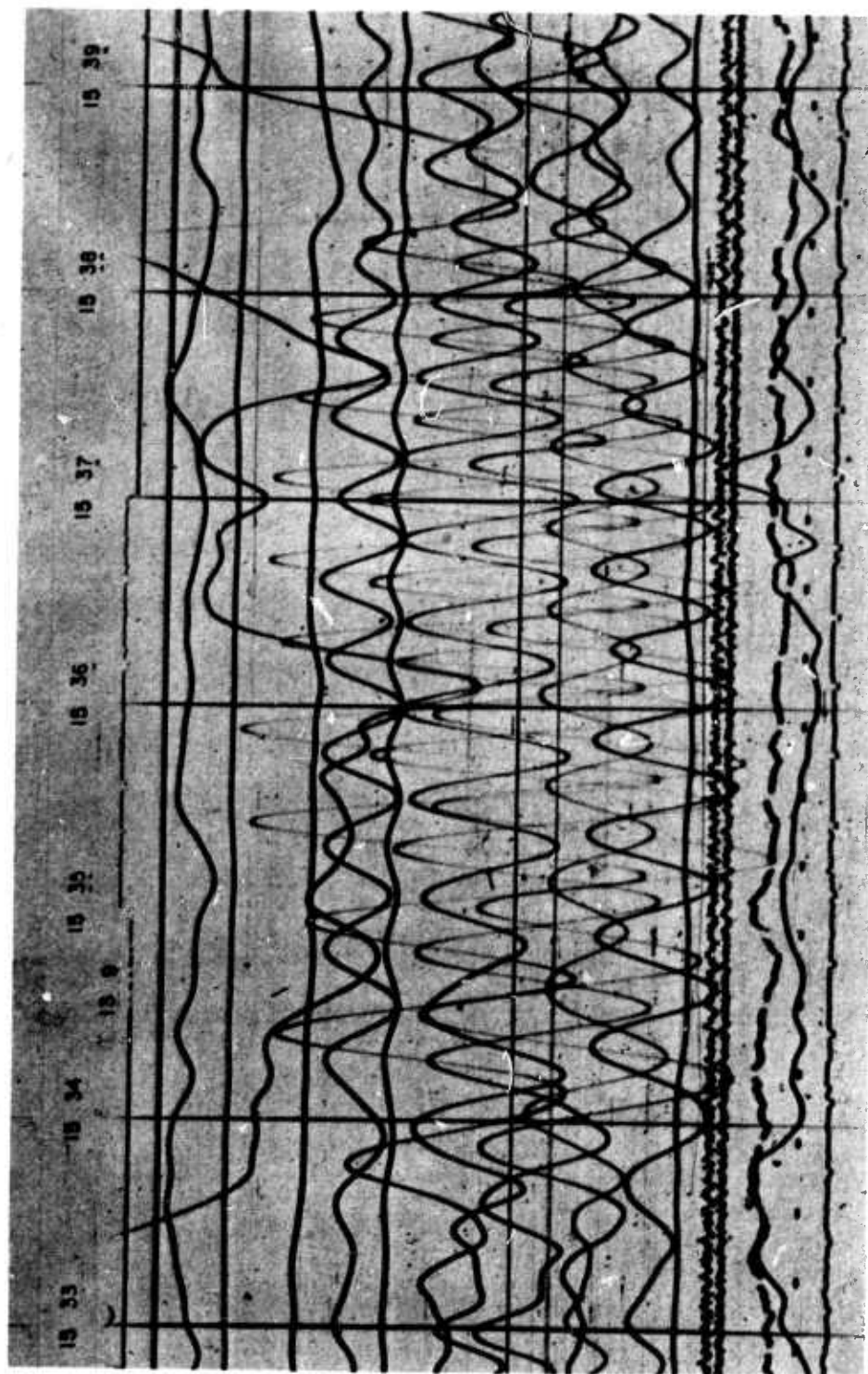


Figure 13. Reproduction of a 16 mm film recording of a Rayleigh wave train from an earthquake near New Britain Island.  $\Delta = 1448:38$ ,  $5.1S$ ,  $152.1E$ ,  $h \approx 70$ ,  $m_b = 5.0$ ,  $\Delta \approx 98$  deg, azimuth  $\approx 270$  deg.

QC-AZ  
CAMERA 1  
RUN 139  
19 MAY 1970



MAG.  
TRACE AT 25 SEC

GCT  
HR MIN  
DAY  
WWV  
S325L1-S55L  
S325L2+S325L1+S55L  
S325L1+S55L  
S325L2  
PZL  
S325L1+P325L  
S325L1  
P325L  
S325L1 P325L  
S55L+P55L  
S55L  
P55L  
S55L P55L  
ML1

OC-AZ  
CAMERA 2  
RUN 139  
19 MAY 1970

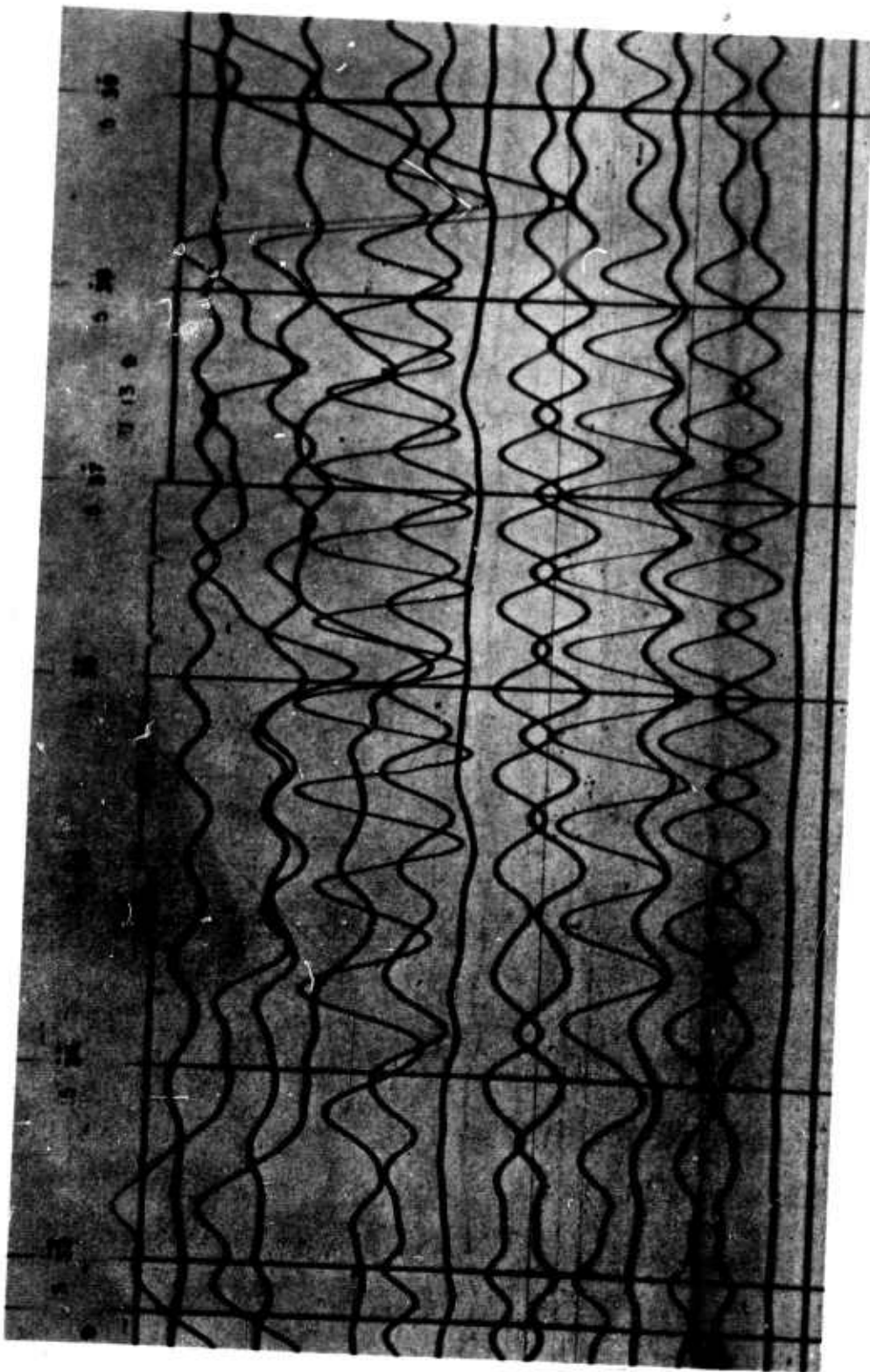


Figure 14. Reproduction of a 16 mm film recording of a Rayleigh wave train from an earthquake near New Britain Island.  $\theta = 1448:38$ ,  $5.1S$ ,  $152.1E$ ,  $h \approx 70$ ,  $m_b = 5.0$ ,  $\Delta \approx 98$  deg, azimuth  $= 270$  deg.

TRACE	MAG.
GCT	AT 25 SEC
HR MIN	-
DAY	-
WV	-
FLAG	-
S325L2	1.62 X 10 <sup>-12</sup> STRAIN/MM
S325LL2	1.62 X 10 <sup>-11</sup> STRAIN/MM
S325L1	1.26 X 10 <sup>-12</sup> STRAIN/MM
S325LL1	2.43 X 10 <sup>-11</sup> STRAIN/MM
S55L	1.19 X 10 <sup>-12</sup> STRAIN/MM
S55LL	1.14 X 10 <sup>-11</sup> STRAIN/MM
PZL	39.6K
P325L	52.2K
PZX	26.4K
P325X	33.3K
P55L	1.26K
ML1	0.057μBAR/MM
•PZS	97.4K
•P55X	66.8K
•P325S	90.5K
WV	2 MPH/MM
ML2	3.5μBAR/MM
WD	-

-32-

NOTE: \* MAG. AT 1 SEC

OC-AZ  
CAMERA 1  
RUN 142  
22 MAY 1970

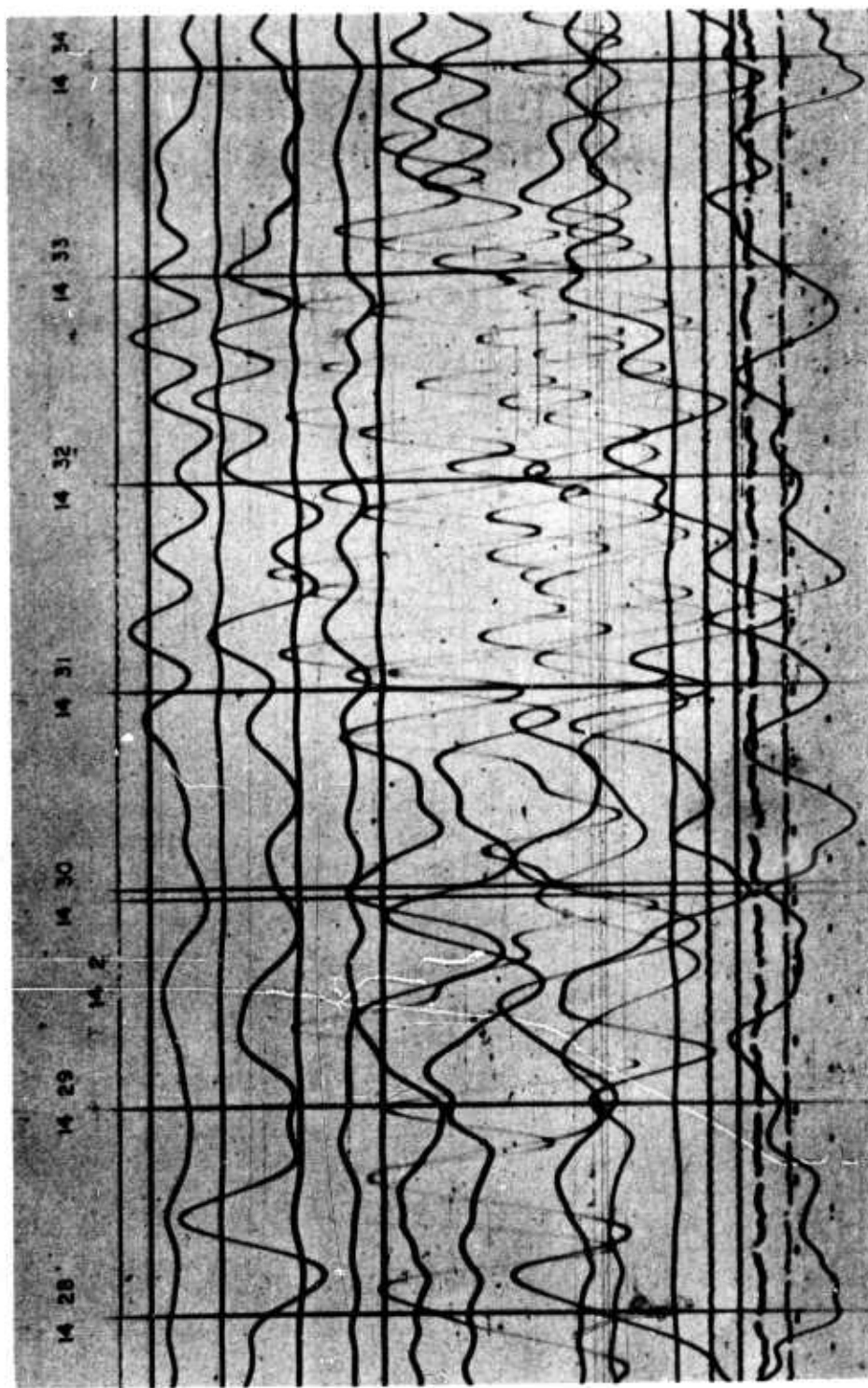


Figure 15. Reproduction of a 16 mm film recording of a Rayleigh wave train from an earthquake off the coast of Ecuador.  $\Delta = 1408:54$ ,  $2.5N$ ,  $83.0W$ ,  $h = ?$ ,  $m_b = 4.4$ ,  $\Delta = 42$  deg, azimuth  $\approx 135$  deg.

EQUIV.  
INERTIAL  
MAG.  
RAYLEIGH  
WAVE

TRACE

AT 25 SEC

HR MIN	-
DAY	-
WVV	-
S325L2-S55L	34.2K
OFF	-
S325L2+S55L	48.7K
S325L1	28.6K
PZL	21.1K
S325L2+P325L	40.7K
S325L2	21.7K
P325L	22.5K
S325L2-P325L	51.1K
S55L+P55L	91.0K
S55L	36.2K
P55L	56.4K
S55L-P55L	82.3K
ML1	-
-	-

QC-AZ  
CAMERA 2  
RUN 142  
22 MAY 1970

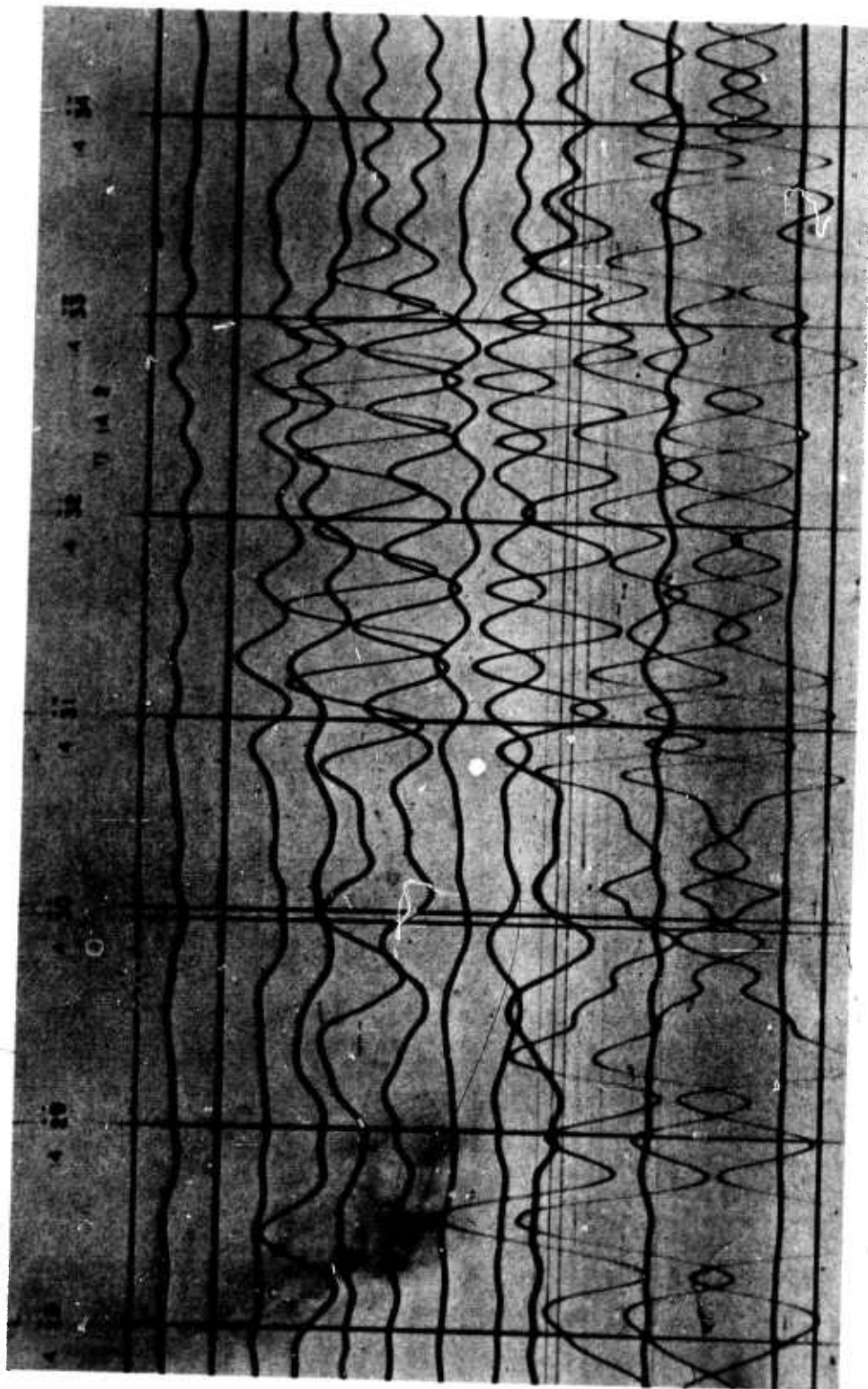


Figure 16. Reproduction of a 16 mm film recording of a Rayleigh wave train from an earthquake off the coast of Ecuador.  $\theta = 1408:54$ ,  $2.5N$ ,  $83.0W$ ,  $h = ?$ ,  $m_b = 4.4$ ,  $\Delta \pm 42$  deg, azimuth  $\pm 135$  deg.

TRACE	MAG.
GCT	AT 25 SEC
HR MIN	-
DAY	-
WVW	-
FLAG	-
S325L2	1.11 X 10 <sup>-12</sup> STRAIN/MM
S325LL2	1.19 X 10 <sup>-11</sup> STRAIN/MM
S325L1	1.05 X 10 <sup>-12</sup> STRAIN/MM
S325LL1	1.09 X 10 <sup>-11</sup> STRAIN/MM
S55L	1.25 X 10 <sup>-12</sup> STRAIN/MM
S55LL	1.19 X 10 <sup>-11</sup> STRAIN/MM
PZL	51.2K
P325L	50.0K
P55L	43.0K
PZX	45.8K
P325X	48.6K
P55X	42.0K
ML1	0.057μBAR/MM
• PZS	487K
• P325S	462K
WV	2 MPH/MM
WD	-
ML2	3.5μBAR/MM

NOTE: • MAG. AT 1 SEC

QC-AZ  
CAMERA 1  
RUN 161  
10 JUNE 1970

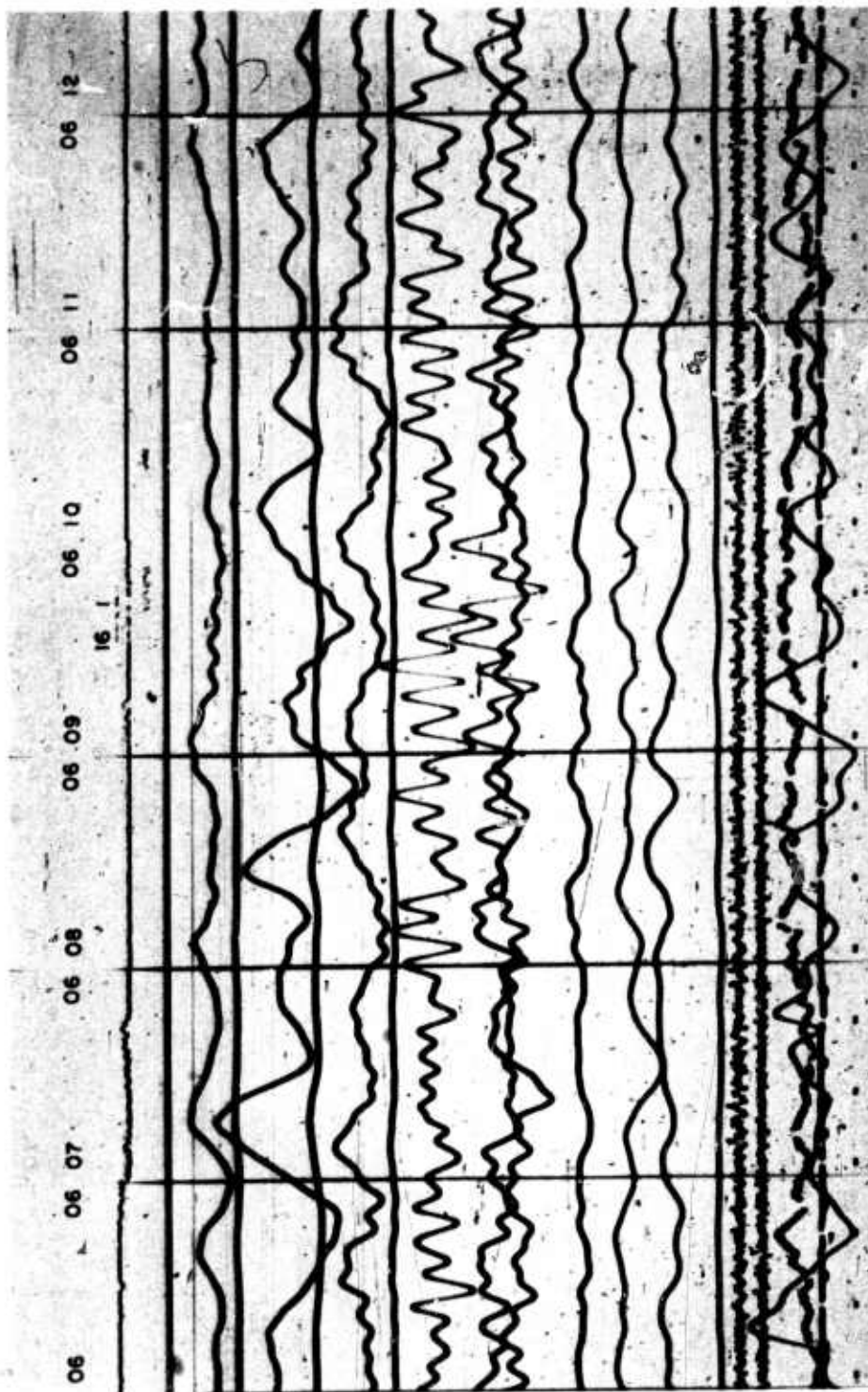


Figure 17. Reproduction of 16 mm film recording of LR1 Rayleigh wave. USC&GS preliminary epicenter data:  $0 = 0517.14.0$ ,  $39.2N$ ,  $29.5E$ , Turkey,  $h = 27$  km,  $m_0 = 4.2$ ,  $\Delta = 99.5$  deg, azimuth =  $29.6$  deg



TRACE  
GCT  
HR MIN  
DAY  
WWV  
(S325L1-S325L2)  
S325L1-S55L  
S325L2-S55L  
S325L2  
PZL  
S325L1+P325L  
S325L1  
P325L  
S325L1-P325L  
S55L+P55L  
S55L  
P55L  
S35L-P55L  
ML1

..  
AT 25 SEC  
-  
-  
-  
~500K  
51.3K  
57K  
-  
19.7K  
63.0K  
32.9K  
31.3K  
61.3K  
53.5K  
31.1K  
26.2K  
54.1K  
0.050uBAR/MM

-35-

..EQUIV.  
INERTIAL  
MAG.  
RAYLEIGH  
W/°E

QC-AZ  
CAMERA 2  
RUN 161  
10 JUNE 1970

TR 70-29

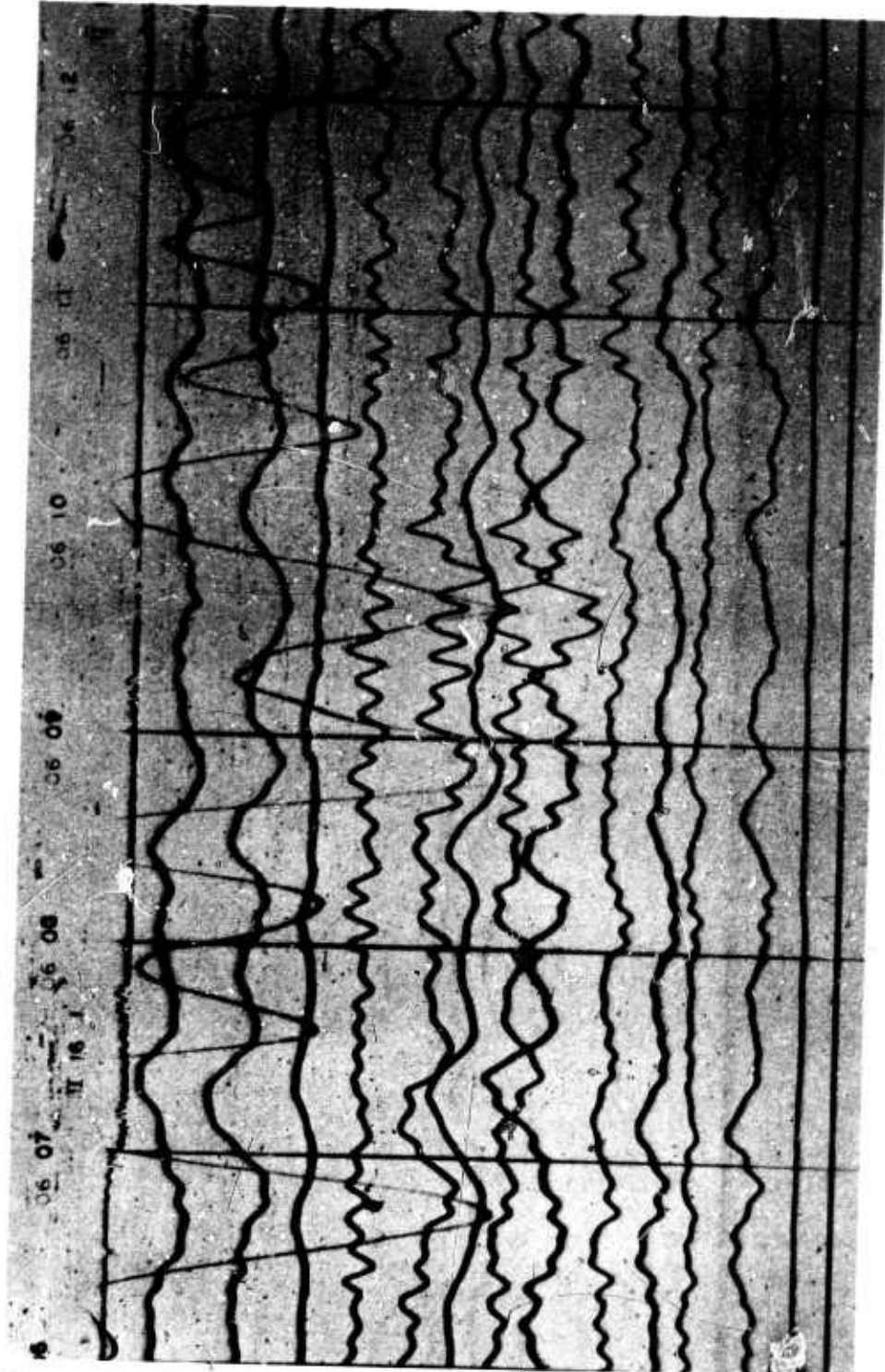


Figure 18. Reproduction of 16 mm film recording showing enhancement of LR1 Rayleigh wave on S325L-P325L and S55L-P55L difference traces. USC&GS preliminary epicenter data:  $\theta = 0517:14.0$ ,  $39.2N$ ,  $29.5E$ , Turkey,  $h = 27$  km,  $m_b = 4.2$ ,  $\Delta = 99.5$  deg, azimuth =  $29.6$  deg

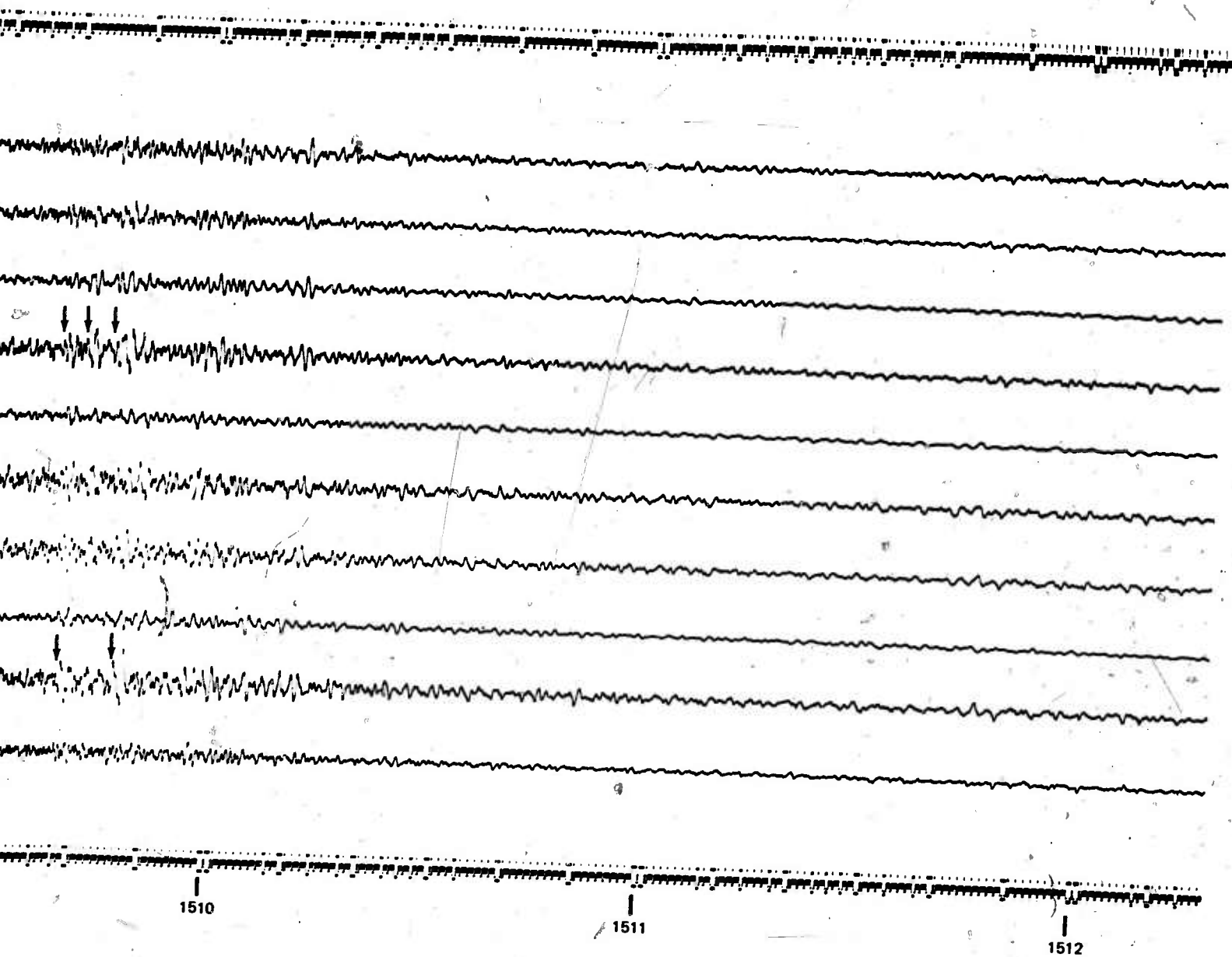


Figure 10. Enhancement of short-period arrivals from an earthquake during the coda of an earlier event

these recordings are not known but based on the amplitude of the microseisms the magnifications are estimated to be about 200K in both figures. Figure 9 is a reproduction of the playout made from magnetic tape No. 2 for 21 April 1970. The USC&GS PDE card data for this event are:

0 = 1500:00.0, 37° 06'50.0" N, 116° 04'51.0"W, Nevada Test Site (NTS) event "CAN",

h = 0,  $m_b$  = 4.8,  $\Delta$  = 5.5 deg = 613 km, azimuth station-to-epicenter = 318.5 deg.

The vertical strain seismograph is formed by the sum of the perpendicular horizontal strain seismographs. Very clear arrival times can be picked for the initial Pn arrival on the S-P325S and the (S325S+S55S) +PZS traces. These traces show much sharper first breaks than the P325S and PZS inertial traces. A second P arrival is clearly detected between the Pn and Pg. The arrival of the Sg-Lg phases at 1502:50 saturates the magnetic tape recorder electronics. Several distinct P and several distinct S arrivals can be seen in the coda after the electronics stopped clipping. Times were picked from a high speed playout and the travel time was divided by the distance to obtain an estimate of a minimum P or S velocity for various layers between NTS and QC-AZ for the following arrivals:

<u>Phase</u>	<u>Travel time/distance</u>
Pn <sub>1</sub>	7.534 km/sec
Pn <sub>2</sub>	7.474 km/sec
P <sub>1</sub>	6.662 km/sec
Pg	6.207 km/sec
Sn?	3.996 km/sec
Sg-Lg <sub>1</sub>	3.597 km/sec
Sg-Lg <sub>2</sub>	3.557 km/sec

During the Lg coda from the explosion, arrivals were recorded from an earthquake located by the United States Geological Survey (USGS) close-in network near Rangely, Colorado (see figure 10). The USC&GS PDE card data are: 0 = 1505:47.5, 40°05.39'N, 108° 53.87W, Rangely, Colorado, h = 4 km,  $m_b$  = 4.6,  $\Delta$  = 7.2 deg = 804 km, azimuth = 16.9 deg. The Pn (or P<sub>1</sub>) phase is recorded with an impulsive break on the S-P325S, S325S+S55S, and the (S325S+S55S) -PZS traces about 3 sec before the Pg phase. Several S and surface wave phases including Sn are clearly enhanced. The travel time divided by the distance is:

<u>Phase</u>	<u>Travel time/distance</u>
Pn(or P <sub>1</sub> )	6.101 km/sec
Pg	5.983 km/sec
Sn <sub>1</sub>	3.655 km/sec
Sn <sub>2</sub>	3.640 km/sec
Sn <sub>3</sub>	3.631 km/sec
Sg-Lg <sub>1</sub>	3.486 km/sec
Sg-Lg <sub>2</sub>	3.478 km/sec

The travel times and velocities between Rangely, Colorado, and QC-AZ are considerably slower than the travel times from NTS to QC-AZ. To the authors' knowledge, the above observations are the first reported Sn travel times in the Basin and Range Province.

### 11.3 ENHANCEMENT OF SURFACE WAVES AND DETECTION OF LOW LEVEL SIGNALS

Several examples of recordings of surface waves and the detection of low level signals are illustrated in this section. These examples are shown as a collection of individual record sections and do not represent a unified study. During much of the time covered by this report, installation of instruments was the primary goal and perfectly calibrated recordings with equalized gains and correct polarities was of secondary importance. Accurate location of epicenters is not available for several weeks after the events; therefore, several earlier recordings have been used to give a preliminary demonstration of the QC-AZ detection threshold. In the group of recordings presented, an improvement in record quality and a decrease in instrument noise can be seen as time progresses.

Figure 11 is a recording typical of the many earthquakes that occur near Chiapas, Mexico. A very clear, large amplitude slightly dispersed Love wave on the P55L and P55X precedes the larger amplitude Rayleigh wave on the PZL, P325L, PZX, and P325X. The S325L had been set at too high a magnification during this recording period. The S55L did not record the Rayleigh wave because it is almost transverse to the wave motion and on a null for both Love and Rayleigh waves. The large recorder amplitude at which this magnitude 4.0 event from an epicentral distance of 25.1 deg is a good example of the capabilities of the ALPS response inertial system which has a magnification of 113 to 122K in the X10 reproduction in figure 11. The ML2 microbarograph outside the mine is being calibrated with a 65  $\mu$ bar input at 112 sec and with a 9  $\mu$ bar input at 4.9 sec periods.



EQUIV.  
INERTIAL  
MAG.  
RAYLEIGH  
WAVE

TRACE  
REF. NO. AT 25 SEC  
DAY

BCD  
TIME

S325L1 18.2K

S55L 18.6K

S325L1 + S55L 36.8K

S325L1 - S55L 36.8K

PZL 17.6K

BCD  
TIME

QC-AZ  
MAGNETIC TAPE  
PLAYOUT  
RUN 101  
11 APRIL 1970

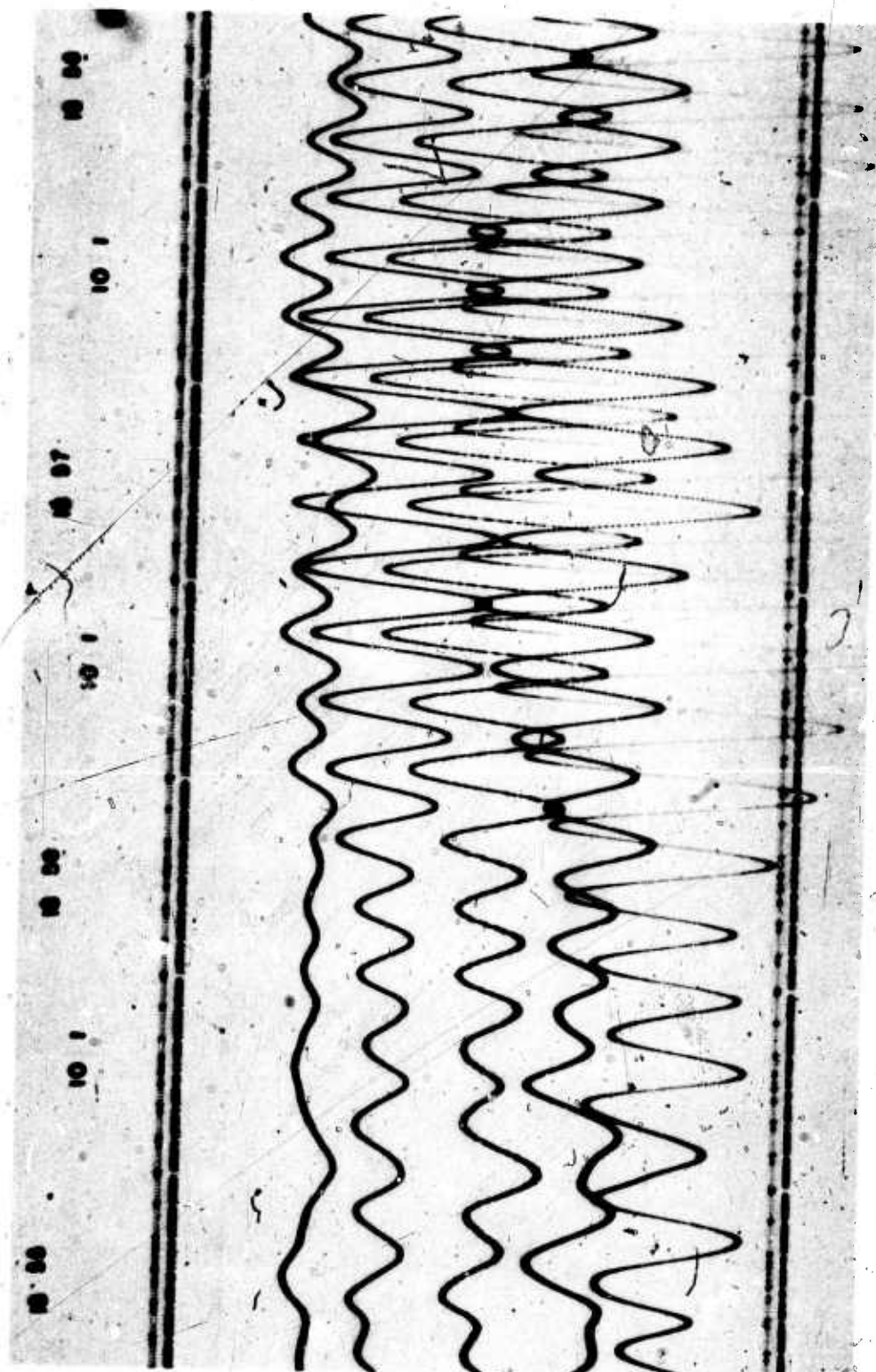


Figure 19. Reproduction of a 16 mm film recording of a Rayleigh wave train from an earthquake in the Tonga Island Region.  $\theta = 0621:16.3$ ,  $19.3S$ ,  $173.6W$ ,  $h = 33$ ,  $m_p = 5.3$ ,  $\Delta = 78.9$  deg, azimuth =  $238$  deg.

#### 11.4 COMPARISONS BETWEEN THE PARALLEL STRAIN SEISMOGRAPHS

This section describes the preliminary results of an experiment to compare the two parallel horizontal strain seismographs S325-1 and S325-2. The comparisons are made with the Advanced Long-Period System (ALPS) response between 1 and 256 sec and between 20 and 2560 sec, and with the ultra-long-period (ULP) response between 20 and 2560 sec. The comparisons are made under three conditions: first, with a low wind velocity and low-to-moderate microbarographic activity; second, with a high wind velocity and large microbarographic disturbances; and, third, with large earthquake signals. In addition to comparisons between the two parallel strain seismographs, some comparisons are made with the parallel inertial seismograph P325L and with the perpendicular strain seismographs S55L and S55U. In section 11.5.2 the strain seismographs S325U1 and S55U are related to the ML2 microbarograph outside the mine. The comparisons are quantitized with power spectral densities, cross power spectral densities, coherence, and relative phase angle. Table 2 is a list of the instrumentation systems compared and the figure numbers for corresponding plots.

##### 11.4.1 Spectral Analysis Presentation

All of the time series analysis plots are similar. Part a of the figure is the power spectral density of the two seismograms and the cross power spectral density between them. Part b of the figures is the coherence and part c is the relative phase angle. (Note part b is coherence not coherence squared.) Long time series and a small number of lags were used for good statistical stability. Time samples of 33.1 min (with 128 lags) or 32.0 min (with 256 lags) were used for spectra between 1 and 256 sec periods and time samples of 6.7 hr (with 128 lags) were used for spectra between 20 and 2560 sec periods. In general, the shorter period spectra were calculated with 256 lags, but in a few cases, they were also calculated with 128 lags for greater smoothing and a smaller confidence limit.

The spectra are uncorrected for system responses and are calibrated relative to earth strain or earth displacement at 25 sec for the ALPS response and at 100 sec for the ULP response. Thus, if the reader wishes to estimate the power spectral density of ground strain or ground displacement at another period, the calibration values in the figures should be divided by the square of the ratio of the response of the system at the desired period to the response of the system at the calibration period of 25 or 100 sec. In the figures in which strain is compared to displacement, the strain has been normalized to displacement based on a 25 sec Rayleigh wave phase velocity of 4.00 km/sec and the resulting power ratio of  $(6.28 \times 10^{-5})^2 \text{ strain}^2/\text{m}^2$ . Cross power spectral density between strain and displacement is normalized based on a power ratio of  $6.28 \times 10^{-5} \text{ strain} \cdot \text{m}/\text{m}^2$ . The spectra are presented as a power spectral density normalized to a 1 Hz passband. The passband used in the actual calculations was either  $1/128 = 7.81 \times 10^{-3} \text{ Hz}$ ,  $1/256 = 3.91 \times 10^{-3} \text{ Hz}$ , or  $1/2560 = 3.91 \times 10^{-4} \text{ Hz}$ . If the reader wishes to normalize to a passband of 1 mHz =  $1/1000 \text{ Hz}$  for comparison with several published microseismic spectra, the plotted values can be divided by 1000.

Table 2. Instrumentation systems compared

<u>Signal condition</u>	<u>System 1</u>	<u>System 2</u>	<u>Period range (sec)</u>	<u>Figure no.</u>
Low wind	S325L1	S325L2	1-256	21
	S325L1	S325L2	1-128	22
	S325L1	P325L	1-256	23
	S325L1	P325L	1-128	24
	S325L1	S55L	1-256	25
High wind	S325L1	S325L2	1-256	27
	S325L1	S325L2	20-2560	28
	S325U1	S325U2	20-2560	29
	S325L1	P325L	1-256	30
	S325L1	S55L	1-256	31
	S325U1	S55U	20-2560	32
Earthquake				
LR1 coda	S325LL1	S325LL2	1-256	33
LQ3, LR2, and LR3	S325LL1	S325LL2	1-256	35
LQ3, LR2, and LR3	S325LL1	S55LL	1-256	36
LR1	S325L1	S325L2	1-256	38
LR1	S325L1	S325L2	1-128	39
LR1	S325L1	P325L	1-128	40
High wind	S325U1	ML2	20-2560	42
	S55U	ML2	20-2560	43

Many of the spectra show 1 or 2 peaks at 1.7 and 3.2 sec. These peaks are the residual power noise in the playback and digitization electronics. Actual playback was at 100 times the field recording speed so a true 60 Hz noise at playback relates to an equivalent 0.6 Hz or 1.7 sec noise in the time scale of the field recorder.

Computational noise was also observed in the course of the calculations but is well below any meaningful data. The spectra are calculated using the fast Fourier transform (FFT) algorithm of Cooley and Tukey. A single FFT on the Geotech CDC 3100 computer has a noise about  $10^{12}$  to  $10^{13}$  below the largest number in the calculations. This error results in part from the fact that the FFT algorithm takes differences from almost equal numbers. The spectral program used employs three FFT and erratic results occur about  $10^5$  or  $10^6$  below the largest spectral number. These erratic results are interpreted as computational noise. When two time series are analyzed together with the cross spectral program using the FFT, they must be scaled so that their spectra are within the  $10^5$  to  $10^6$  range of no computational noise. The first cross spectra calculated comparing the inertial seismograph and the strain seismograph showed this noise since the strain power values are  $39.5 \times 10^{-10}$  smaller than the displacement values. In subsequent calculations the strain values were scaled to alleviate this numerical problem.

#### 11.4.2 Low Wind Conditions

A time interval was selected for the comparison when the two parallel strain seismographs were operating in a normal manner, when the wind was varying slowly between about 3 and 5 mph and when there was no apparent earthquake motion in the recordings. This time sample is typical of the QC-AZ microseismic background in May. Figure 20 is a portion of the time interval that was used for the comparison. While the strain seismographs were operating normally, the horizontal inertial seismographs had just had the magnets and coils changed and were still noisy, not having settled back to normal operation yet. The P325 seismometer was the last to be worked on and is the noisiest. In figure 20, the S325L1 and S325L2 are seen to have some similarities at the shorter periods and for the microseisms, but the S325L2 contains more longer period motion than the S325L1.

The total mean square strain (relative to 25 sec) in the passband of the seismograph during the sample analyzed was  $8.801 \times 10^{-25}$  strain<sup>2</sup> on the S325L1 and  $1.764 \times 10^{-24}$  strain<sup>2</sup> on the S325L2. The root-mean-square (RMS) motion in the seismograph passbands were  $9.38 \times 10^{-13}$  strain and  $1.33 \times 10^{-12}$  strain, respectively. The design goal for the strain seismographs was to detect, with a 1:1 signal-to-noise ratio, a  $5 \times 10^{-13}$  strain in a narrow band centered on 30 sec. Since this sample contains microseismic noise and residual barometric pressure induced noise, as well as instrument noise, the design goal has been met with an extra margin of capability. Figure 21 contains a spectral comparison between the S325L1 and S325L2 seismograms. The S325L1 and S325L2 spectra coincide from about 12 to 20 sec.

This observation is significant. It means:

1. The calibration constant is known to sufficient accuracy on the S325-1 strain seismometer;

TRACE	MAG.
GCT	<u>AT 25 SEC</u>
HR MIN	-
DAY	-
WV	-
FLAG	-
S325L2	1.36 X 10 <sup>-12</sup> STRAIN/MM
S325LL2	2.18 X 10 <sup>-11</sup> STRAIN/MM
S325L1	1.21 X 10 <sup>-12</sup> STRAIN/MM
S325LL1	1.19 X 10 <sup>-11</sup> STRAIN/MM
S55L	1.20 X 10 <sup>-12</sup> STRAIN/MM
S55LL	1.14 X 10 <sup>-11</sup> STRAIN/MM
PZL	26.4K
P325L	88.2K
P55L	82.9K
PZX	33.4K
P55X	109K
P325X	95.0K
ML1	0.057/UBAR/MM
•PZS	487K
•P325S	462K
ML2	3.5/UBAR/MM
WV	2 MPH/MM
WD	

-40-

NOTE: • MAG. AT 1 SEC

QC-AZ  
CAMERA 1  
RUN 151  
31 MAY 1970

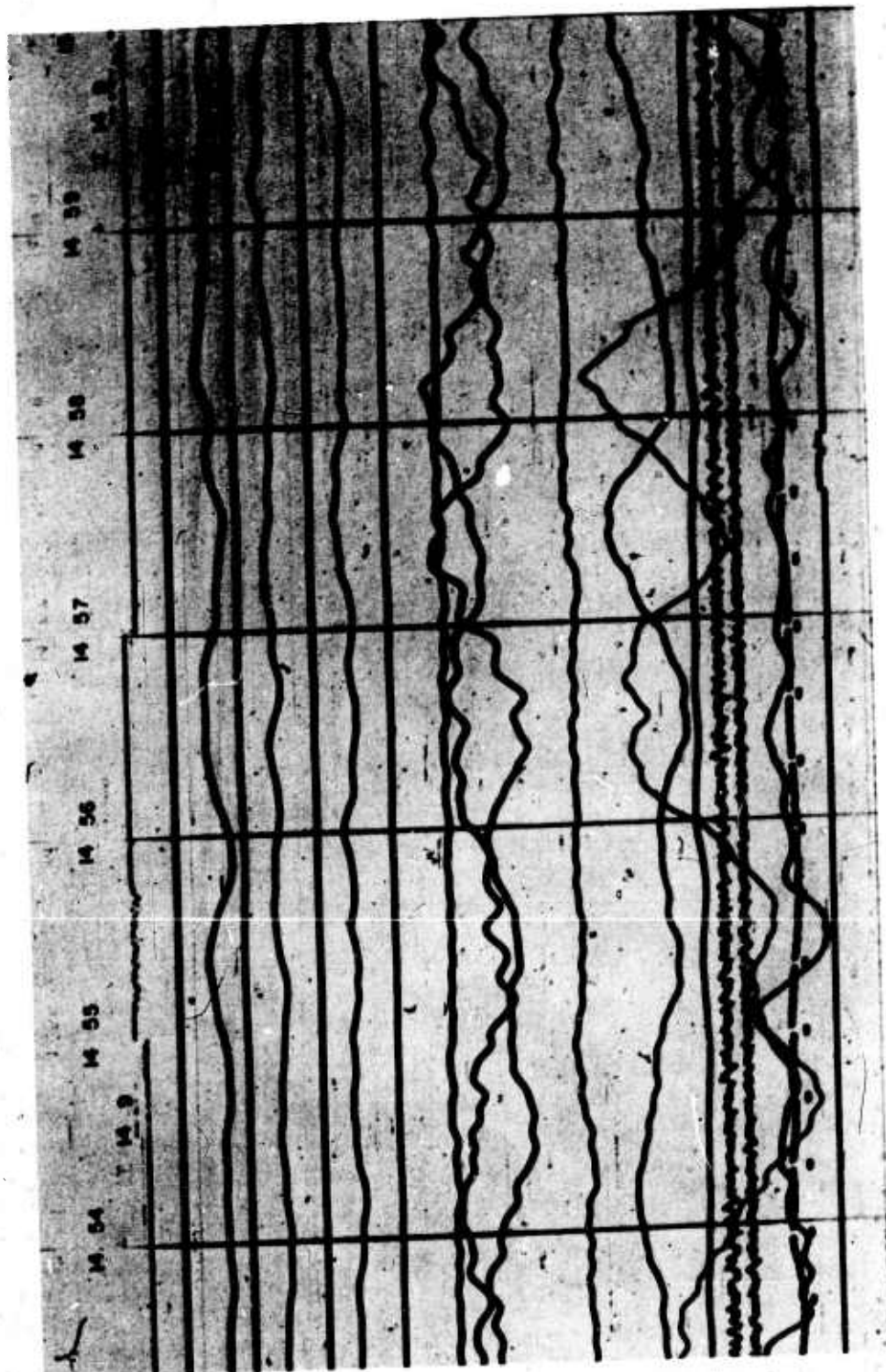
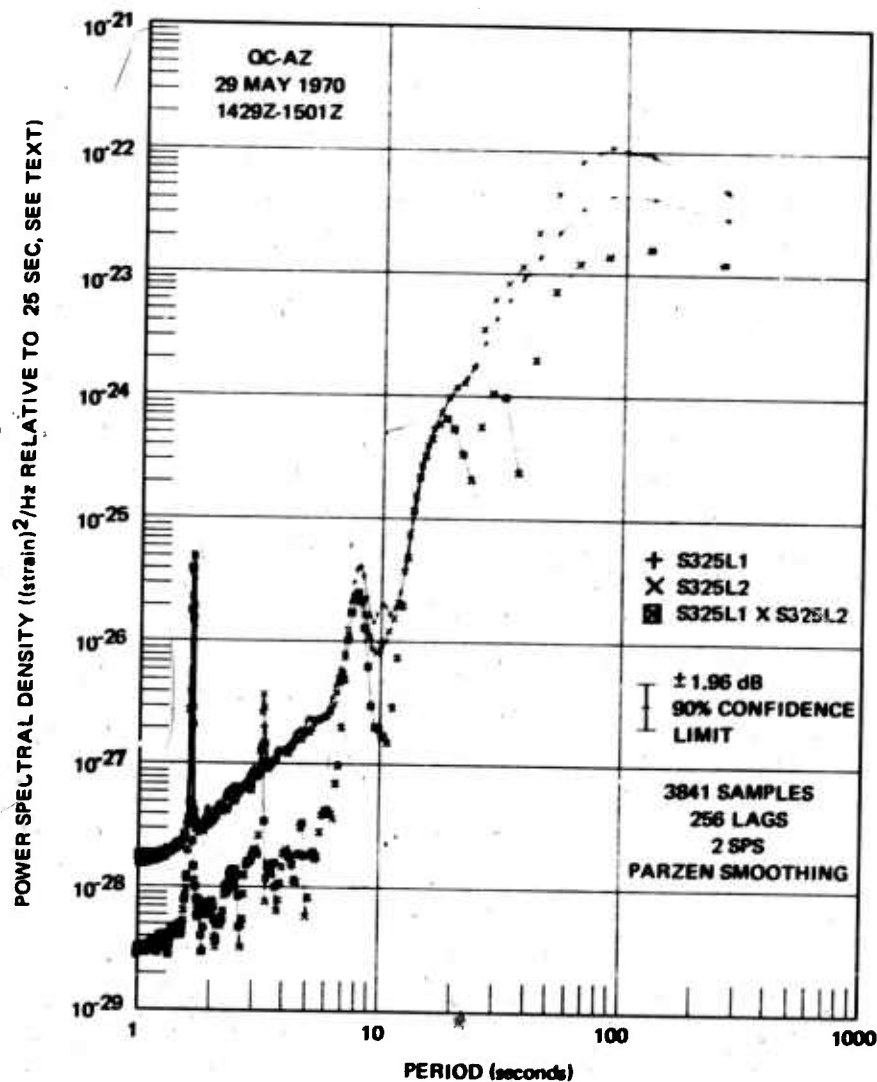
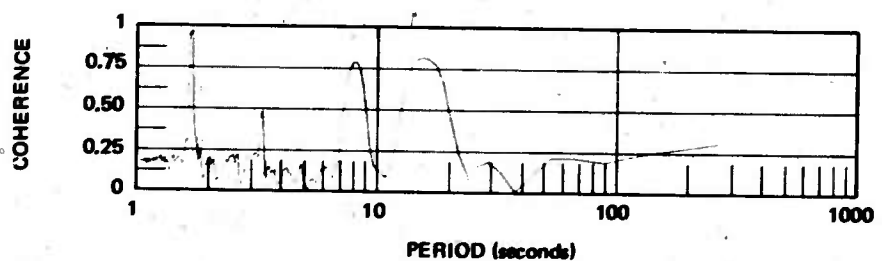


Figure 20. Reproduction of 16 mm film recording of a portion of the low wind sample

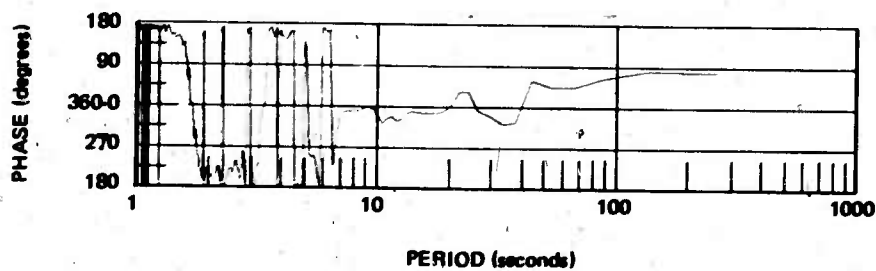




a. Power spectral density



b. Coherence



c. Phase lead  
S325L2 over S325L1

Figure 21. Power spectral density, coherence, and relative phase angle with 256 lags for parallel horizontal strain seismographs S325L1 and S325L2 during low wind conditions

G 6012

2. The calibration constant is known to sufficient accuracy on the S325-2 strain seismometer;

3. In the 12 to 20 sec period range both strain seismometers are seeing the same identical ground strain which must be a true representation of the ground motion.

Another observation to be made from these spectra is that the S325L2 has more power than the S325L1 at periods longer than about 25 sec and has less power at periods shorter than about 12 sec including the 8 sec microseismic peak. This same frequency dependent phenomena will be seen in the other comparisons that follow. The true mechanism acting here is not positively known. However, a working hypothesis is presented that

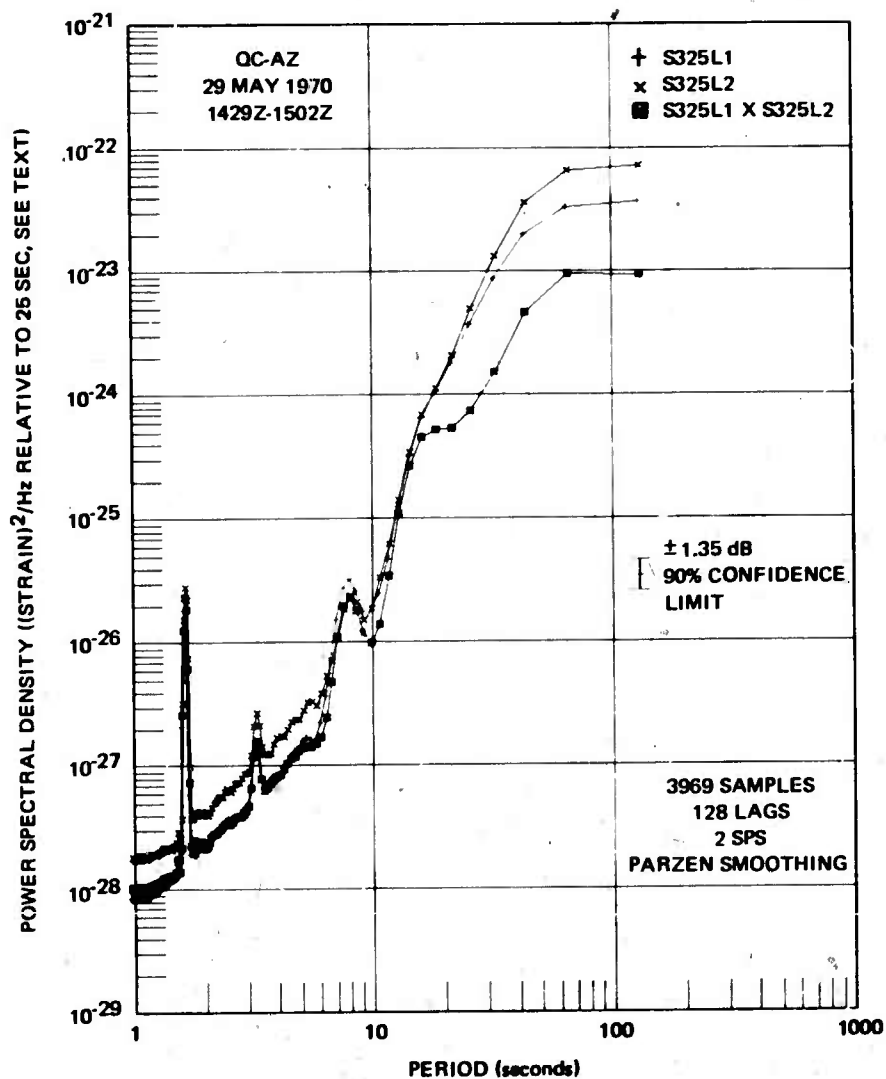
a. Both the S325-1 and S325-2 are attenuated to signals from travelling waves in the earth by a small factor (see section 11.4.4) either because of the joint and fault system in the rock in the vicinity of the mine or because of the geometry of Goldmine Mountain and the surrounding region and;

b. The S325L2 is acted on by an additional frequency dependent damping force proportional to the rate-of-change of ground strain. The S325-1 strain seismometer is mounted in solid rock both at the fixed end anchor and at the transducer, while the S325-2 strain seismometer is mounted on a different mineralized fault zone at both ends. The two faults both dip at about 70 deg. The fault at the northern end dips to the northeast and the fault at the southern end dips to the southeast.

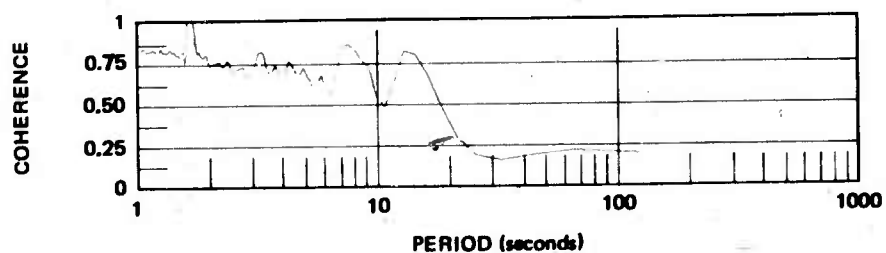
It is possible that the small attenuation factor may be different for both instruments. If it were the same, the two spectra in figure 20 would be equal at long periods and the S325L2 would have less power than the S325L1 at all periods. The attenuation factor could be the same, and the small difference at the longest periods in figure 20 could be a calibration uncertainty.

The coherence between the two parallel strain seismometers peaks at the microseismic periods of 8 sec and 18 sec. While the coherence of about 0.25 at 30 sec and from 50 to 256 sec is not statistically significant, it is felt that the coherence of a partially deterministic signal plus noise is a more robust process than indicated by statistical tests with random numbers and that this coherence is meaningful. The coherence is attributed to ground strains from the small to moderate microbarometric pressures. The phase angle lead of the S325L2 over the S325L1 is seen to be almost zero between 8 and 30 sec and 30 and 50 sec and almost 90 deg lead at 30 sec and between 50 and 256 sec. The 90 deg phase lead is in agreement with the above hypothesis that the S325L2 is acted upon by a damping force proportional to rate-of-change of strain.

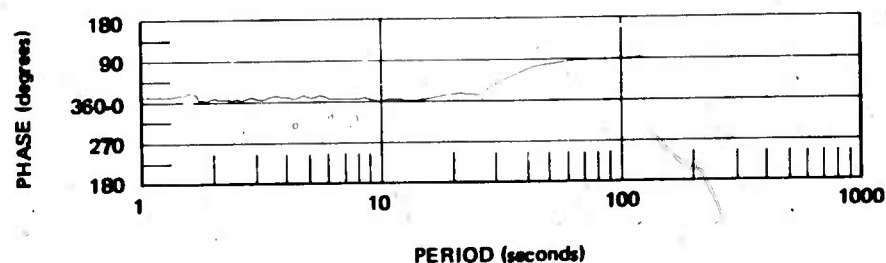
In studying the numerical values of the two power spectral densities small peaks not discernible in the plot in figure 21 were noticed at adjacent frequencies for the S325L1 and S325L2. If these peaks are real, the analysis plotted in figure 21 is a true representation. However, since the variations in the magnitudes of the smaller peaks are much less than the statistical stability of the analysis, they may not be real physical phenomena. To test the validity of their frequency separation, another analysis was performed with half as many lags (128 instead of 256) to obtain a smaller confidence limit. The results of this analysis are plotted in figure 22. These results are seen



a. Power spectral density



b. Coherence



c. Phase lead  
S325L2 over S325L1

Figure 22. Power spectral density, coherence, and relative phase angle with 128 lags for parallel horizontal strain seismographs S325L1 and S325L2 during low wind conditions

G 6013



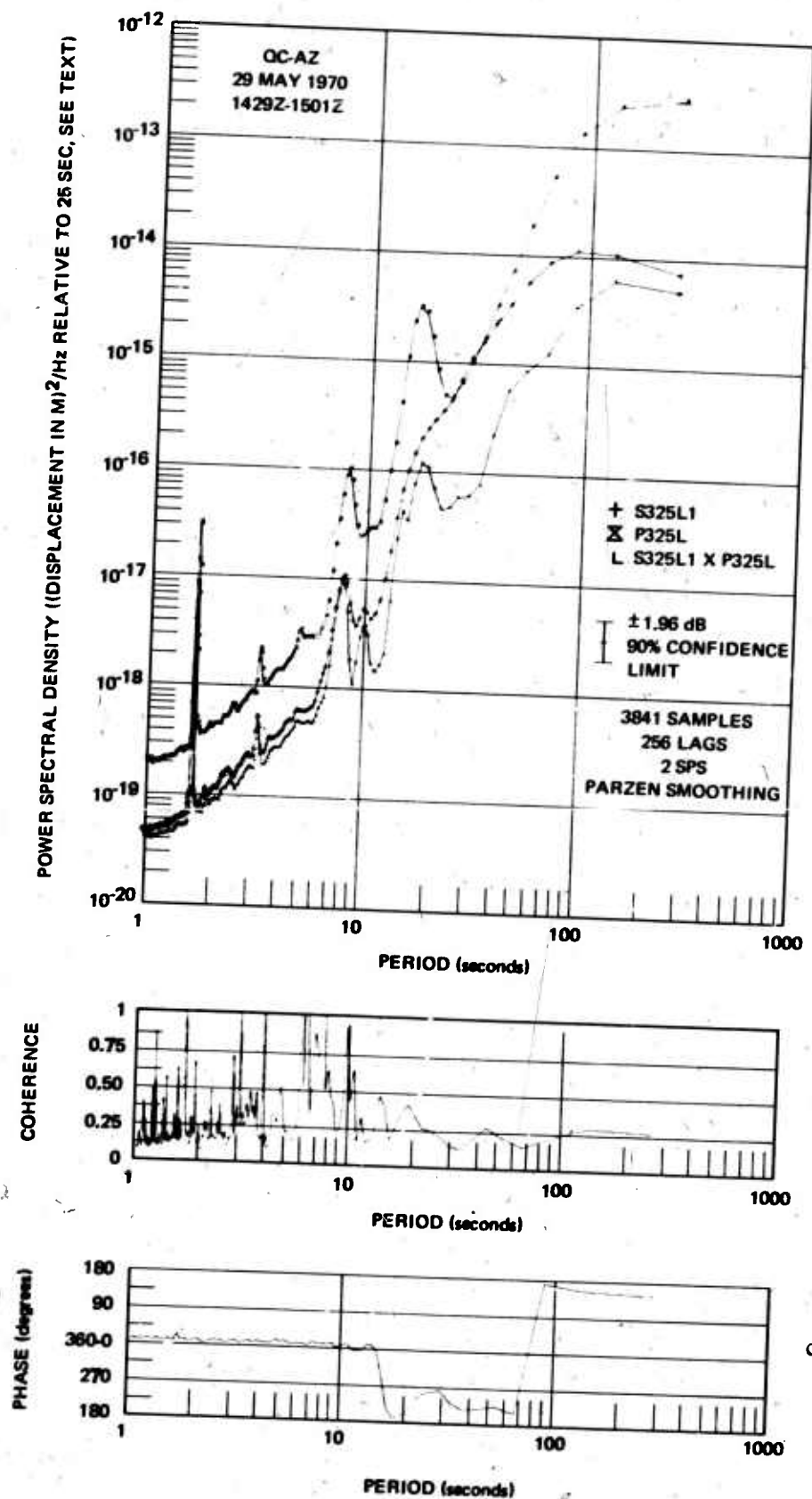
to be a smoothed version of figure 21 with these primary differences. The cross spectral peak at 30 sec in figure 21 is smoothed into the peak at 16 sec in figure 22. The smoothing improved the coherence at all periods in figure 22 over figure 21. The phase lead of S325L2 over S325L1 is almost zero from 1 sec to about 25 sec, then smoothly changes to a 90 deg phase lead. The conclusions arrived at from the analysis of figure 21 with greater frequency resolution are substantiated by the analysis of figure 22 with greater statistical stability.

The computational noise referred to in section 11.4.1 is seen to be on the order of  $10^{-27}$  strain<sup>2</sup>/Hz compared to maximum values on the order of  $10^{-22}$  strain<sup>2</sup>/Hz in both figures 21 and 22. A sharp break is seen in the slope of all of the spectra at about 6 sec. At periods shorter than 6 sec, the results should be considered invalid.

The S325L1 strain seismograph spectra are compared with the P325L inertial seismograph spectra in figure 23. The strain spectra and the strain-inertial cross spectra are normalized as described in section 11.4.1 with this normalization, the two sets of spectra of this sample are almost equal at 25 sec. As stated above, the inertial seismometer had been recently worked on and was experiencing long-period noise oscillations. Consequently, the P325L spectra at periods longer than about 40 sec should be used only for qualitative comparisons. Even with the extra long-period noise, the total mean square displacement (relative to 25 sec) in the passband of the seismograph was  $3.10 \times 10^{-15}$  m<sup>2</sup> which is 55.6  $\mu$ m rms in the horizontal direction of 325 deg azimuth. The three peaks in the cross spectra are significant. The two peaks at 8 sec and 16 sec are from microseisms and the 10 sec peak is from some unidentified signal. The significance of the 10 sec peak is its confirmation as a true signal even though it was not apparent in the spectra of the S325L2 seismograph in figure 21 or 22 and is almost smoothed out of the P325L spectra. The significance of the 8 sec and 16 sec peaks are that the strain and inertial seismographs do not differ at these periods by the normalization factor applicable for the calibration period of 25 sec. The fact that there is less energy on the S325L1 strain seismograph than the P325L inertial seismograph implies that:

- a. The apparent phase velocity of this energy in the horizontal plane in the 325 deg azimuth is larger at 8 sec and 16 sec than at 25 sec, or
- b. The strain in the 325 deg azimuth is not coupled to travelling waves in the Earth to the same degree that the output of a horizontal pendulum is coupled to the same waves, or
- c. The local geometry of Goldmine Mountain and the surrounding region has modified the component of the local vector wave number in the 325 deg azimuth, or
- d. A combination of these factors.

There are indications that all of these have contributed. Signals appear smaller than expected on the two parallel 325 deg azimuth seismographs as will be shown in section 11.4.4. There also is a definite difference in the apparent



a. Power spectral density

b. Coherence

c. Phase lead  
P325L over S325L1

Figure 23. Power spectral density, coherence, and relative phase angle with 256 lags for parallel horizontal seismographs, S325L1 strain and P325L inertial, during low wind conditions

G 6014

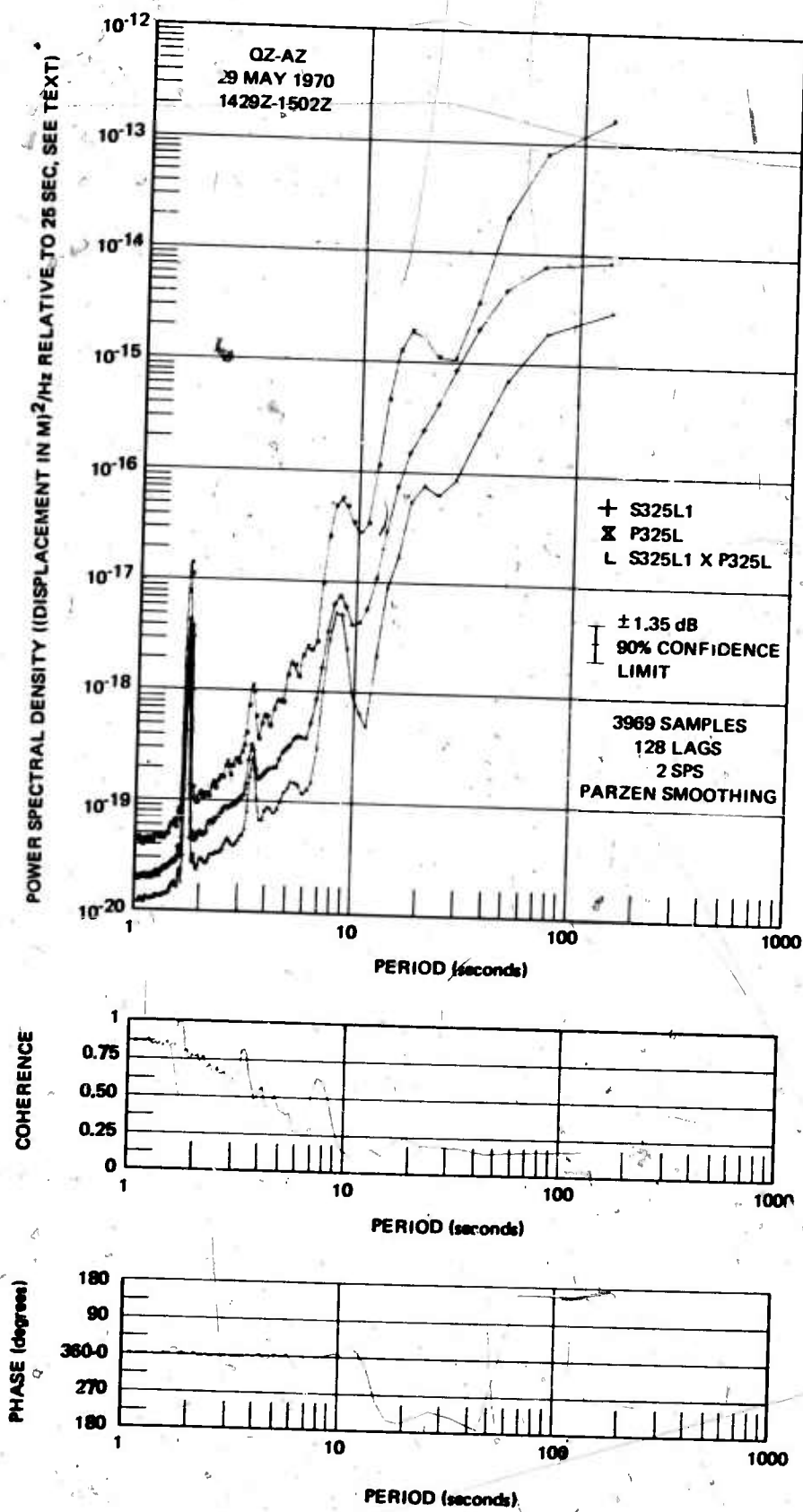
phase velocity of the energy at 8 sec and of the energy at 16 sec with relatively less 16 sec energy being seen in the spectra and in the film recordings.

The coherence between the P325L and S325L1 plotted in figure 23b suffered from computational noise resulting from the large scale difference between strain and pendulum data. Because of the noise, the data should be interpreted qualitatively as high coherence at 8 sec and fairly constant coherence at about 0.25 from 10 sec to 256 sec. The phase lead of P325L is seen to be zero for periods up to 10 sec and close to 180 deg for the longer periods. Figure 24 is an analysis of the same data used for figure 23 except that 128 lags were used for a smaller confidence limit. The results are the same as discussed above except that the 10 sec peak was smoothed into the adjacent passbands. The coherence and relative phase angles are the same.

The perpendicular strain seismograph S55L is compared to the S325L1 in figure 25. The total mean square strain (relative to 25 sec) on the S55L in the total passband was  $9.79 \times 10^{-25}$  strain<sup>2</sup> which is an rms strain of  $9.89 \times 10^{-13}$ . The two spectra are very similar at periods up to about 20 sec with peaks in the cross spectra at 8, 10, 18 and 32 sec. The first three peaks are from coherent energy. The 8 sec and 18 sec peaks and most periods have a 180 deg phase relationship. The 180 deg phase relationship is characteristic of transverse shear strain. At the 10 sec peak, S55L leads S325L1 by 300 deg and at 32 sec by 240 deg. Since the phase angle is not 180 deg, the 10 and 32 sec peaks probably are not the result of shear strains. The occurrence of the 30-32 sec peak in the cross spectra of both the parallel strain seismographs and the perpendicular strain seismographs indicates that there was real ground motion at this period. This may be another frequency of low-level microseismic activity. The level of the power spectra in both azimuths is relatively the same with the differences well within the range of possible variation in the azimuthal response of the strain systems to the sources of microseismic noise.

#### 11.4.3 High Wind Conditions

During episodes of high wind, there are variations in the pressure field which create displacements, tilts, and strains within the ground. These disturbances are discussed in more detail in sections 11.5 and 11.6. The two parallel horizontal strain seismographs S325L1 and S325L2 respond identically to these ground strains. Figure 26 is a portion of the time sample that was analyzed for a comparison during windy conditions. The wind was blowing about 20 mph and gusting to 35 mph. The ML2 microbarograph outside the mine was responding to large pressure fluctuations. In the figure the equal and opposite strain typical of a shear stress is visible at several points, with an especially large yet typical pulse at about 0503Z. The S325L1 and S325L2 seismographs track each other identically in the time domain in figure 26 and the spectra almost overlay in the frequency domain in figure 27. During this sample the total mean square strain (referenced to 25 sec) in the passband was  $4.198 \times 10^{-23}$  strain<sup>2</sup> for the S325L1 and  $5.458 \times 10^{-23}$  strain<sup>2</sup> for the S325L2 and the rms values were  $6.479 \times 10^{-12}$  strain and  $7.388 \times 10^{-12}$  strain, respectively. In figure 27 the spectra are seen to be almost identical except for a slight increase in value for the S325L2 at increasing period. The coherence is one and there is no relative phase shift between the seismographs. The seismographs are recording identically. The time sample was extended to 6.7 hr and analyzed for the comparison for periods between 20 and 2560 sec seen in



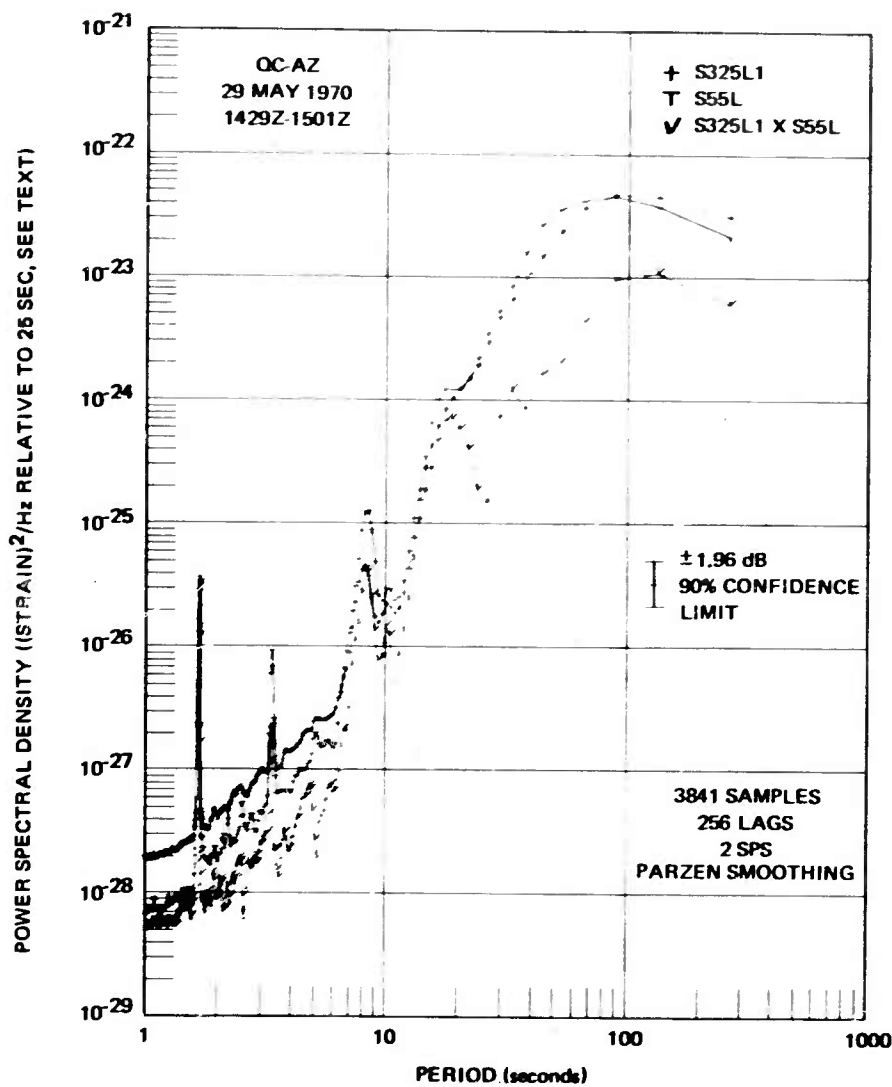
a. Power spectral density

b. Coherence

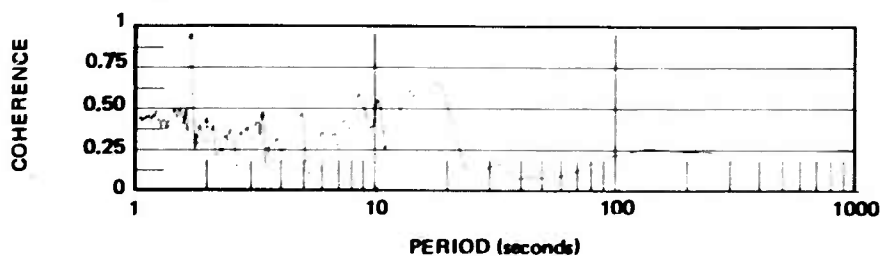
c. Phase lead  
P325L over S325L1

Figure 24. Power spectral density, coherence, and relative phase angle with 128 lags for parallel horizontal seismographs, S325L1 strain and P325L inertial, during low wind conditions

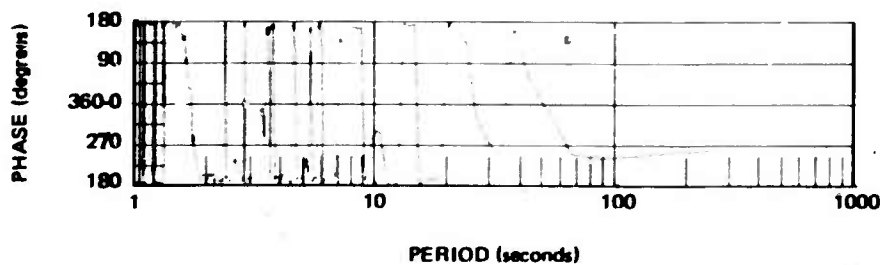
G 6015



a. Power spectral density



b. Coherence



c. Phase lead  
S55L over S325L1

Figure 25. Power spectral density, coherence, and relative phase angle with 256 lags for perpendicular horizontal strain seismographs S325L1 and S55L during low wind conditions

G 6016

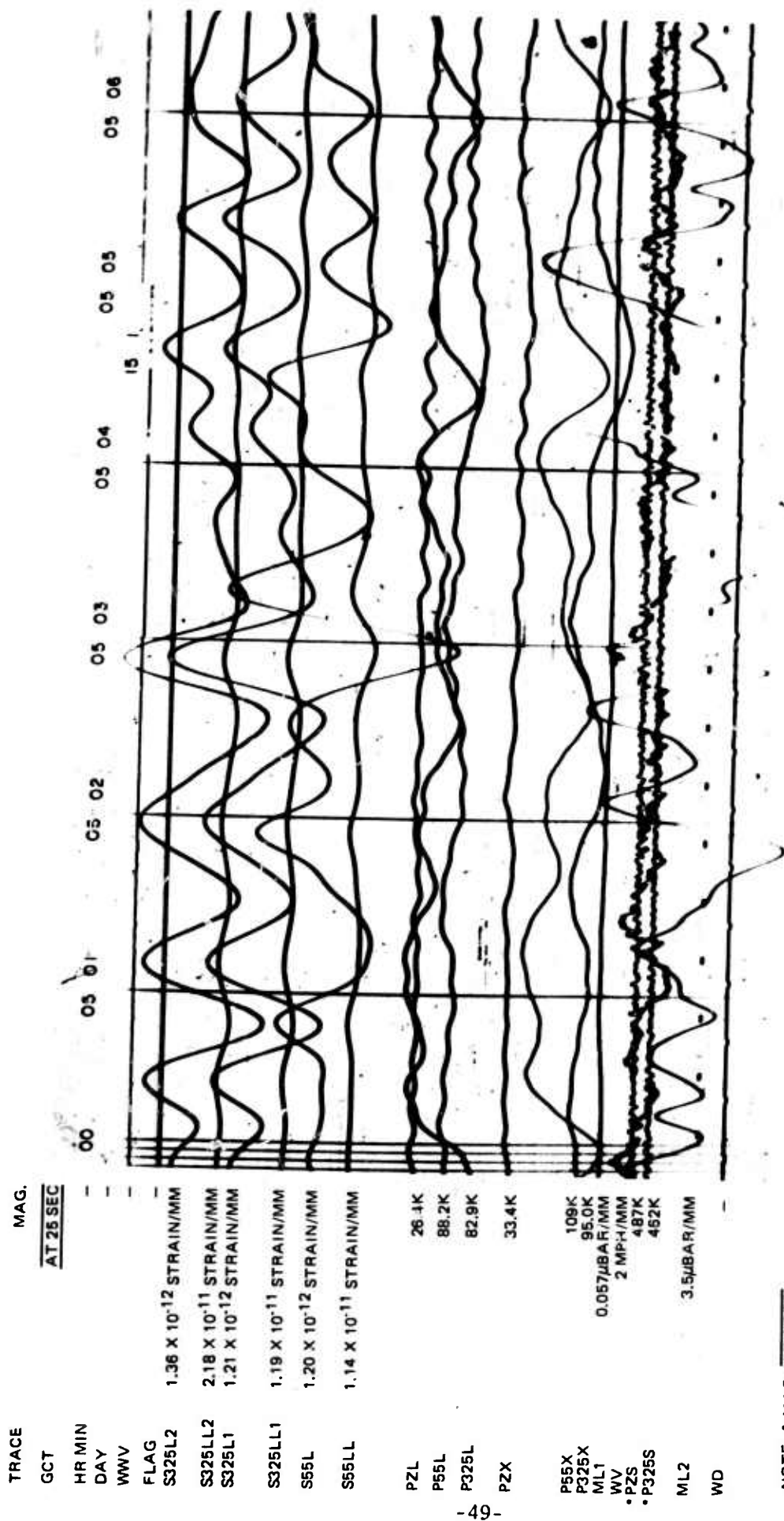
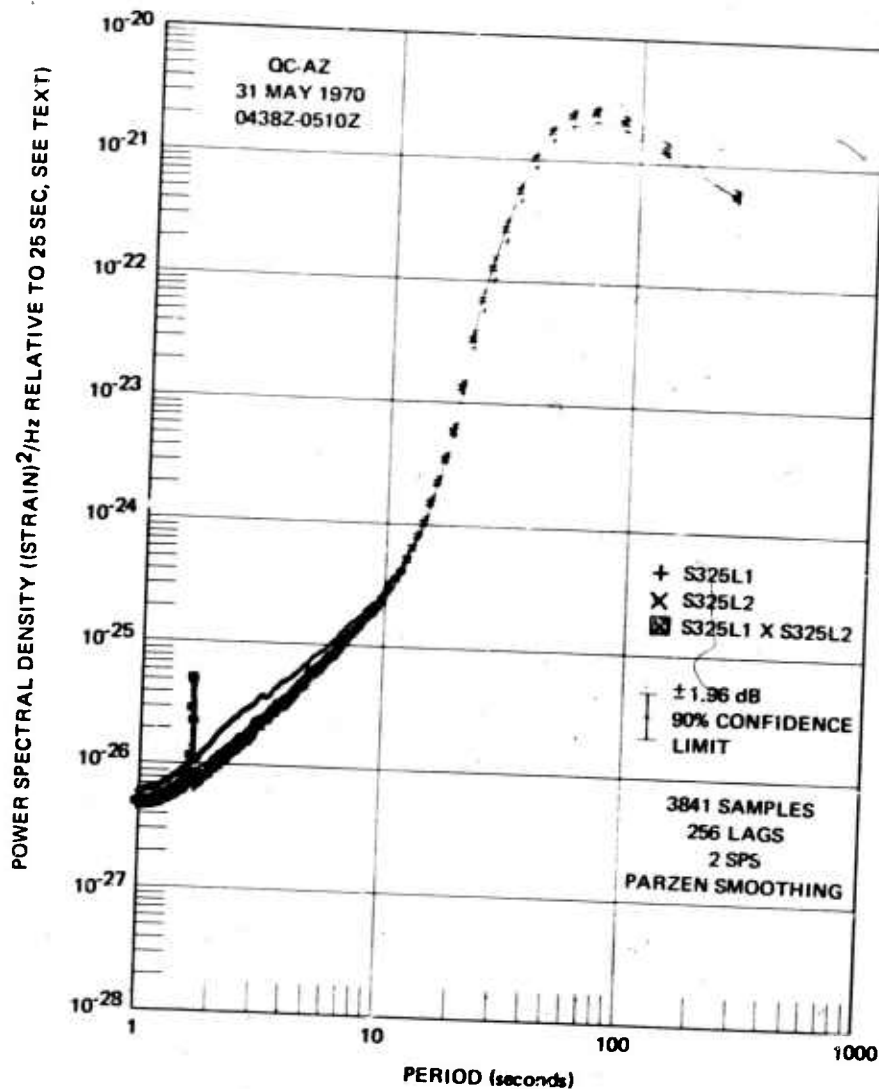
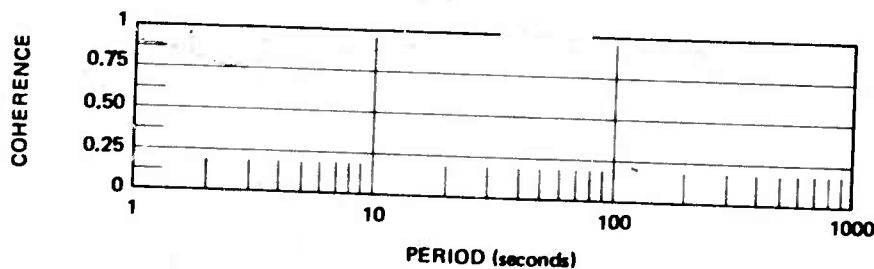


Figure 26. Reproduction of 16 mm film recording of a portion of the high wind sample

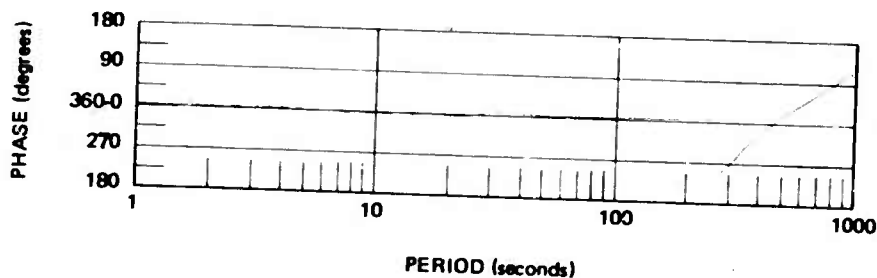
QC-AZ  
CAMERA 1  
RUN 151  
31 MAY 1970



a. Power spectral density



b. Coherence



c. Phase lead  
S325L2 over S325L1

Figure 27. Power spectral density, coherence, and relative phase angle of parallel horizontal strain seismographs S325L1 and S325L2 during high wind conditions, 1 to 256 sec range

G 6017

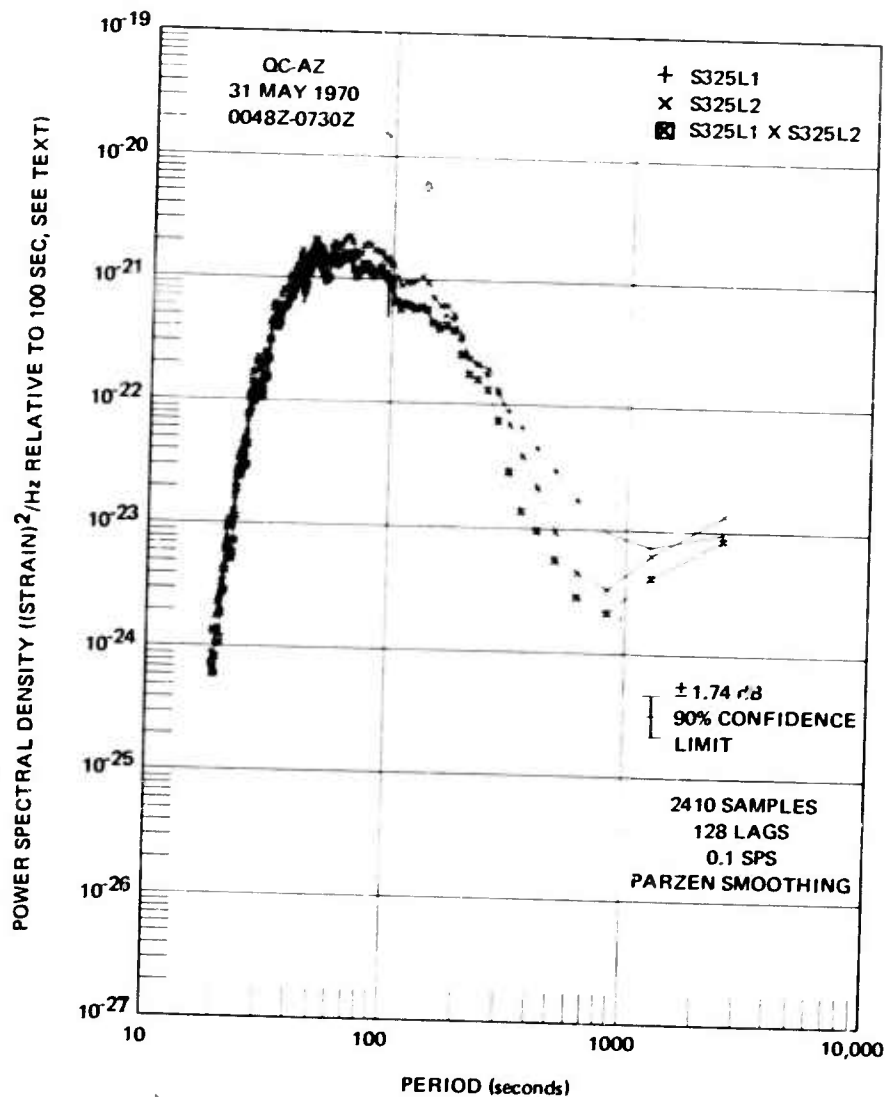


figure 28. The results are the same as at the shorter periods except between 300 and 1280 sec where the S325L1 has more power than the S325L2. The coherence is almost one except in the anomalous period range and the relative phase angle remains at essentially zero for all periods. A comparison between the ULP response seismographs S325U1 and S325U2 is illustrated in figure 29. The rms strains (referred to 25 sec) during the 6.7 hr period in the total passband of these seismographs were  $3.61 \times 10^{-11}$  strain and  $2.08 \times 10^{-11}$  strain, respectively. The two are seen to be essentially the same at periods out to 234 sec and then the S325U1 exhibits considerably more power than the S325U2.

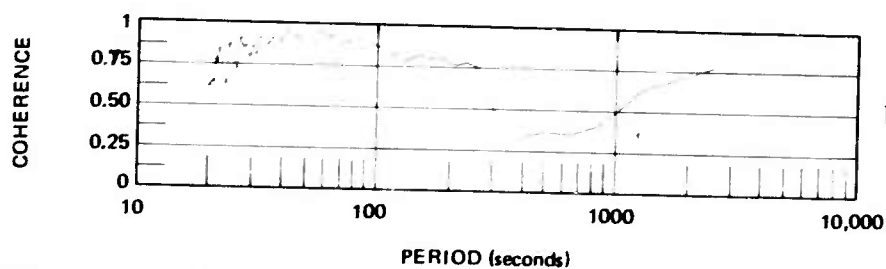
During the pressure induced disturbances, the horizontal inertial seismometers are subjected to considerable tilting as can be seen in the seismogram in figure 26 on the inertial ALPS response channels (P-L). The tilts are more evident on the inertial extended-long-period response (P-X) which has a higher magnification at the longer periods than the ALPS response. The inertial P325L is compared with the strain S325L1 in figure 30. The rms ground displacement (referred to 25 sec) during this 32.0 min sample was 33.0  $\mu$ . This value is lower than the rms displacement during the low wind sample because in the intervening 37 hr the seismometer settled down to almost normal operation. In the P325L spectra in figure 30, the general background spectrum has risen until the microseismic peaks at 8.4 and 16.2 sec are almost swamped by the general rise in the spectrum. The coherence is relatively low indicating that the tilt response of the horizontal inertial seismometer is only partially linearly related to the ground strain. The ground strain has increased so that the entire spectra is above the strain of the microseismic peaks which are not visible either in the analog trace or as a spectral peak.

The perpendicular horizontal strain seismographs are very comparable in spectra. The equal amplitude and 180 deg phase relationship is indicative of the response of perpendicular linear strainmeters to transverse shear strain. During the high wind sample analyzed, the rms strain (referenced to 25 sec) for the S55L seismograph was  $6.500 \times 10^{-12}$  strain. This rms value is within 0.32 percent of the  $6.479 \times 10^{-12}$  rms strain on the S325L1. The fact that the rms values are this close is fortuitous considering the errors in calibration and analysis, but it does substantiate that calibrations are very close and are well within acceptable operational tolerances. The spectral comparison is plotted in figure 31. The spectra at periods shorter than about 10 sec are in the computational noise and are not meaningful. The spectra are seen to be very smooth and devoid of any peaks. The cross spectra does show a minor peak at the microseismic period of 16 sec. This small amount of microseismic strain apparently mixes with the pressure induced strain in a nonlinear manner resulting in the dip in the spectra at 20 sec. The coherence holds to reasonable values except for a minimum at 20 sec and at periods longer than 100 sec. The phase angle is almost 180 deg at all periods. Figure 32 extends the comparison to longer periods with the ULP response seismographs S325U1 and S55U. About the same picture is seen as before. The spectra are similar in appearance out to periods near 250 sec. A comparison of figures 29 and 32 shows that at the longer periods, the S55U resembles the S325U2 more than the S325U1. The cross spectra have many sharp high Q peaks. With the frequency resolution and statistical stability of the analysis, these peaks are considered as being real and are definitely not an artifact of the data analysis. Also, since these peaks appear in the cross spectra of the perpendicular strains, but not in the cross spectra of the parallel strains, they must be associated with a shear strain phenomena.

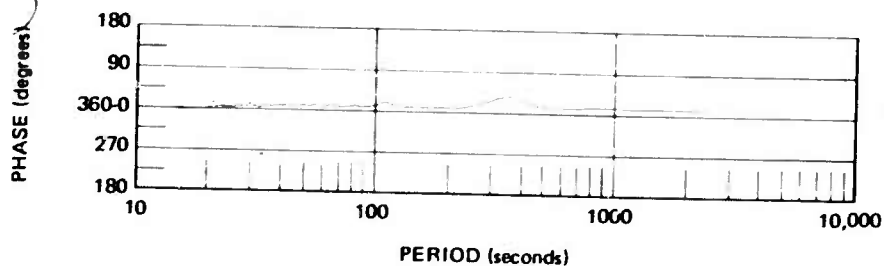




a. Power spectral density



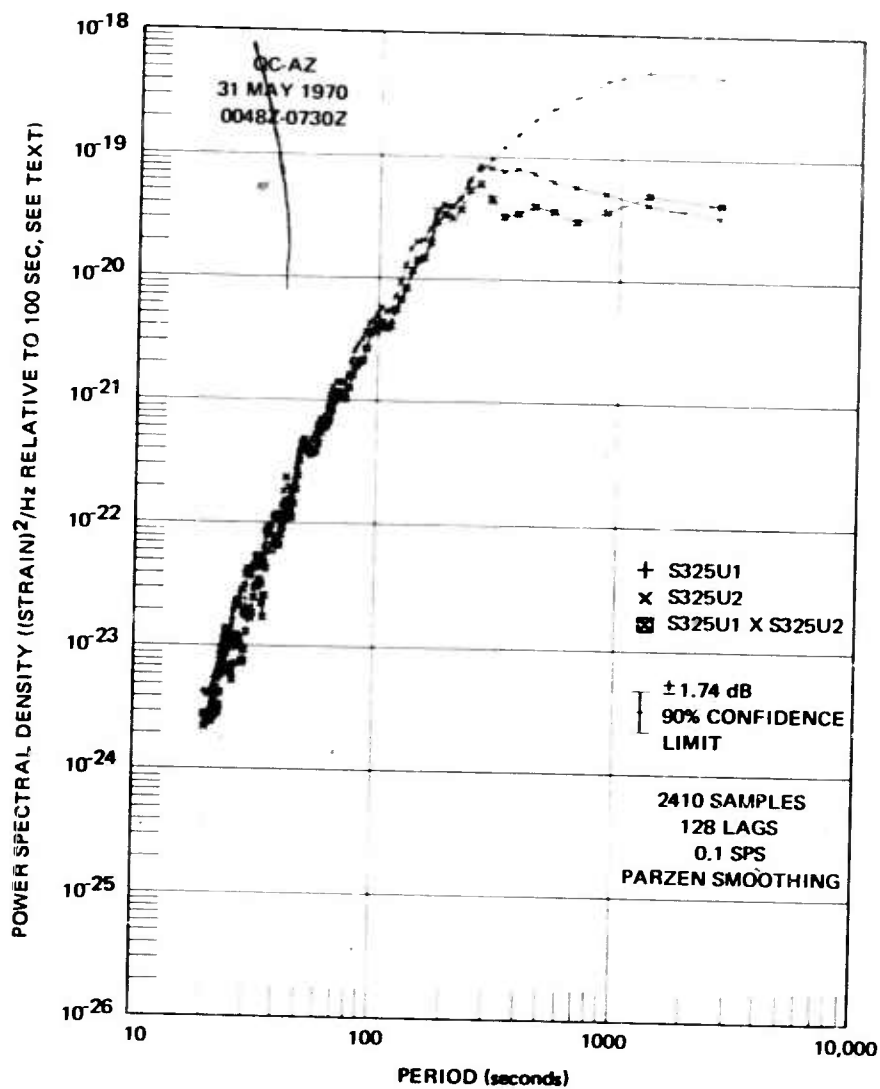
b. Coherence



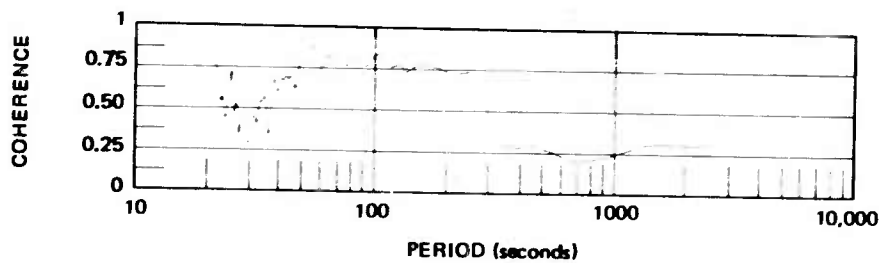
c. Phase lead  
S325L2 over S325L1

Figure 28. Power spectral density, coherence, and relative phase angle of parallel horizontal strain seismographs S325L1 and S325L2 during high wind conditions, 20 to 2560 sec range

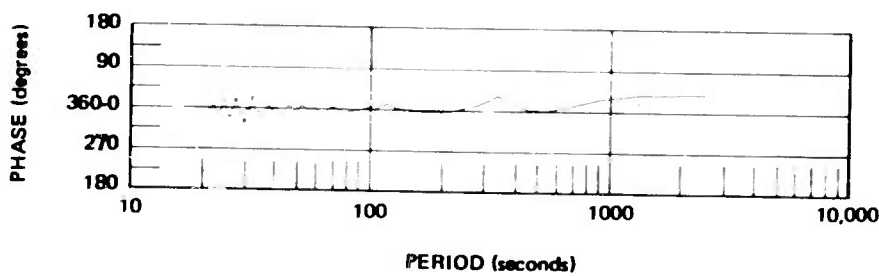
G 6018



a. Power spectral density



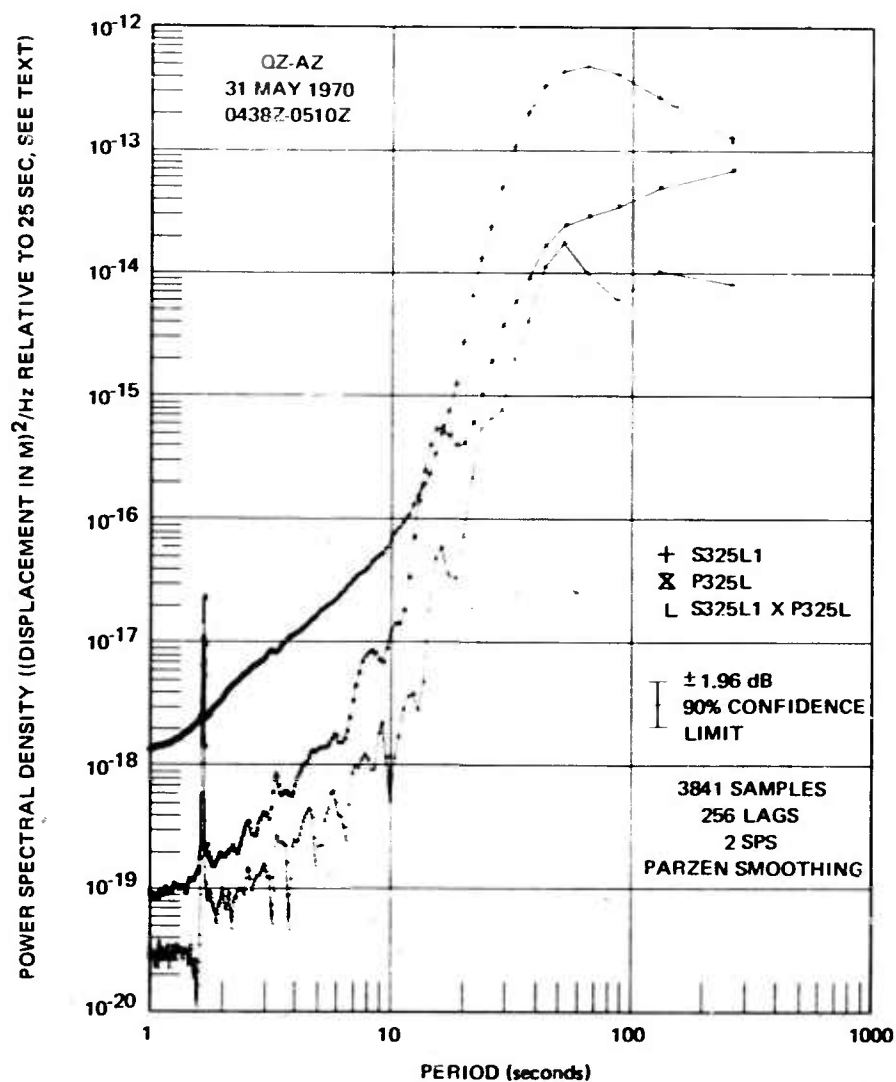
b. Coherence



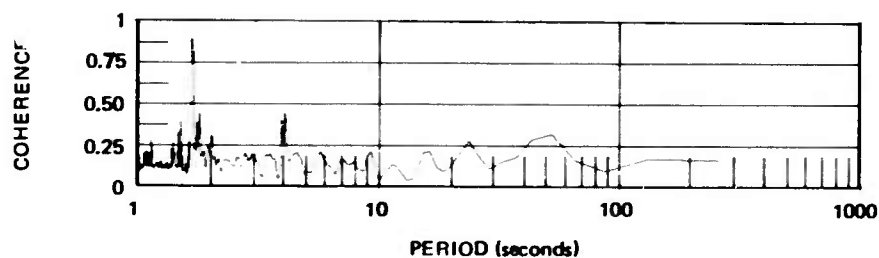
c. Phase lead  
S325U2 over S325U1

Figure 29. Power spectral density, coherence, and relative phase angle of parallel horizontal strain seismographs S325U1 and S325U2 during high wind conditions

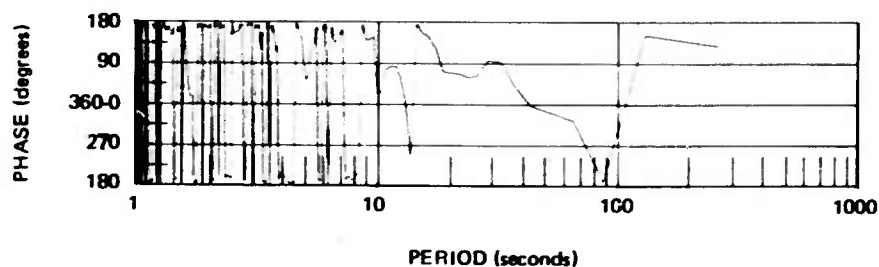
G 6019



a. Power spectral density



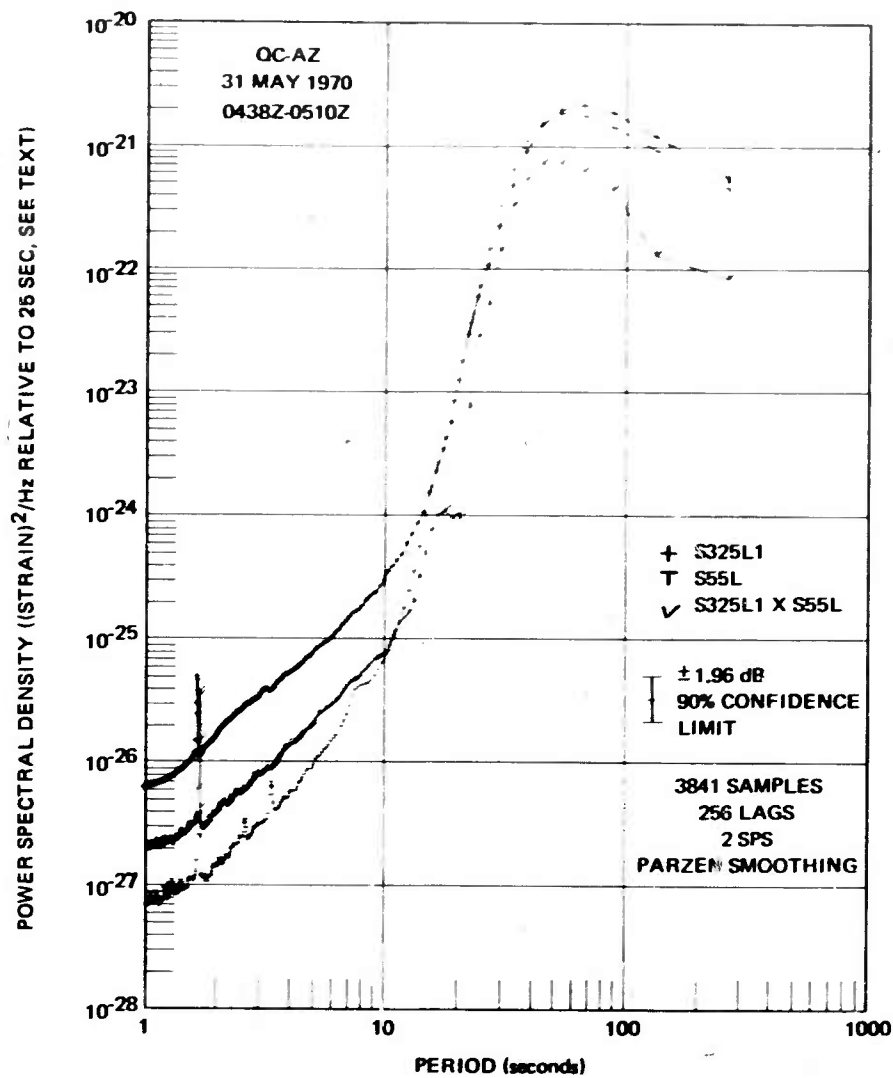
b. Coherence



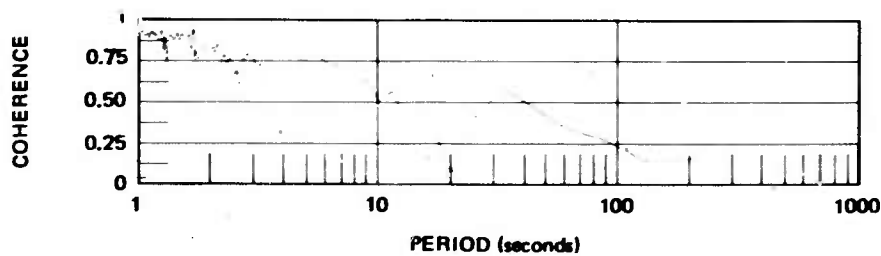
c. Phase lead  
P325L over S325L1

Figure 30. Power spectral density, coherence, and relative phase angle of parallel horizontal seismographs, S325L1 strain and P325L inertial, during high wind conditions

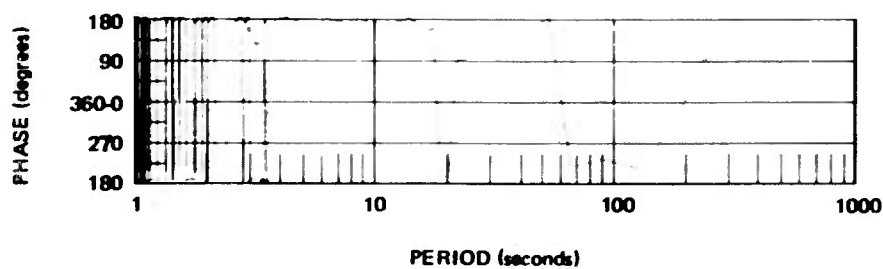
G 6020



a. Power spectral density



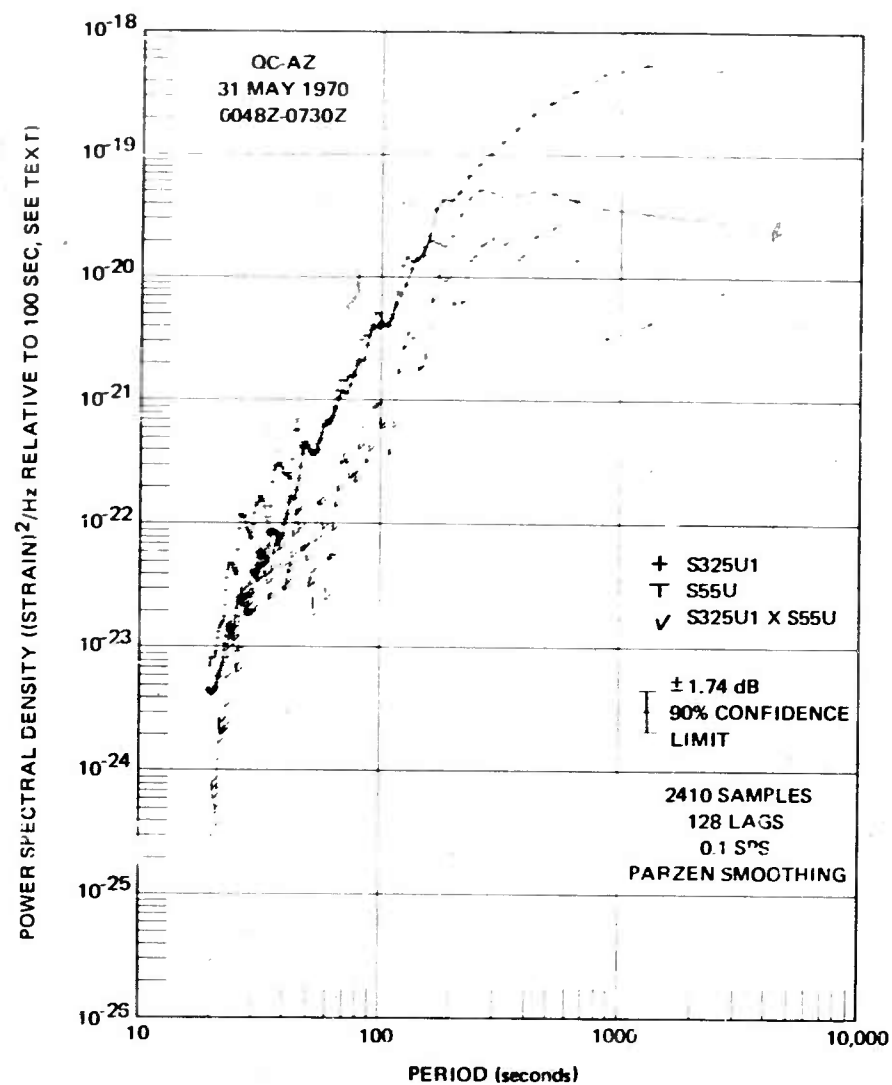
b. Coherence



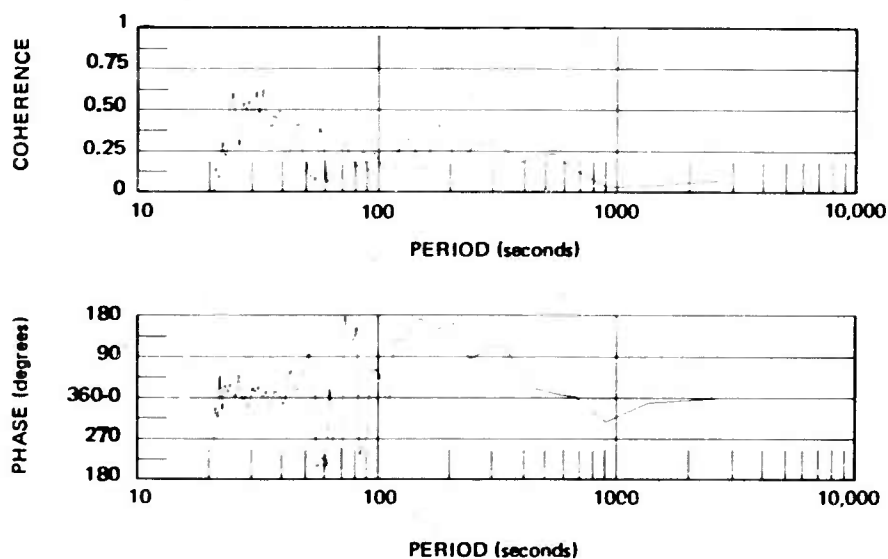
c. Phase lead  
S55L over S325L1

Figure 31. Power spectral density, coherence, and relative phase angle of perpendicular horizontal strain seismographs S325L1 and S55L during high wind conditions

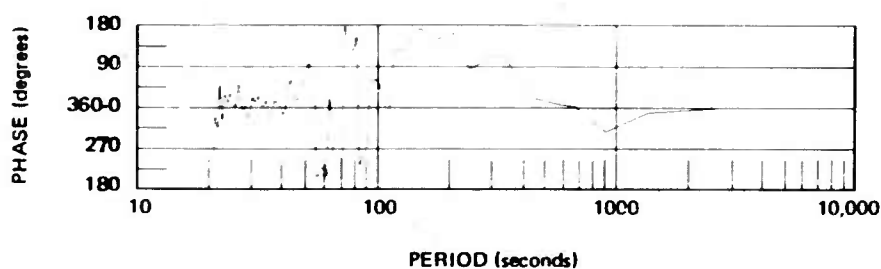
G 6021



a. Power spectral density



b. Coherence



c. Phase lead  
S55U over S325U1

Figure 32. Power spectral density, coherence, and relative phase angle of perpendicular horizontal strain seismographs S325U1 and S55U during high wind conditions

G 6022

The coherence between the perpendicular strain seismographs shows the coherence of the peaks in the cross spectra at between about 0.25 and 0.4. The relative phase angle tends toward 180 deg at periods between 50 and 210 sec and tends toward 0 deg at other periods.

#### 11.4.4 Earthquake Signals

Three earthquake signals were used to verify that the parallel horizontal strain seismographs produced the same outputs for travelling waves. All three signals are associated with the large Peru earthquake of 31 May 1970. The USC&GS PDE card data on this earthquake are:  $0 = 2023:27.3$ ,  $9.2S$ ,  $78.8W$ ,  $h = 43$  km, near coast of northern Peru,  $m_b = 6.6$ ,  $M_s = 7.8$ ,  $\Delta = 52.5$  deg, azimuth station-to-epicenter  $137.4$  deg. The first signal sample used from this earthquake was from the coda of the LR1 Rayleigh wave during a time window equivalent to group velocities of 1.72 to 1.10 km/sec. The second signal sample is a combined signal from the LR2 Rayleigh wave with a group velocity window of 2.52 to 2.20 km/sec and from the LQ3 Love wave and the LR3 Rayleigh wave with a group velocity window of 3.37 to 2.95 km/sec. During both of these time samples all of high gain channels were driven off the film and were clipping the magnetic tape recorders. Therefore, the low gain strain seismograph channels were used for the comparisons. The third earthquake signal is a major portion of the LR1 Rayleigh wave from an aftershock. The time window corresponds to group velocities between 3.37 and 2.95 km/sec. The USC&GS PDE card data for the aftershock are:  $0 = 0136:10.2$ ,  $9.3S$ ,  $79.0W$ ,  $h = 49$  km, off the coast of northern Peru,  $m_b = 6.0$ ,  $M_s = 5.5$ ,  $\Delta = 5.2$  deg, azimuth station-to-epicenter =  $138$  deg. The high gain seismographs were used for the analysis of the third sample even though the S325L1 and S325L2 were clipped on the peaks between 0203Z and 0206Z and the P325L was clipped on the peaks from 0203Z to 0207Z. The total time of clipping was about 5 percent of the whole time window and did not materially affect the analysis except at the short-period end of the spectrum.

The spectra for the first sample are plotted in figure 33. This sample was taken at the earliest window that could be selected after the low gain tape channels stopped clipping. Thus this sample represents the maximum signal that can be recorded without distortion on the ALPS response channels which are recorded at two signal levels. The spectra are seen to be almost identical with either a little less power on the S325LL1 at 7 sec and at periods longer than 20 sec or a slight calibration error. The coherence is one and the relative phase angle is zero at all periods. During this sample the rms strain (referred to 25 sec) in the whole passband was  $1.71 \times 10^{-10}$  strain on the S325LL1 and  $1.91 \times 10^{-10}$  strain on the S325LL2.

The two parallel strain seismographs are seen to track each other identically during the portion of the second sample shown in figure 34. The spectra, figure 35, show the same results for the S325LL1 and S325LL2. Again the S325LL1 either has slightly less power or a small calibration error. The coherence is one at all periods except 10 sec which is in the noise and the relative phase angle is zero. The spectra of the tape recorder-reproducer noise is evident as the approximately white noise between 3 and 10 sec. The analog antialias filter acting upon the tape noise is clear between 1 and 3 sec. The same antialias filter was used in digitizing all the data for which spectra were calculated in the 1 to 256 sec passband. The action of the filter

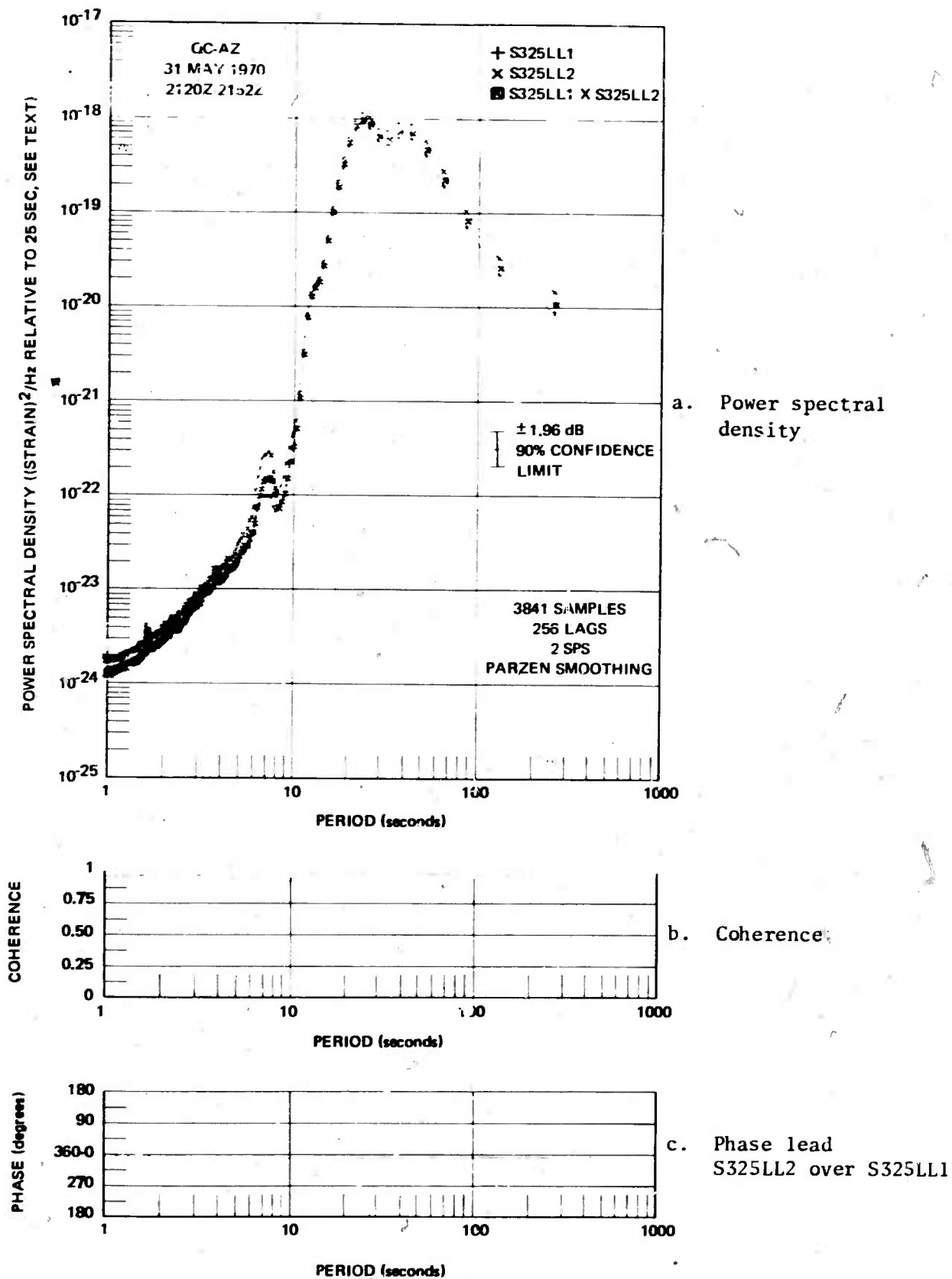


Figure 33. Power spectral density, coherence, and relative phase angle of parallel strain seismographs S325LL1 and S325LL2 during the LR1 Rayleigh wave coda of the Peru earthquake

G 6023

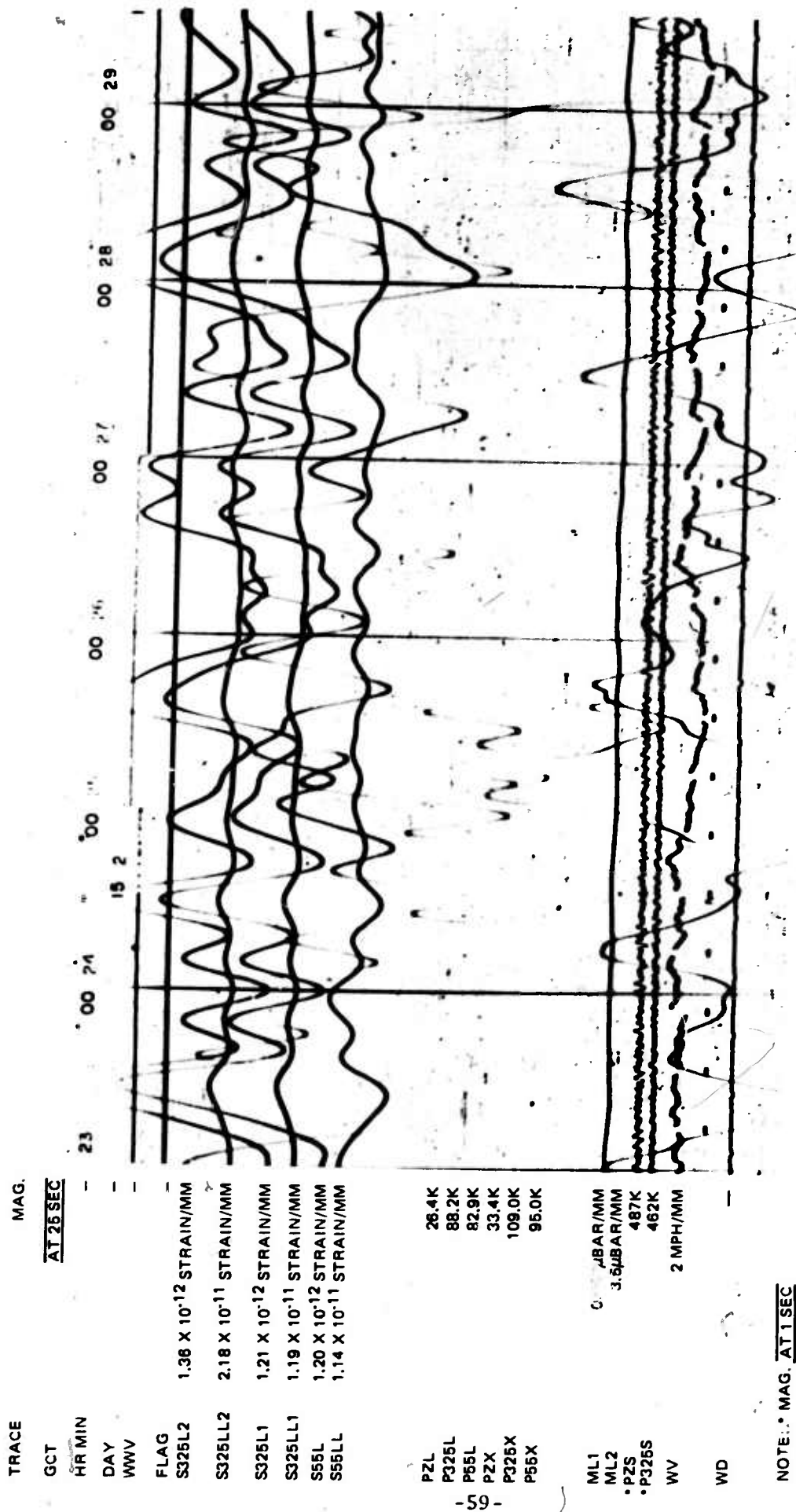
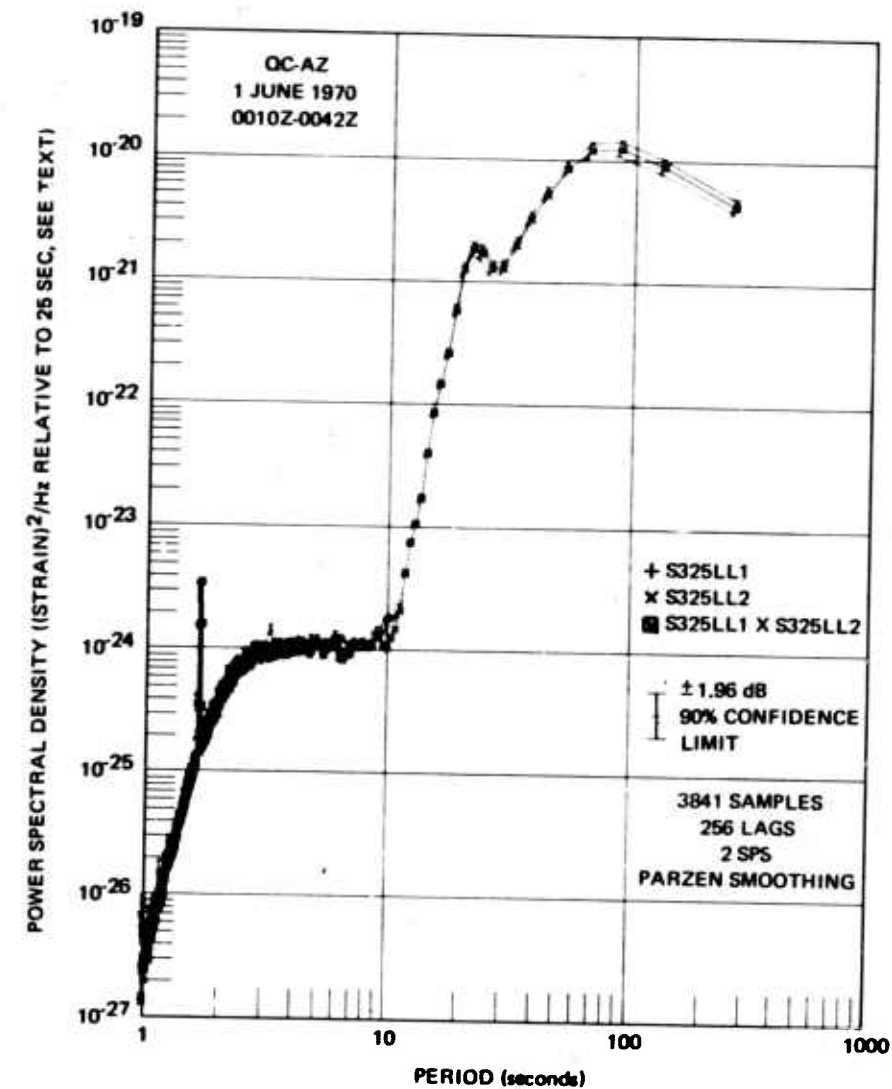


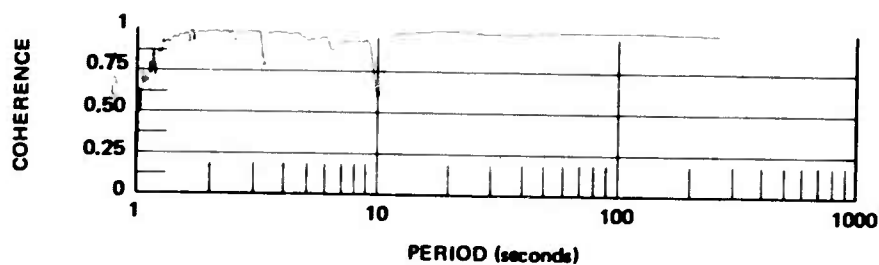
Figure 34. Reproduction of 16 mm film recording of part of the LQ3 Love wave, the LR2, and the LR3 Rayleigh wave from the Peru earthquake. USC&GS epicenter data:  $\Delta = 2023; 27.3, 9.2S, 78.8W$ ,  $h = 43$  km, near coast of northern Peru,  $m_b = 6.6$ ,  $M_s = 7.8$ ,  $\Delta = 52.5$  deg, azimuth = 137.5 deg

QC-AZ  
CAMERA 1  
RUN 152  
1 JUNE 1970

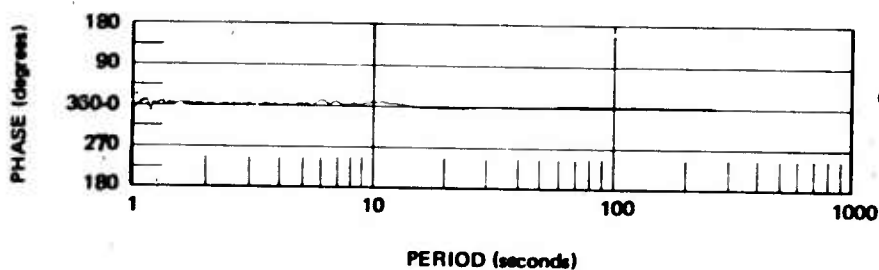




a. Power spectral density



b. Coherence



c. Phase lead  
S325LL2 over S325LL1

Figure 35. Power spectral density, coherence, and relative phase angle of parallel horizontal strain seismographs S325LL1 and S325LL2 during the LQ3 Love wave and the LR2 and the LR3 Rayleigh waves of the Peru earthquake

G 6024

is not seen in any of the other figures because the spectra between 1 and 3 sec in all the other figures is well below the computational noise level. The peak of the spectra at about  $10^{-18}$  strain<sup>2</sup>/Hz in figure 33 and the tape noise at about  $10^{-24}$  strain<sup>2</sup>/Hz in figure 35 indicate a potential 60 dB dynamic range with narrow band-pass spectral analysis. The same dB value applies to both power and amplitude.

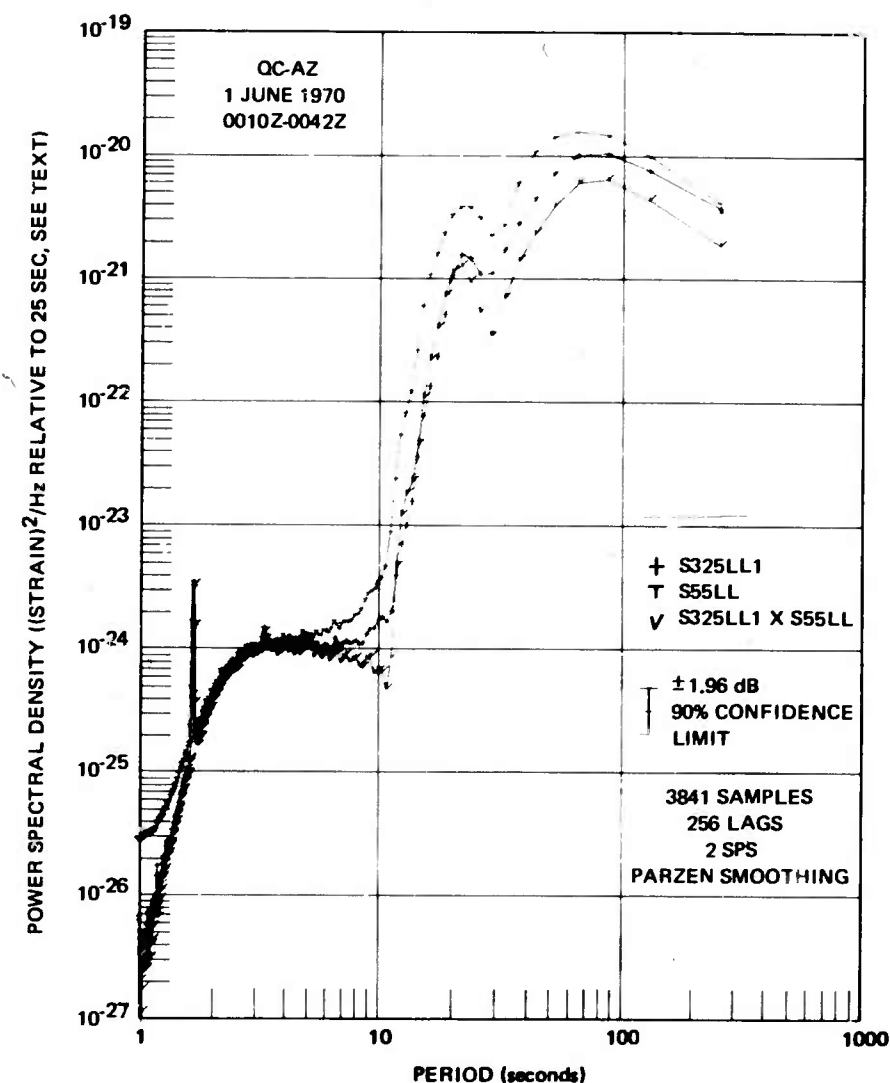
The strain spectra from the perpendicular S325LL1 and S55LL are plotted in figure 36. The spectra are similarly shaped but the S325LL1 has only about two-thirds the magnitude of the power on the S55LL. This difference is attributed to a possible cancellation of LR2 and LR3 Rayleigh motion on the almost radial 325 deg azimuth instruments. The coherence is good and the relative phase angle is 180 deg. The rms strain (referred to 25 sec) in the whole passband for this sample was: S325LL1  $1.500 \times 10^{-11}$  strain, S325LL2  $1.704 \times 10^{-11}$  strain, and S55LL  $1.983 \times 10^{-11}$  strain.

The third earthquake signal further confirms that the two parallel strain seismographs give the same output. The analog signals on the low gain channels are seen to track identically in figure 37. The spectra essentially overlay in figure 38. The data below 7 sec are into the noise. The peaks at the shorter periods are the result of using clipped data for about 5 percent of the sample. The coherence is one and the relative phase angle is zero at all periods. Because of the clipped data the spectra were also calculated with 128 lags for better stability. The results plotted in figure 39 are the same as in figure 38 except that the noise only affects periods shorter than 4 sec. The coherence is one at all periods indicating a more reliable statistical estimate.

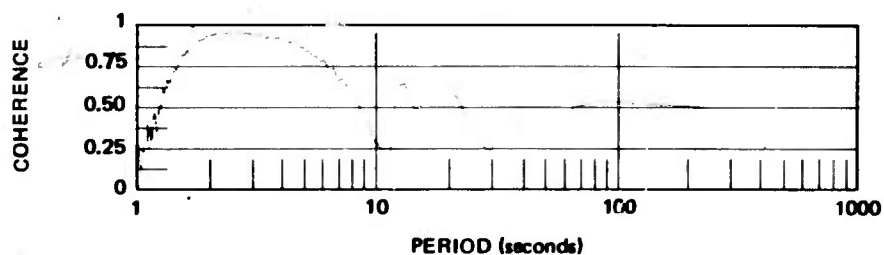
Figure 40 contains the spectra of the S325L1 and the P325L seismographs. There are two significant differences. First, at 25 sec, the S325L1 is a factor of 3.5 lower in (equivalent) power or 1.9 lower in amplitude than the P325L. Second, the cross spectra very closely follows the S325L1 in shape and power. There are two interpretations that can be taken from these data. First, the similarity of the strain spectra and the cross spectra suggest that the strain seismograph S325L1 represents the linear portion of true ground motion and the additional power on the inertial seismograph P325L represents a nonlinear output generated by localized tilting of the nearby rock. The concept of nonlinear tilt response of the rock is discussed in section 11.6.

The second interpretation is that the 325 deg azimuth component of the vector wave number in the vicinity of the instruments has been altered from the expected wave number component. Therefore, a better comparison could be made by empirically adjusting the strain seismograph output by the 3.5 power ratio. Even when this adjustment is made, the inertial seismograph has a significantly greater power than the strain seismograph at periods longer than 25 sec.

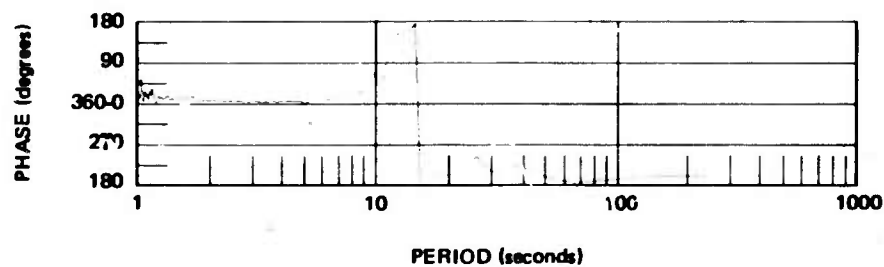
A nonlinear response to tilting could smooth out the spectral peaks on the inertial seismogram also. This lowering of the Q could result from a mechanical friction between blocks along the local fault and joint pattern. This same phenomena may be causing the frequency dependent relationship between the two parallel strain seismographs. The 9 sec peak in figure 40 is not as high a Q on the P325L as it is on the S325L1.



a. Power spectral density



b. Coherence



c. Phase lead  
S55LL over S325LL1

Figure 36. Power spectral density, coherence, and relative phase angle of perpendicular horizontal strain seismographs S325LL1 and S55LL during the LQ3 Love wave and the LR2 and the LR3 Rayleigh waves of the Peru earthquake

G 6025

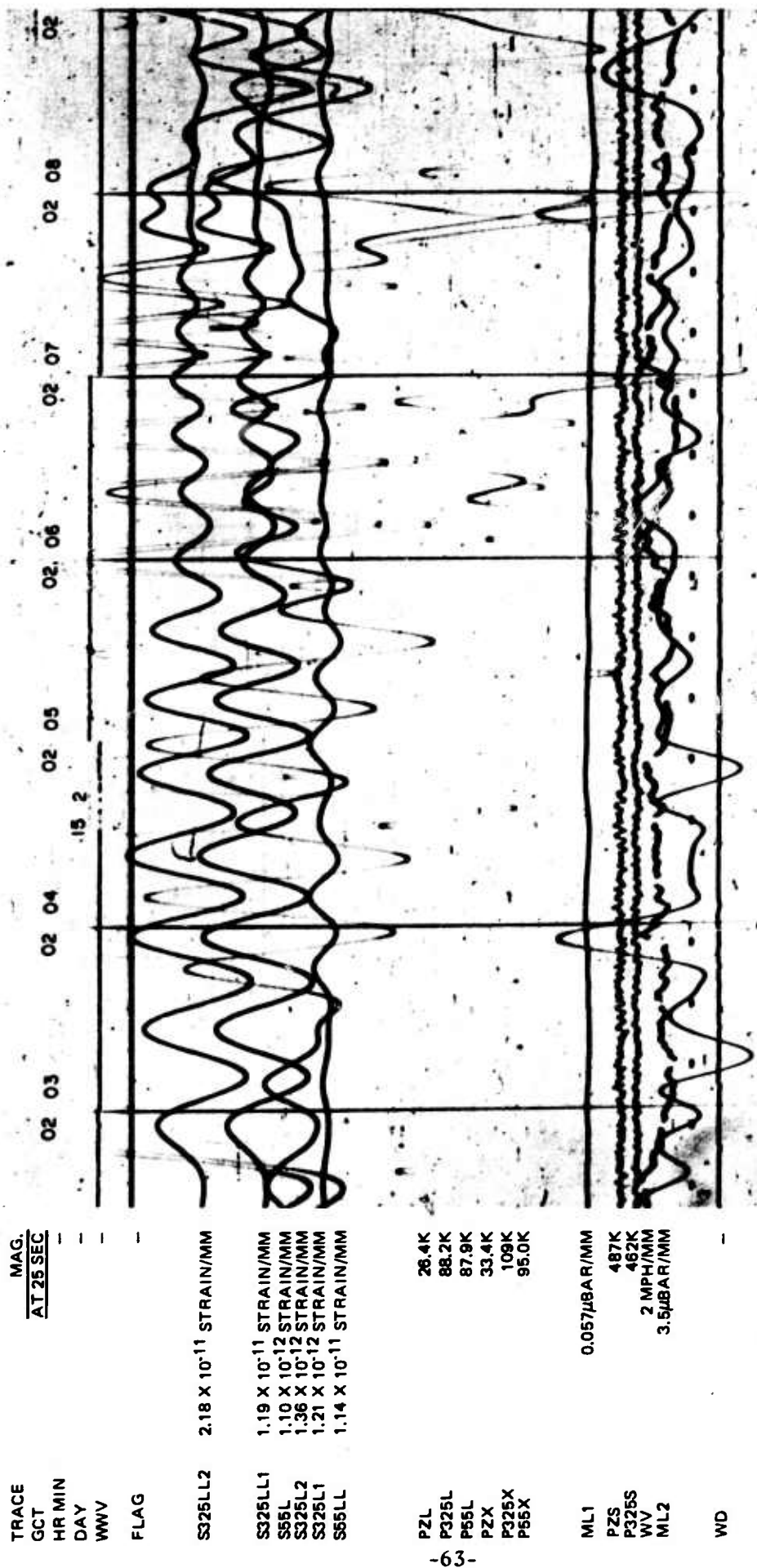
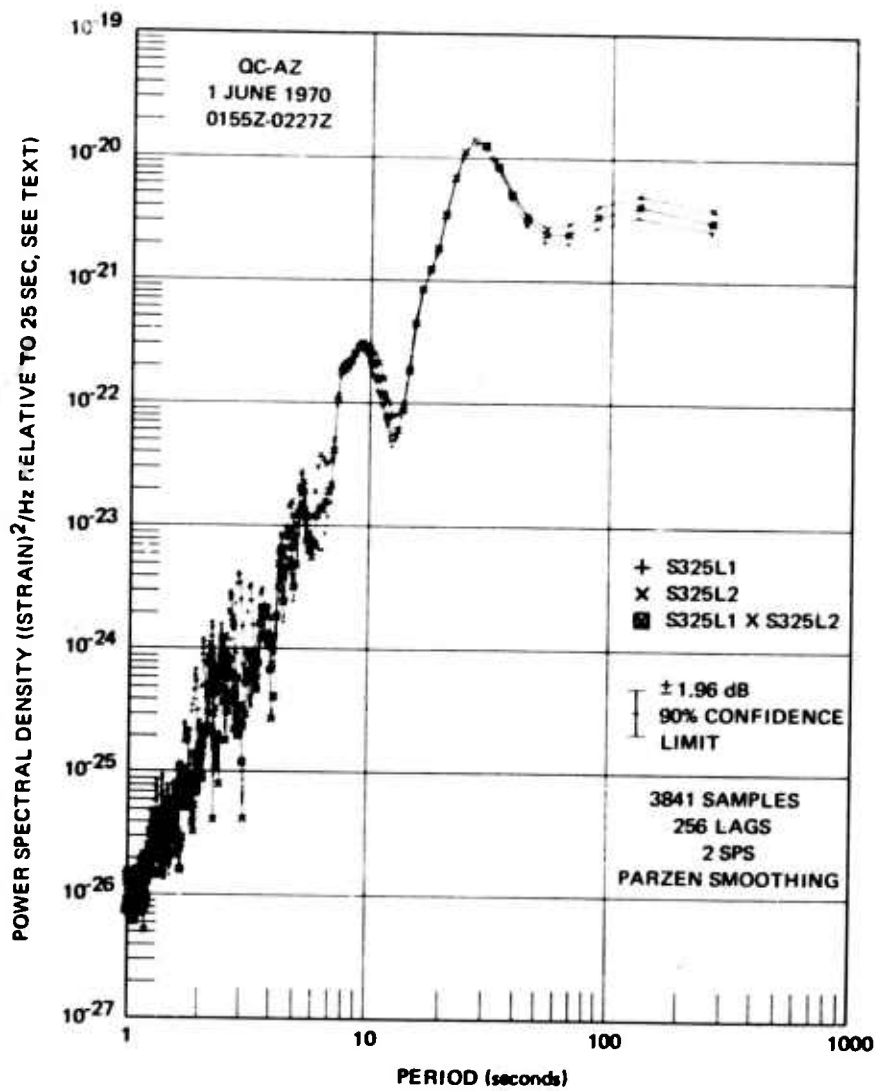


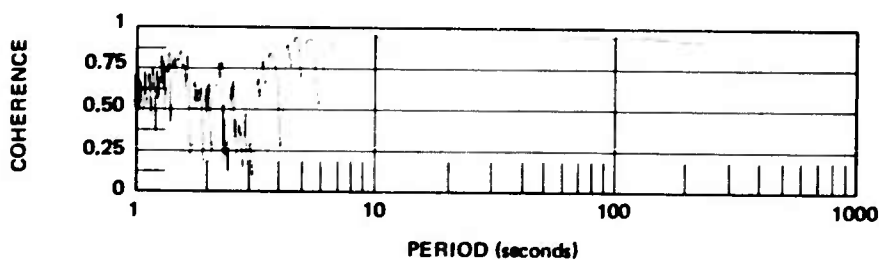
Figure 37. Reproduction of 16 mm film recording of LRI Rayleigh wave from an aftershock of the Peru earthquake. USC&GS epicenter data:  $\Delta = 0136:10.2$ ,  $9.3S$ ,  $79.0W$ ,  $h = 48$ , off coast northern Peru,  $m_b = 5.5$ ,  $M_s = 5.5$ ,  $\Delta = 52.5$  deg, azimuth =  $137.5$  deg

NOTE: \* MAG. AT 1 SEC

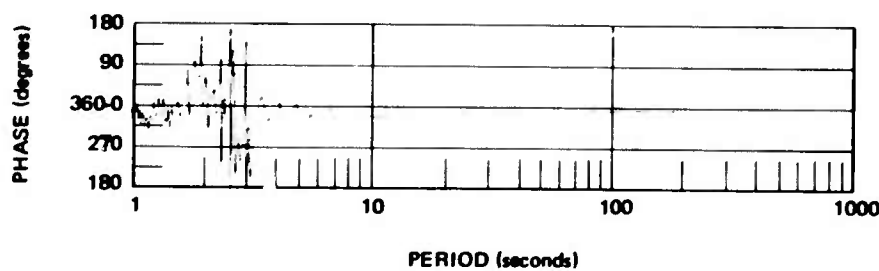
OC-AZ  
CAMERA 1  
RUN 152  
1 JUNE 1970



a. Power spectral density



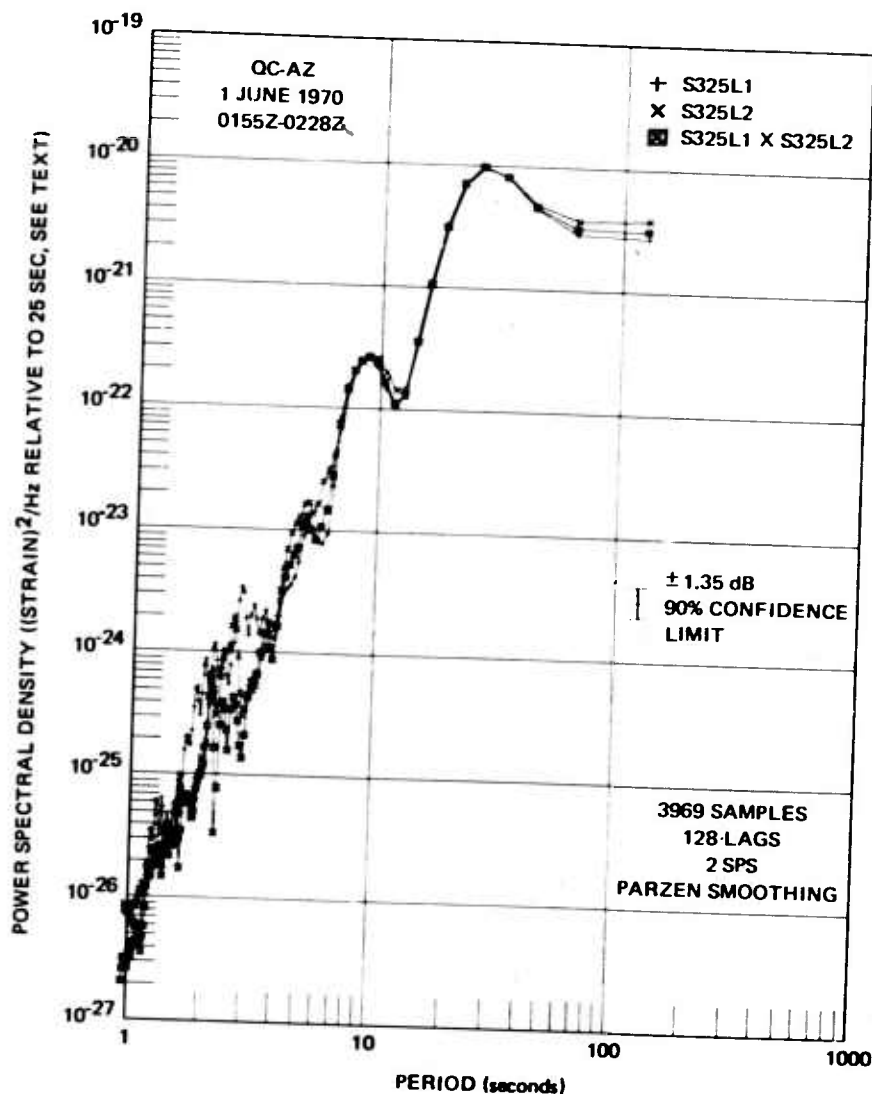
b. Coherence



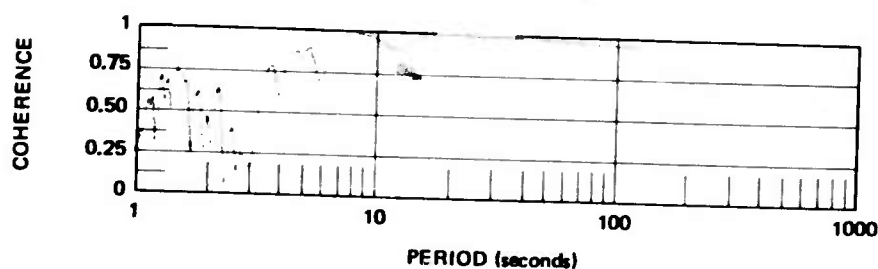
c. Phase lead  
S325L2 over S325L1

Figure 38. Power spectral density coherence, and relative phase angle with 256 lags for parallel horizontal strain seismographs S325L1 and S325L2 during the LR1 Rayleigh wave of an aftershock of the Peru earthquake

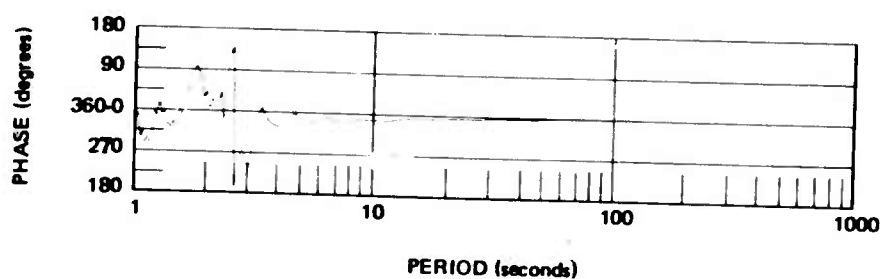
G 6026



a. Power spectral density



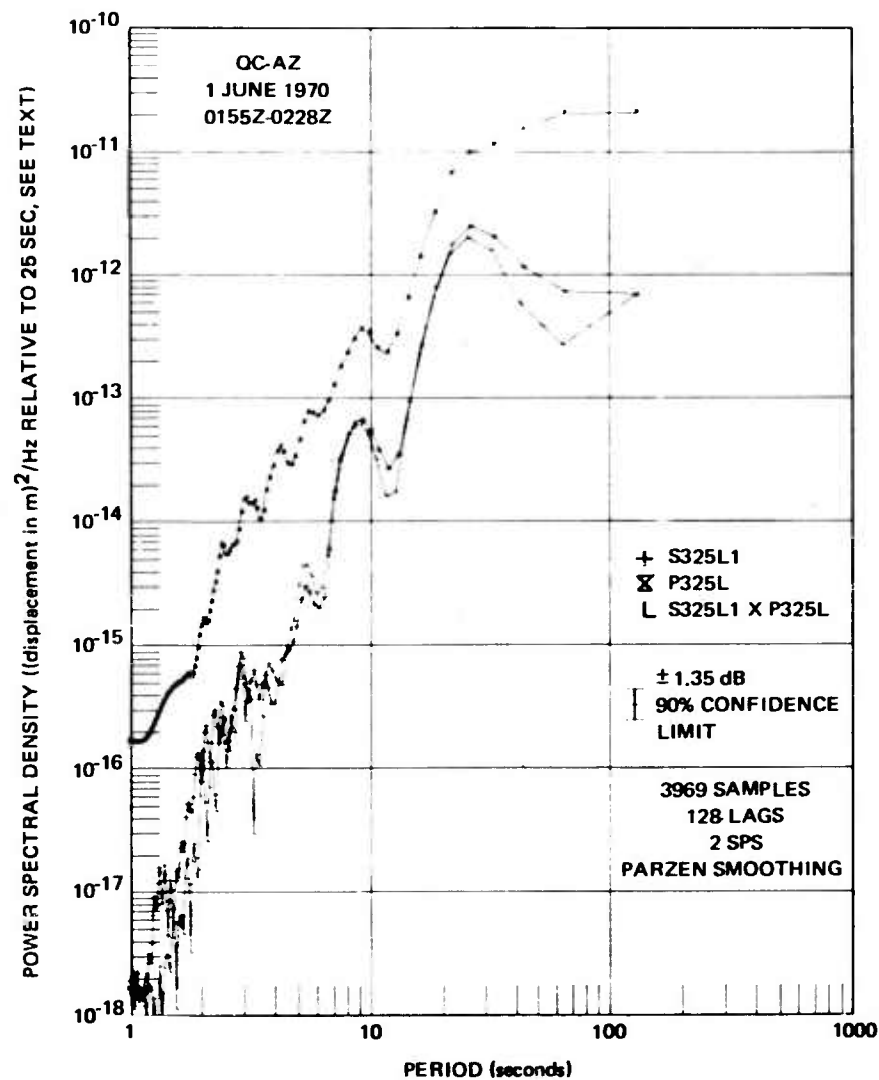
b. Coherence



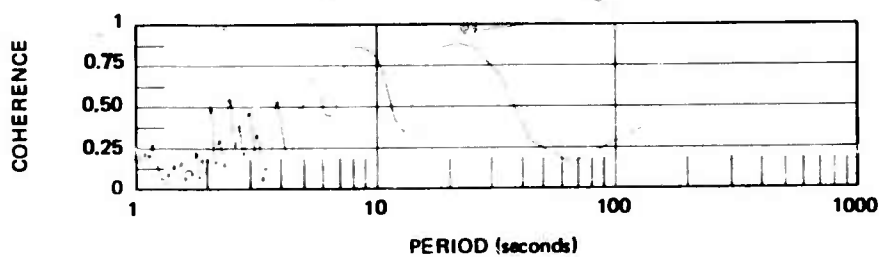
c. Phase lead  
S325L2 over S325L1

Figure 39. Power spectral density, coherence, and relative phase angle with 128 lags for parallel horizontal strain seismographs S325L1 and S325L2 during the LRI Rayleigh wave of an aftershock of the Peru earthquake

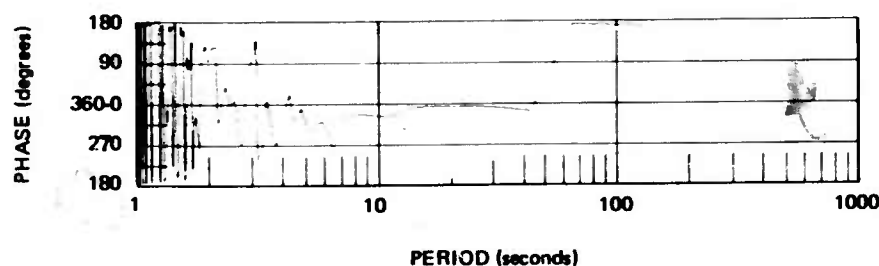
G 6027



a. Power spectral density



b. Coherence



c. Phase lead  
P325L over S325L1

Figure 40. Power spectral density, coherence, and relative phase angle with 128 lags for parallel horizontal seismographs, S325L1 strain and P325L inertial, during the LRI Rayleigh wave of an aftershock of the Peru earthquake.

G 6028



In figure 40, the coherence is about 0.9 near 8 sec and 25 sec. The relative phase angle is zero except at periods of 64 and 128 sec where it is 180 deg. During the third earthquake signal analyzed, the rms motion (relative to 25 sec) in the whole passband was: S325L1  $1.82 \times 10^{-11}$  strain, S325L2  $1.95 \times 10^{-11}$  strain, and P325L  $9.05 \times 10^{-7}$  m.

#### 11.5 SEISMIC NOISE RESULTING FROM ATMOSPHERIC PRESSURE VARIATIONS

The fact that long-period seismographs become noisy when the wind blows has been known for several years. Recently, Sorrells and Der (1970) have shown that for simple models the vertical displacements resulting from forces created by variations in the atmospheric pressure field can be predicted with good success. This section of the report reviews some of the past observations of pressure induced noise; extends the recently developed theory to predict ground displacements to include ground strain and tilt; and presents a spectral comparison between the strain seismographs and the microbarograph. Section 11.6 extends the noise considerations to include linear and non-linear tilt noise on horizontal inertial seismographs. The discussion in these two sections represents a status report. Because of the importance of understanding noise sources and mechanisms to the improvement of signal-to-noise ratio at QC-AZ and any other high sensitivity seismograph installation, more investigations will be made into these phenomena.

Some of the motions referred to in these two sections are on the order 1 to 0.1 Angstroms. While these small motions have undoubtedly contributed to seismograph noises at other locations, only the high sensitivity available at QC-AZ and the comparisons between strain and inertial seismographs have enabled the investigators to begin to detect the phenomena that are contributing to seismograph noise.

##### 11.5.1 Previous Observations of Wind-Related Long-Period Noise

Effects of pressure loadings on the ground began to be quantitatively observed in 1963 and 1964 after instrument stability and installation problems were solved for the Advanced Long-Period System which was operated as a three-component long-period seismograph at 100K magnifications at the Wichita Mountain Observatory (WMO). The history of the improvement of the instruments and the instrument installation to increase their stability will not be discussed here. Instrumentation noise is discussed by Whalen (1963) and a summary of long-period seismograph development was given by Hamilton (1964).

One of the present authors (JEF) working with Burden (1964) established that noise on horizontal pendulum seismographs was positively correlated with wind action. It was also observed that seismometers installed in a walk-in vault within a small hill were significantly more susceptible to wind noise than a seismometer installed in a tank vault about 1 m below the surface but only 60 m away from the hillock. The wind related (pressure induced) noise was deemed to be a localized tilt having a dimension of about 50 m. The dimension of the tilting region was deduced from the relationship between the horizontal and the vertical displacements. The geomorphology of WMO encompasses layers of rhyolite which are broken up into large blocks by joints easily visible at the surface by local vegetation changes. The dimensions of the tilting surfaces deduced from the seismograms agree with the dimensions of the physical block structure in the vicinity.

Under the same author's (JEF) supervision, Milam (1965) continued the development of improved installation techniques to minimize all noise in the ALPS system. Pressure induced tilt was reduced by a further significant amount on a horizontal seismometer installed in an 8 m deep vault about 100 m from the walk-in vault and the 1 m deep tank vault. A second seismograph installation was made about 100 m from the surface in the Stevenson-Bennett Mine near Las Cruces, New Mexico (LC-NM). (A Long-Range Seismic Measurements (LRSM) Program team co-occupied the mine during these experiments but operated independently.) The Las Cruces installation verified the capability of the full three-component seismograph to operate at magnifications of 100K (at X10 view) for extended periods of time. During this experiment, the need to use tank vaults inside a sealed seismometer chamber well within a mine was conclusively established. After all pressure and temperature effects acting directly on the seismometers were eliminated, noise was observed on the horizontal seismometers when the wind velocity exceeded about 30 mph. The existence of a wind related noise threshold at both WMO and LC-NM confirms that the elastic loading is proportional to the pressure induced force at the surface. Since the wind velocity related to the noise threshold at a 100 m depth at Las Cruces was greater than the wind velocity related to the noise threshold in the 1 m deep or the 8 m deep tank vaults at WMO, the observations confirmed that the amplitude of the displacements was related to the wind velocity.

A similar attenuation of pressure induced noise was observed at the WMO short-period strain installation in 1967. (See Shopland, 1968.) The original trench depths were 2.8 to 3.7 m on the east strain seismometer and 3.6 to 3.7 m on the north strain seismometer. An additional 1.3 m of overburden was added. The wind velocity related to the noise threshold increased from about 7 km/hr on the east seismograph and about 20 km/hr on the north seismograph to about 35 km/hr on both seismographs. A spectral comparison of the east seismograph during 15 to 20 mph winds before and after the additional overburden was added showed a 5 to 10 dB power reduction at frequencies above 0.8 Hz and not much change in power at longer periods. Figure 41 shows a replot of the data points in figure 51 from Shopland (1968) on a log-log scale. Straight lines have been visually fit to these data points. The equations for the lines are:

strain east before

$$u = 0.1625 C^{1.495}$$

strain north before

$$u = 0.000324 C^{2.91}$$

strain north after

$$u = 0.000563 C^{2.20}$$

where

$u$  = equivalent ground motion in millimicrons  
peak-to-peak calculated from the strain  
seismograms

$C$  = wind velocity in km/hr

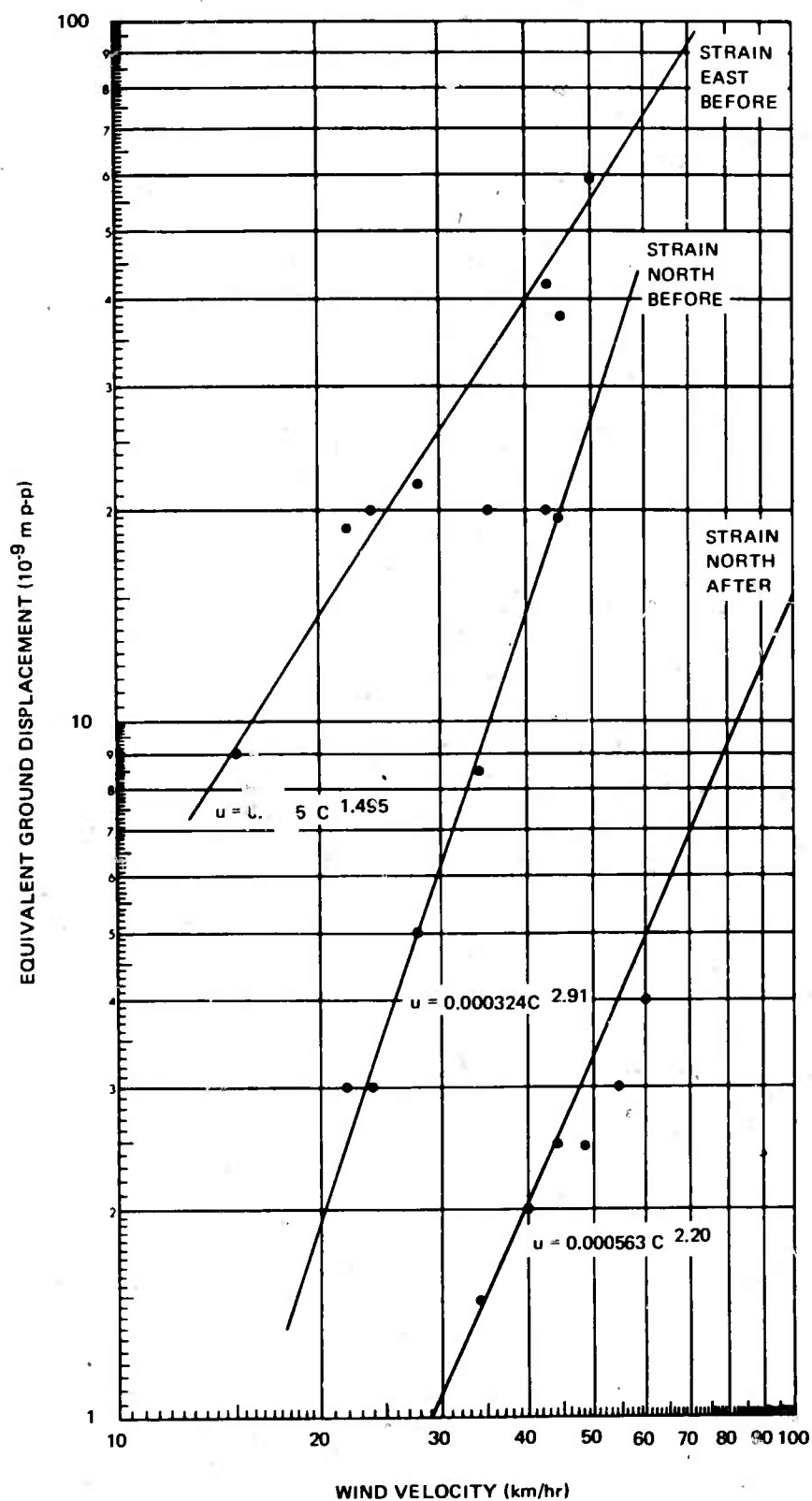


Figure 41. Relationship between equivalent ground displacement and wind velocity at WMO

G 6029

The improvement of the operation of a long-period seismograph by burial in a culturally noisy location was also demonstrated by Rector (1965). Three seismometers in a 15.25 m deep cased hole, in a surface tank vault inside a building, and on a concrete pier in a building were used for the tests at the Geotech Garland facility. After properly pressure sealing and insulating the buried seismometer, operating magnifications of 10 to 20K were possible. During the same time intervals, the two surface seismometers could only operate at 0.5 to 2K. The burial sufficiently attenuated most cultural vibrational and pressure induced noises; however, all seismometers responded to large tilts resulting from surface loading by trains and vehicles. No quantitative tilt comparisons could be made because of the relative locations and depths of the various piers.

Other cases of improved long-period seismograph operation were reported in the LRSM program. Warren (1966) excavated a 9.1 m deep vault at La Paz, Bolivia. In conjunction with improvements made in the thermal and pressure stability the depth of the installation attenuated wind related disturbances and resulted in an improvement of operating magnifications from the 10 to 20K range to the 100 to 200K range. Simons (1968) reported on an experiment that compared the operation of long-period seismographs in surface tanks and at the bottom of 162 ft deep missile silos at two different locations both of which were in sediments. He concluded that there was noise on the horizontal seismometers that positively correlated with wind gusts (more than a steady wind). However, no quantitative relationship could be established between tilt at the surface and at depth. In fact, at times the surface horizontal seismometers would tilt first and at other times the silo seismometers would tilt first. The relative amplitudes of the tilts also varied with either the surface or the silo seismometers having the largest amplitude.

The Uinta Basin Observatory (UBO) operated three sets of three-component long-period seismographs simultaneously (Teledyne Industries, 1966). The approximate depths to the three piers were 0.6 m, 2 m, and 15 m. By visual comparison of recordings made, the deeper vaults during windy conditions were about 6 dB and about 18 dB quieter, respectively, than the shallowest vault. A detailed quantitative study of the relationship between the wind velocity, pressure, and seismic noise versus depth was not made.

During testing of the triaxial long-period seismometer in a 60 m (200 ft) deep hole at UBO, the coordinate transformed horizontal outputs of the triaxial system were compared to the three-component system at the 15 m depth. The triaxial system output from a depth of 53 m (175 ft) was found to be about 12 dB quieter than the output of the shallower system (Kirkpatrick, 1968.)

#### 11.5.2 Long-Period Earth Strains and Atmospheric Pressure Variation

To explain the many observations of (1) wind related noise on long-period seismographs and (2) attenuation of this noise with depth, Sorrells (1969), Der (1969), and Sorrells and Der (1970) developed a theory for the displacements associated with the passage of a plane wave of air pressure over an infinite, isotropic, homogeneous, half-space and over a layered half-space. Their equations for displacements in the half-space have been differentiated to obtain the relationship between strains and tilts and the amplitude of the pressure wave.

Consider a system of axes in which the 1 axis is in the direction of wave propagation and the 3 axis is vertical down. The displacements derived by Sorrells (Sorrells and Der, 1970) with a slight change in nomenclature are

$$u_1(x_1, x_3, t) = \frac{ic_0 P}{2\mu|\omega_0|} \left( \frac{\mu}{\lambda+\mu} - \frac{|\omega_0|x_3}{c_0} \right) e^{-\frac{|\omega_0|x_3}{c_0}} e^{i\omega_0 \left( t - \frac{x_1}{c_0} \right)} \quad (1)$$

and

$$u_3(x_1, x_3, t) = \frac{-c_0 P}{2\mu|\omega_0|} \left( \frac{\lambda+2\mu}{\lambda+\mu} + \frac{|\omega_0|x_3}{c_0} \right) e^{-\frac{|\omega_0|x_3}{c_0}} e^{i\omega_0 \left( t - \frac{x_1}{c_0} \right)} \quad (2)$$

By taking the appropriate derivatives, the linear strain in the direction of propagation, the vertical linear strain, the shear strain in the 1-3 plane, and the tilt in the 1 direction are found to be:

$$e_{11} = \frac{du_1}{dx_1} = \frac{P}{2\mu} \left( \frac{\mu}{\lambda+\mu} - \frac{|\omega_0|x_3}{c_0} \right) e^{-\frac{|\omega_0|x_3}{c_0}} e^{i\omega_0 \left( t - \frac{x_1}{c_0} \right)} \quad (3)$$

$$e_{33} = \frac{du_3}{dx_3} = \frac{P}{2\mu} \left( \frac{\lambda+2\mu}{\lambda+\mu} + \frac{|\omega_0|x_3}{c_0} - 1 \right) e^{-\frac{|\omega_0|x_3}{c_0}} e^{i\omega_0 \left( t - \frac{x_1}{c_0} \right)} \quad (4)$$

$$e_{13} = \frac{1}{2} \left( \frac{\partial u_1}{\partial x_3} + \frac{\partial u_3}{\partial x_1} \right)$$

$$e_{13} = \frac{iP}{2\mu} \frac{|\omega_0| x_3}{c_0} e^{-\frac{|\omega_0| x_3}{c_0}} e^{i\omega_0 \left(t - \frac{x_1}{c_0}\right)} \quad (5)$$

$$\text{tilt} = \frac{du_3}{dx_1} = \frac{iP}{2\mu} \left( \frac{\lambda+2\mu}{\lambda+\mu} + \frac{|\omega_0| x_3}{c_0} \right) e^{-\frac{|\omega_0| x_3}{c_0}} e^{i\omega_0 \left(t - \frac{x_1}{c_0}\right)} \quad (6)$$

$$u_2 = e_{22} = e_{i2} = 0, \quad i = 1, 2, 3 \quad (7)$$

where:

1, 2, 3 = axes designators

$x_i$  = coordinate in  $i^{\text{th}}$  axis

$u_i$  = displacement in  $i^{\text{th}}$  direction

$e_{ij}$  = component of strain tensor acting across plane perpendicular to  $i$  axis in direction of  $j$  axis

$P$  = amplitude of pressure wave

$\lambda, \mu$  = Lamé elastic constants

$\omega_0$  = angular frequency of pressure wave

$c_0$  = velocity of pressure wave in the  $x_1$  direction, assumed to be much smaller than the shear wave velocity

$t$  = time

Several observations can be made about equations (3) through (6) and their relationships to equations (1) and (2).

a. The linear strains and the tilt do not have the  $1/k_0 = c_0/|\omega_0|$  in their amplitude coefficients (where  $k$  is wave number). This result is to be expected because for a plane wave

$$u_m = e^{-ik \left( x_m - \frac{t}{c} \right)} \quad (8)$$

$$e_{mn} = \frac{\partial u_m}{\partial x_n} = -ik e^{-ik \left( x_m - \frac{t}{c} \right)} ; \quad m = n. \quad (9)$$

Since the velocity of the pressure wave is much less than the velocity of seismic surface waves,  $k$  is much larger for the pressure wave. Consequently, the ratio of pressure induced noise to surface wave signal on the strain seismograph is proportionally greater than the ratio of noise to signal on the inertial seismographs.

b. The linear strains are either in-phase or 180 deg out-of-phase with each other, depending on the sign of the terms in the parenthesis.

c. For each wave number, there is one depth where the horizontal strain  $e_{11}$  is zero.

d. For a given depth, for the same phase velocity, and at the longer periods, the term containing  $x_3$  in the parenthesis becomes negligible.

e. The linear strains  $e_{11}$  and  $e_{33}$  are  $\pm 90$  deg out of phase with the  $u_1$  displacement, the shear strain  $e_{13}$ , and the tilt.

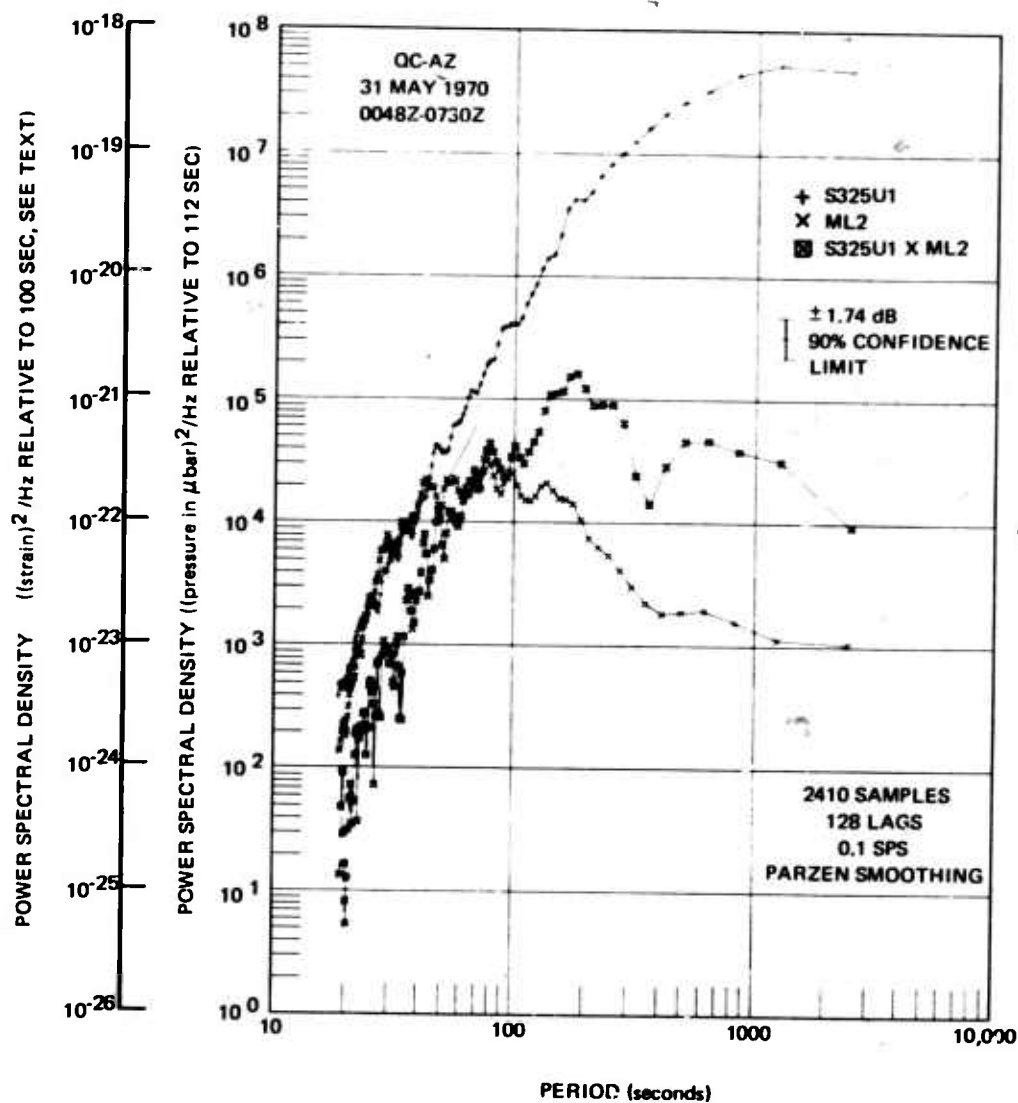
f. The tilt is  $\pm 90$  deg out of phase with the vertical displacement  $u_3$  and in or 180 deg out of phase with the horizontal displacement.

g. The factor controlling the attenuation with depth of all displacements, strains, and tilt is the exponential term  $e^{-k_0 x_3}$ .

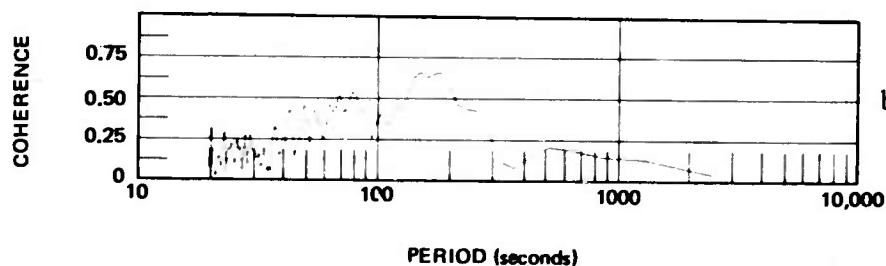
The amplitude of the pressure induced noise on strain and inertial instruments decays much more rapidly with depth than the amplitude of surface waves decays with depth. Therefore, by increasing the depth of an installation, the pressure induced noise can be reduced for better performance. This improvement in signal-to-noise ratio is one of the main reasons why a mine was selected for the installation site on this project.

### 11.5.3 Observed Strains and Pressure Variations

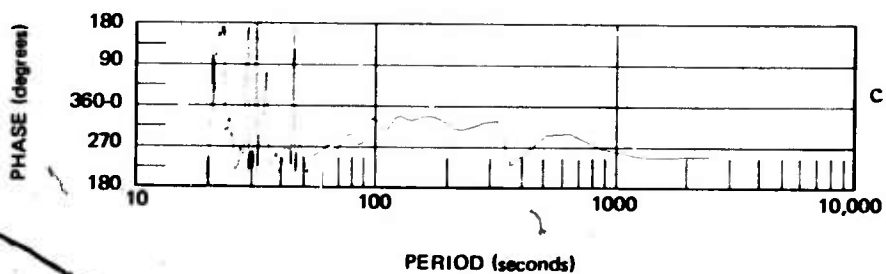
The ULP response seismograms recorded during the high wind conditions discussed in section 11.4.3 were compared with the ML2 microbarograph outside the mine. The results are plotted in figures 42 and 43. The rms values (referred to 25 sec) for the strain seismographs in the whole passband were  $3.605 \times 10^{-11}$  for S325U1,  $2.082 \times 10^{-11}$  for S325U2, and  $1.647 \times 10^{-11}$  for S55U. The rms value (referred to 112 sec) for the ML2 microbarograph was 22.02  $\mu$ bar. If the total strain energy on all three seismographs is assumed to be caused by the pressure source, then the ratio of rms values will give a ratio of strain per



a. Power spectral density



b. Coherence

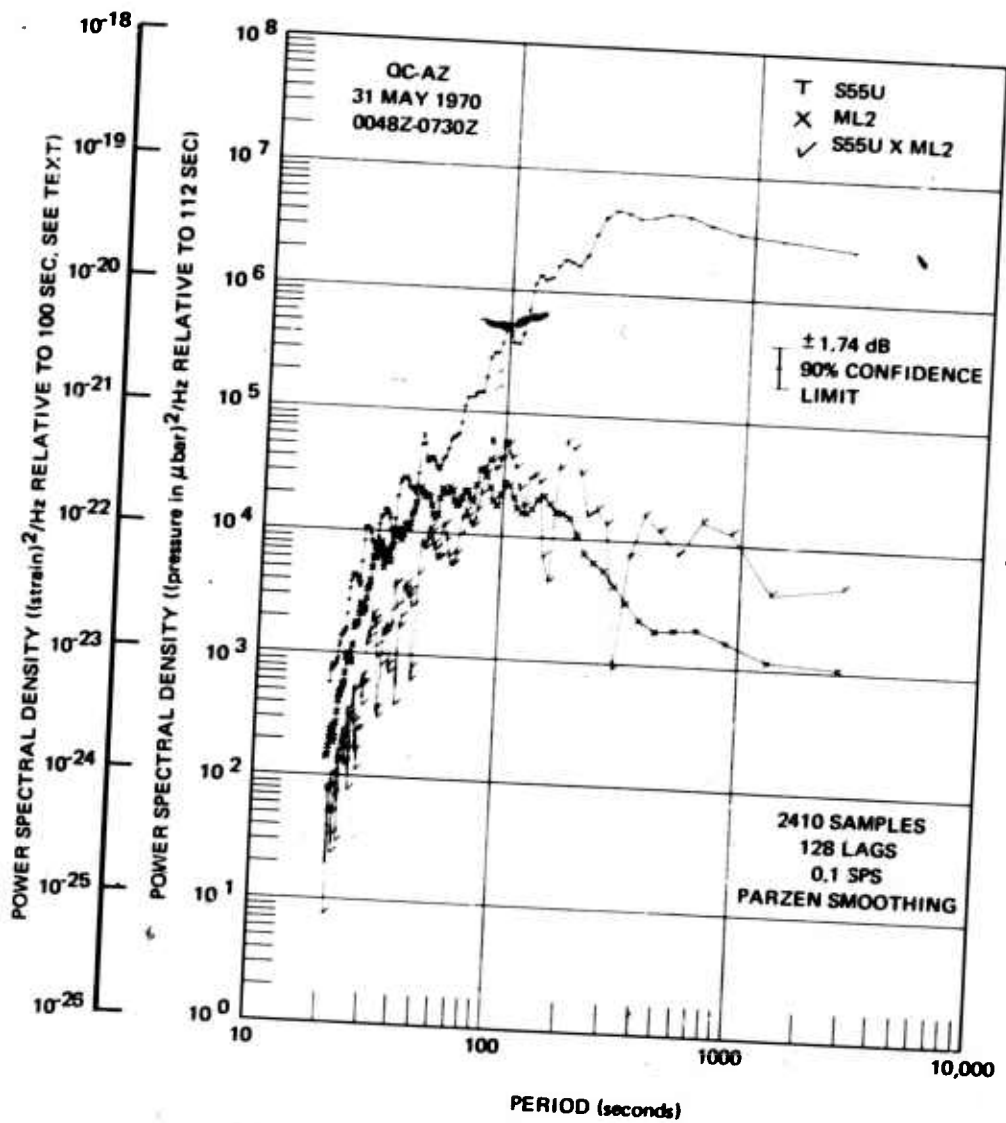


c. Phase lead ML2 over S325U1

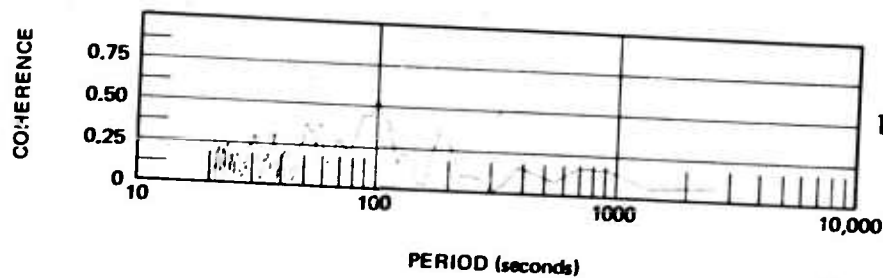
Figure 42. Power spectral density, coherence, and relative phase angle between horizontal strain seismograph S325U1 and microbarograph ML2

G 6030

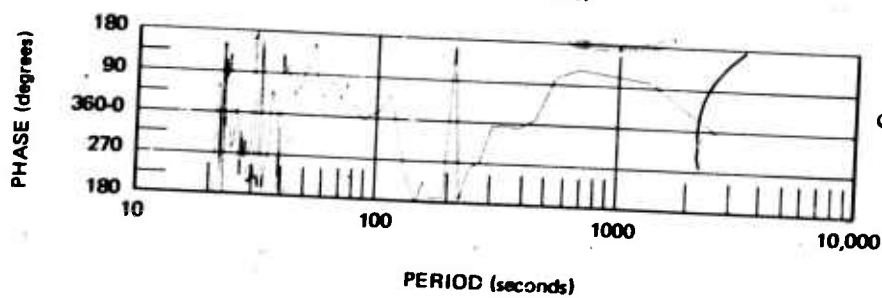




a. Power spectral density



b. Coherence



c. Phase lead  
ML2 over S55U

Figure 43. Power spectral density, coherence, and relative phase angle between horizontal strain seismograph S55U and Microbarograph ML2

microbar disturbance. Taking these ratios gives  $1.64 \times 10^{-12}$  strain/ $\mu$ bar,  $9.46 \times 10^{-13}$  strain/ $\mu$ bar, and  $7.48 \times 10^{-13}$  strain/ $\mu$ bar, respectively. This assumption is not correct as indicated by the coherence in figures 42 and 43. The spectra in both figures were plotted with scales arbitrarily equalized at  $1 \mu\text{bar} = 10^{-13}$  strain. A more meaningful relationship will be obtained in future work by dividing the cross spectra by the microbarograph spectra. The cross spectra is an estimate of the linearly related power in the microbarograph and the seismograph and does not include microseismic power or system noise power from either instrument.

## 11.6 LINEAR AND NON-LINEAR TILT NOISE ON LONG-PERIOD SEISMOGRAPHS

The ground tilts with the passage of Rayleigh waves and with the application of localized forces. Seismographs respond to these tilts with varying degrees of sensitivity. Linear strain seismographs respond to differential motion along their sensitive axis and are insensitive to motions orthogonal to this axis. Therefore, a linear strain seismograph constructed to measure the strain component  $e_{11}$  will be insensitive to the other eight strain components  $e_{ij}$ ,  $i = 1,2,3$ ,  $j = 1,2,3$ , except  $i = j = 1$ . The vertical inertial seismograph will respond to the vertical displacement component of the tilt. Generally for pressure induced noise, the output of a vertical seismograph is about 1/10 the output of the horizontal seismograph. The horizontal seismograph must respond in the same manner to a true horizontal acceleration as it does to the component along the sensitive axis of the instrument of the gravitational acceleration created by a tilt of the base on which the seismometer rests.

This part of the report will (1) adapt a general theory for non-sensitive axis disturbances to horizontal pendulum seismometers developed by Rodgers (1968) to the specific parameters of the ALPS response for tilt resulting from Rayleigh waves and pressure loading, (2) present some data on the nature of the change of the seismic spectrum with increasing wind velocity and pressure variations, and (3) present data that indicate much of the tilting observed in horizontal inertial seismographs is the result of rigid block non-linear tilting and amplification of the tilts significantly above predicted values.

### 11.6.1 Tilt Theory for ALPS Response Horizontal Seismographs

Rodgers (1968) very thoroughly treats the response of the horizontal pendulum seismometer to Rayleigh and Love waves, tilts, and free oscillations. The most significant spurious response is to tilt and to the tilt associated with Rayleigh waves. These two spurious responses will be considered in this paragraph. As mentioned above, the horizontal pendulum responds to the component of the gravity acceleration created by the tilt of the base. Thus the seismometer responds to tilt as an accelerometer. If  $A_D(\omega)$  is the displacement amplitude frequency response and  $A_T(\omega)$  is the tilt amplitude frequency, with  $g$  the gravitational acceleration, Rodgers (1968, equation (72)) has shown that

$$A_T(\omega) = \frac{g}{\omega^2} A_D(\omega) \quad (9)$$

The ALPS displacement amplitude response is plotted in figure 44 equalized to a magnification of 100,000 at 25 sec period. The equivalent tilt response is plotted in the figure to the same scale and is seen to reach a maximum of about 30,000,000 for a rather broad peak of frequencies. Rodgers also gives an equation for the output of a seismograph for a retrograde Rayleigh wave as

$$\phi = \phi_i \left( 1 + \frac{g/c}{2\pi\beta} \tau \right) \quad (10)$$

where

$\phi$  = actual seismogram

$\phi_i$  = ideal seismogram

$g$  = gravity acceleration

$c$  = wave phase velocity

$\beta$  = particle motion ellipticity parameter, ratio of horizontal semi-axis to vertical semi-axis

$\tau$  = period of wave.

The second term in the parenthesis in equation 10 is the tilt term. Values for the tilt term have been calculated using  $\beta = 2/3$ , which would apply for an infinite half-space, and with typical values for Rayleigh wave phase velocity. These calculated values are listed in table 3. The tilt response

$(1 + \frac{g/c}{2\pi\beta} \tau) A_D(\omega)$ , is plotted in figure 44. From this figure it can be

seen that the addition of the tilt response to the displacement response for a Rayleigh wave is very small compared to the potential response that a horizontal seismometer could have to a tilt at the same periods. The difference between the Rayleigh wave response and the tilt response will be referred to later.

#### 11.6.2 Seismic Spectral Changes with Pressure Activity Changes

Now let's consider the spectral content of the pressure induced noise, then the effect on the horizontal pendulum of pressure induced tilts and of Rayleigh wave induced tilts will be discussed. Figure 45 shows a plot of the S325L1 spectra under low and high wind conditions and the P325L spectra under high wind conditions. As the wind associated, pressure induced noise increases, it increases over the whole spectra. The microseismic peaks visible on the S325L1 strain during the low wind conditions are completely swamped with the strains from the high wind pressure changes. This same raising and lowering of the entire spectrum was observed by Herrin (1963, a personal communication) with a vertical seismograph flat to velocity from 1.25 sec to 110 sec used during an experiment in south Texas. At low wind conditions microseismic peaks were clearly visible at 2 Hz and 6 sec. As the wind velocity increased,

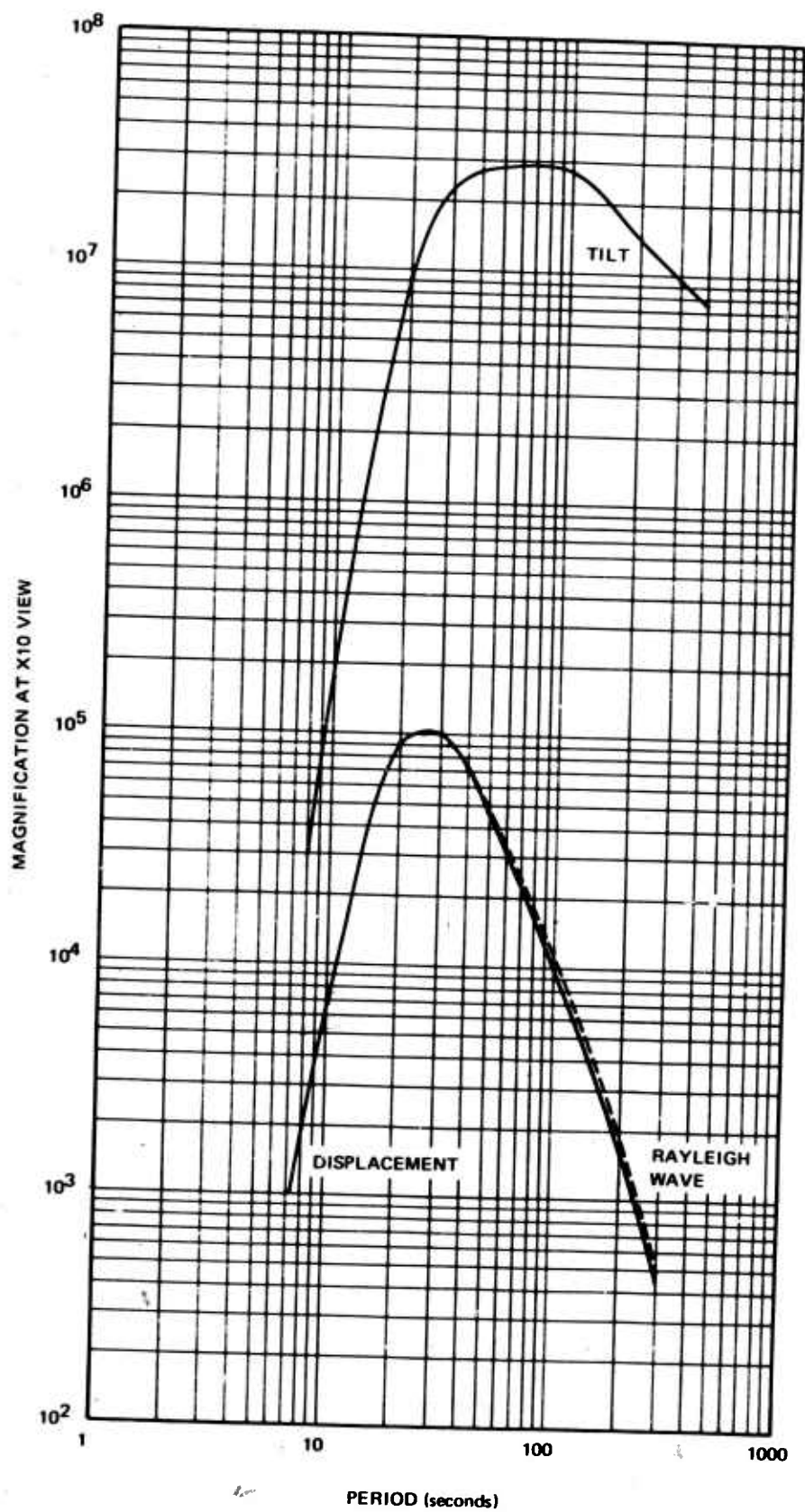


Figure 44. Horizontal inertial ALPS seismograph response to displacement, tilt, and Rayleigh waves

G 6032

Table 3. Tilt response of horizontal inertial seismometers to Rayleigh waves

Period sec	Phase velocity km/sec	$\frac{g/c}{2\pi\beta} \tau$
10	3.0	0.008
15	3.0	0.012
20	3.36	0.014
24	3.50	0.016
26	3.56	0.017
30	3.65	0.019
34	3.78	0.021
40	3.90	0.024
45	3.93	0.027
50	3.97	0.029
55	3.98	0.032
60	3.99	0.035
70	4.00	0.041
80	4.03	0.046
90	4.07	0.052
100	4.11	0.057
150	4.28	0.082
200	4.57	0.102
250	4.90	0.119
300	5.28	0.133

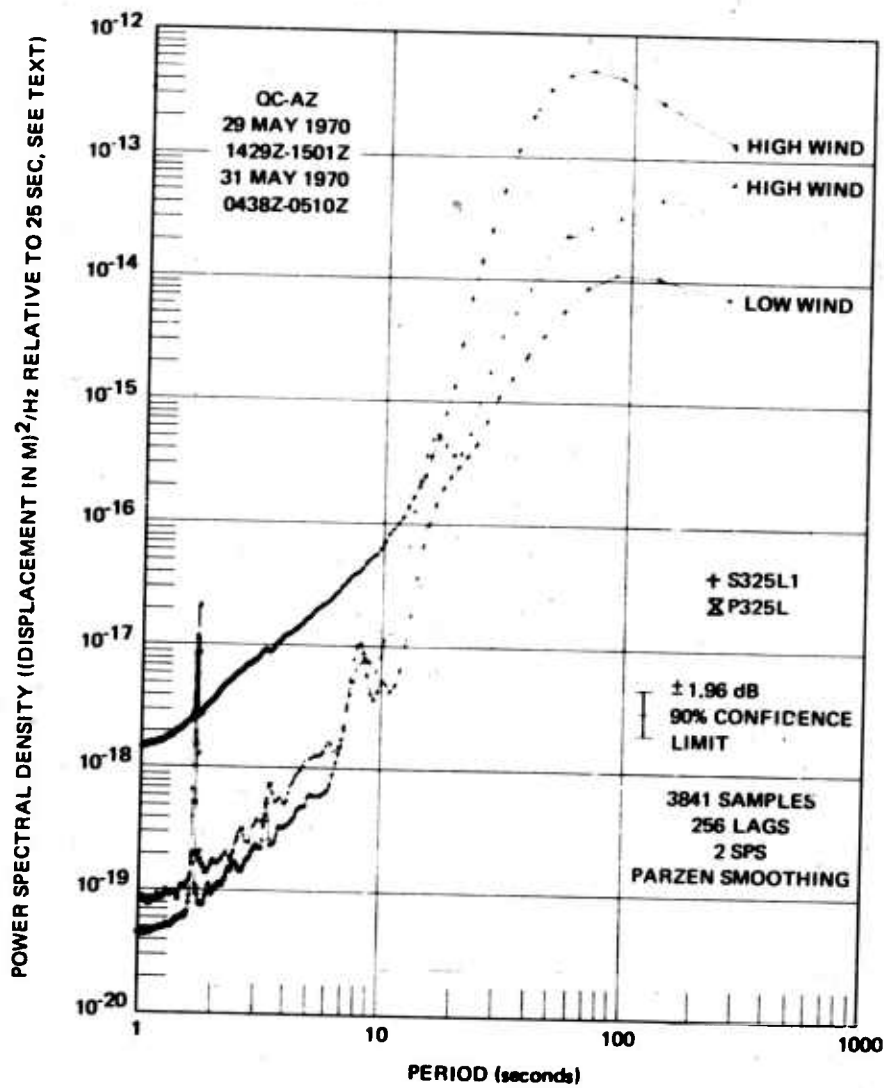


Figure 45. Comparison of power spectral density between low and high wind conditions

valleys in the spectra were filled in until finally the 2 Hz then the 6 sec peaks disappeared into the pressure induced spectra. Thus the pressure induced noise to a first order approximation can be considered to be a white noise source. (The ML2 spectra in figures 42 and 43 when considered along with the microbarograph response actually indicate a flat response to rate-of-change of pressure between about 50 sec and 400 sec.) The output of any system to a white noise source is the system response. Therefore, the shape of the spectral output of a seismograph can give strong indications as to the input character.

#### 11.6.3 Non-Linear Tilting

Several sets of data demonstrating the tilt response have already been presented; two will be discussed here. The spectra of the inertial P325L during high wind conditions are compared to the spectra of the S325L1 strain in figures 30 and 45. At periods longer than 64 sec, the S325L1 spectra decreases, but the P325L spectra continues to increase. This divergence in the spectra implies a non-linear relationship which is confirmed in the coherence plotted in figure 30. It is hypothesized that the additional output on the inertial system is a symptom of rigid body tilting with possibly relative movement on the local joint and fault pattern. Movement on local joints and faults in the immediate vicinity of instrument systems has been observed by Harrison (1969) in the Poorman Fault near Boulder, Colorado. Stewart Smith (1970, personal communication) has hypothesized that the residual strains observed in the near field of large explosions (and possibly in the far field of earthquakes) are actually the readjustment of the strain field in the vicinity (10's m to 10's km) of the seismometers.

For teleseismic earthquakes, this readjustment is triggered by the passage of the Rayleigh wave which is generally the largest amplitude elastic wave. Both Harrison's and Smith's observations apply to a step readjustment. The hypothesis presented here is that the readjustments along local joints and faults is a dynamic phenomena occurring all the time in much smaller amplitudes (on the order of 0.1 Angstrom) than have previously been resolved. It is felt that this phenomena is not unique to QC-AZ but that it can be observed at any high sensitivity seismic observatory.

The LR1 Rayleigh wave spectra in figure 40 also substantiates the excess tilt response of the horizontal inertial P325L over the response of the strain S325L1. If the S325L1 spectra is taken as representative of the true Rayleigh wave motion, then table 3 and figure 44 indicate that at 100 sec there should only be about 5.7 percent greater amplitude on the pendulum from the Rayleigh wave tilt. The assumption that the S325L1 spectra represents the true Rayleigh wave motion is supported by the cross spectra in figure 40 which is almost identical to the S325L1 spectra. The observed output in power spectral density at 100 sec of the P325L is a factor of about 30 larger than the power of the S325L1. The ratio of the observed 30:1 difference is so much greater than the 1.057:1 difference predicted by the theory, that it has to be related to a phenomenon other than an elastic response to the travelling wave. Even if the S325L1 spectra is normalized upward by the 3.5 power ratio, the tilt output is still in excess over the Rayleigh wave tilt.

In summary, the authors contention is that this other phenomenon is a rigid block motion on the order of 0.1 Å in amplitude on the local joint pattern and that this motion is apparently accompanied by a frictional damping action. It is expected that this same action will be observed at any high-sensitivity seismic observatory.

## 12. SPECIAL REPORT

A special technical report (Fix and Sherwin, 1970) has been submitted to summarize the instrumentation complex objectives, design, installation, and preliminary results. Authority for publication has been received according to the VELA UNIFORM security review procedure. This paper has been submitted to the Bulletin of the Seismological Society of America for consideration of publication.

## 13. REFERENCES

- Burden, H. Owen, 1964, Operation and calibration of Advanced Long-Period System, Technical report no. 64-95: Garland, The Geotechnical Corp., 30 p.
- Der, Zoltan, 1969, Long-period seismic noise and atmospheric pressure variations. Part 2. The response of a layered half space to atmospheric pressure changes, Technical note 4/69: Garland, Geotech, A Teledyne Company.
- Fix, James E., and Sherwin, John R., 1970, A high-sensitivity strain/inertial seismograph installation, Technical Report No. 70-3: Garland, Teledyne Geotech, 44 p.
- Hamilton, Jack H., 1964, Summary of long-period seismograph work at Geotech, Technical report no. 64-121: Garland, The Geotechnical Corp., 39 p.
- Harrison, J. C., 1969, More tilt measurements from the Poorman Mine, near Boulder, Colorado (abstract): EOS, Trans. Amer. Geophys. Union, v. 50, no. 11, p. 643.
- Kirkpatrick, B. M., 1968, Long-period triaxial seismograph development, Quarterly report no. 7, Project VT/6706, Technical report no. 68-20: Garland, Geotech, A Teledyne Company, 27 p.
- Lanczos, Cornelius, 1956, Applied analysis: Englewood Cliffs, Prentice Hall, Inc., 539 p.
- Milam, W. C., 1965, Final report on study of the operation of the Advanced Long-Period System, Technical report no. 65-93: Garland, Teledyne Industries, Geotech Div., 78 p., 6 app.



- Mitchell, B. J. and Landisman, M., 1969, Electromagnetic seismograph constants by least-squares inversion: Bull. Seism. Soc. Am., v. 59, no. 5, p. 1335-1348.
- Rector, Robert E., 1965, Shallow-hole test of long-period horizontal seismometer, Technical report no. 65-30: Garland, The Geotechnical Corp., 22 p.
- Rodgers, P. W., 1968, The response of the horizontal pendulum seismometer to Rayleigh and Love waves, tilt, and free oscillations of the Earth: Bull. Seism. Soc. Am., v. 58, no. 5, p. 1384-1406.
- Shopland, Robert C., 1968, Final Report, Project VT/5081, Multicomponent strain seismograph, 1 July 1965 to 31 December 1967, Technical report no. 68-3: Garland, Geotech, A Teledyne Company, 156 p., 2 app.
- Shopland, Robert C., 1970, Design of portable strainmeter system, Technical report no. 70-6: Garland, Teledyne Geotech, 55 p.
- Simons, R. S., 1968, Operation of long-period seismographs in deactivated missile silos, Technical report no. 68-4: Garland, Geotech, A Teledyne Company, 45 p.
- Sorrells, G. G. and Der, Zoltan, 1970, Long-Period seismic noise and atmospheric pressure variations, Technical report no. 70-12: Garland, Teledyne Geotech, 76 p.
- Sorrells, G. G., 1969, Long-period seismic noise and atmospheric pressure variations. Part 1. The response of an isotropic half space to a plane pressure wave, Technical note 3/69: Garland, Geotech, A Teledyne Company, 20 p.
- Teledyne Industries, Geotech Division, 1966, Operation of two observatories, final report, Project VT/5054, 1 May 1965 through 30 April 1966, Technical report no. 66-54: Garland, Teledyne Industries, Geotech Division, 100 p., 3 app.
- Warren, N. M., 1966, Long-period seismograph installation, La Paz, Bolivia, Technical report no. 66-60: Garland, Teledyne Industries, Geotech Division, 16 p.
- Whalen, Joseph M., 1963, Instrumentation noise of long-period seismographs, paper presented at 13th IUGG General Assembly, Berkeley, California; also Technical report no. 63-81: Garland, The Geotechnical Corp., 26 p.

APPENDIX to TECHNICAL REPORT NO. 70-29

INSTRUMENT NOMENCLATURE, RECORDER  
CHANNEL ALLOCATION, AND POLARITY

## INSTRUMENT NOMENCLATURE, RECORDER CHANNEL ALLOCATION, AND POLARITY

This appendix lists the instrument nomenclature, the normal recorder channel assignments, and the polarity convention for the Queen Creek Seismological Station (QC-AZ).

### 1. NOMENCLATURE

The nomenclature used for the instrument system identifiers is:

<u>Category of data</u>	<u>Identifier</u>
Time:	BCD = binary coded decimal station time WWV = WWV time
Compensation:	Comp = playback compensation channel
Data:	first symbol: S = strain P = pendulum M = microbarograph* W = wind  second symbol*: Z = vertical 325 = 325 degree azimuth 55 = 55 degree azimuth V = (wind) velocity D = (wind) direction  third symbol: L = Advanced Long-Period System (ALPS) response U = Ultra-Long-Period (ULP) response X = Extended-Long-Period response B = Broad-Band (BB) response

S = Short-Period (SP) response

fourth symbol: L = Low gain

1,2,3 = numbers assigned to similar instruments

\*Microbarograph channel identifiers do not have a symbol in the second symbol category.

Flag: flag = identifier for clipping at Ithaco amplifier output

## 2. RECORDER CHANNELS

### 2.1 TAPE RECORDERS

<u>Channel No.</u>	<u>No. 1</u>	<u>Recorder No. 2</u>	<u>No. 3</u>
1	BCD	BCD	BCD
2	SZLL	WV2	MU
3	P325LL	SZB	SZUL
4	P55L	P55S	P55X
5	S325LL	S55B	S325UL
6	S55L	S55S	S55U
7	Comp	Comp	Comp
8	S325L	S325S	S325U
9	SZL	SZS	SZU
10	P325L	P325S	P325X
11	PZL	PZS	PZX
12	S55LL	WD2	S55UL
13	PZLL	S325B	ML1
14	P55LL	WWV	ML2

## 2.2 16 mm FILM RECORDERS

<u>Channel No.</u>	<u>No. 1</u>	<u>Recorder</u>	<u>No. 2</u>
1	FLAG		WWV
2	WWV		S325L-S55L
3	SZL		SZL+S325L+S55L
4	SZLL		S325L+S55L
5	S325L		SZL
6	S325LL		PZL
7	S55L		S325L+P325L
8	S55LL		S325L
9	PZL		P325L
10	P325L		S325L-P325L
11	P55L		S55L+P55L
12	PZX		S55L
13	P325X		P55L
14	P55X		S55L-P55L
15	ML1		ML1
16	PZS		off
17	P325S		only
18	P55S		16
19	WV		channels
20	WD		

## 2.3 35 mm FILM RECORDER

<u>Channel No.</u>	
1	SZU
2	S55U
3	S325U
4	MU

## 3. POLARITY

The polarity convention used on QC-AZ recorders is as follows:

Strain:

Compression is up on film recorders and positive voltage into the magnetic-tape recorders.

Inertial:

Displacement toward up, toward 525 deg azimuth, and toward 55 deg azimuth are up on film recorders and positive voltage into the magnetic-tape recorders.

Electromagnetic calibration coils:

Connected so that a dc current turned on produces a positive output.

Unclassified  
Security Classification

DOCUMENT CONTROL DATA - R & D

<i>(Security classification of title, body of abstract and indexing annotation must be entered when the overall report is classified)</i>		
1. ORIGINATING ACTIVITY (Corporate author) Teledyne Industries, Inc., Geotech Division 3401 Shiloh Road - Garland, Texas 75040		2a. REPORT SECURITY CLASSIFICATION Unclassified
3. REPORT TITLE Development of LP Wave Discrimination Capability Using LP Strain Instruments Quarterly Report No. 8, Project VT/8706		2b. GROUP
4. DESCRIPTIVE NOTES (Type of report and inclusive dates) Quarterly Report, 1 April 1970 to 30 June 1970		
5. AUTHOR(S) (First name, middle initial, last name) Fix, James E. and Sherwin, John R.		
6. REPORT DATE 21 September 1970	7a. TOTAL NO. OF PAGES 99	7b. NO. OF REFS 19
8a. CONTRACT OR GRANT NO. F33657-69-C-0121 ✓	9a. ORIGINATOR'S REPORT NUMBER(S) TR 70-29	
b. PROJECT NO. VELA T/8706	9b. OTHER REPORT NO(S) (Any other numbers that may be assigned this report)	
c.		
d.		
10. DISTRIBUTION STATEMENT This document is subject to special export controls and each transmittal to a foreign national may be made only with the prior approval of Chief, AFTAC. Qualified users may request copies of this document from: Defense Documentation Center, Cameron Station, Alexandria, Va. 22314		
11. SUPPLEMENTARY NOTES		12. SPONSORING MILITARY ACTIVITY HQ USAF (AFTAC/VELA Seismological Center), Washington, D. C. 20333
13. ABSTRACT Progress during the second quarter of 1970 is reported. Variable-capacitance transducers will be installed on the three strain seismometers in July for a broad-band output. A second microbarograph records pressure fluctuations outside the mine. A second Develocorder and an analog computer are recording directional beams on-line by combining strain and inertial seismographs. The second 325 deg azimuth strain seismometer will be used to construct a vertical seismometer in July. Magnets and coils on the LP inertial seismometers were returned to a standard configuration to match the strain response. A low-pass filter on the input to the strain preamplifier has limited amplifier saturation from large signals out of the passband. The mine seal has been improved to a 4 hour time constant. Three methods of obtaining system transfer functions from special test data were investigated. The most practical is to record the output from a step or impulse of current into the calibration coil and determine the transfer function by numerical smoothing and differentiating. Magnetic tape playback and on-line recordings provide enhancement of signals, wave type identification, and sharpened time breaks from interfering events and from low-level teleseismic earthquakes. Enhanced short-period recordings demonstrate that Pn, Pg, Sn, and Sg travel times from Rangely, Colorado, to QC-AZ are significantly longer than between NTS and QC-AZ. Examples of small surface waves detected are: $m_b = 4.1$ at 62 deg, $m_b = 4.0$ at 25 deg, and $m_b = 4.2$ at 100 deg. Power spectral density, coherence, and phase angle comparisons between parallel strain seismometers during low and high wind conditions and earthquake signals demonstrate that the instruments are operating properly and that calibrations are accurate. The history of the evaluation of wind-related LP noise is reviewed. Theoretical equations are developed for strains and tilts in a half-space from a plane wave pressure fluctuation. At 50 sec, a horizontal inertial seismometer operating at 100K (at 25 sec) has magnifications for displacements of 45,000, for Rayleigh waves of 46,300 and for tilts of 27,900,000. A hypothesis is presented that at all hard rock seismograph stations non-linear rigid block tilting occurs as a result of pressure loading and Rayleigh waves. Evidence that supports this hypothesis is: (1) There is a slight relative amplitude shift with frequency and a 90 deg relative phase between the two parallel strain seismometers. (2) The horizontal pendulums respond to significantly more tilt than is associated with a Rayleigh wave.		

DD FORM 1473  
1 NOV 65

Unclassified  
Security Classification

**Security Classification**

14

## KEY WORDS

**LINK A**

**LINK B**

**LINK C**

**ROLE**

WT

NAME	ROLE
Mr. J. Edgar Hoover	Director
Mr. Clegg	Chief of Bureau
Mr. Glavin	Chief of Bureau
Mr. Ladd	Chief of Bureau
Mr. Nichols	Chief of Bureau
Mr. Rosen	Chief of Bureau
Mr. Tracy	Chief of Bureau
Mr. Carson	Chief of Bureau
Mr. Egan	Chief of Bureau
Mr. Gurnea	Chief of Bureau
Mr. Hendon	Chief of Bureau
Mr. Pennington	Chief of Bureau
Mr. Quinn	Chief of Bureau
Mr. Nease	Chief of Bureau
Mr. Gandy	Chief of Bureau

WT

[illegible]

W T

## Wave Discrimination

**Security Classification**